

Université du Québec  
Institut National de la Recherche Scientifique  
Centre Énergie Matériaux Télécommunications

**Smooth Pyroelectric Luminescence in Lithium Niobate, beta Barium Borate and Barium Titanate**

Par

Mohamed Swaisi

Thèse présentée pour l'obtention du grade de  
Philosophiae Doctor (Ph.D.)  
en sciences de l'énergie et des matériaux

**Jury d'évaluation**

Président du jury et examinateur interne	Professeur Fiorenzo VETRONE Institut National de la Recherche Scientifique Centre Énergie Matériaux Télécommunications
Examinateur externe	Professeur Larbi SFAXI University of Monastir Faculté des Sciences de Monastir
Examinateur interne	Professeur Rafik NACCACHE Université de Concordia Chemistry and Biochemistry
Directeur de Recherche	Professeur Andreas RUEDIGER Institut National de la Recherche Scientifique Centre Énergie Matériaux Télécommunications



## **ACKNOWLEDGEMENTS**

First of all, my deepest gratitude goes to my wife and children, who were patient and understanding during the many busy days spent on my research. I would like to express my appreciation to my supervisor Prof. Andreas Ruediger, who diligently supported me from the very beginning of my studies. His permanent support, encouragement as well as his constant availability for an exchange of ideas were essential for the completion of my work. His welcoming, collegial and considerate attitude without the slightest reservation will always remain with me as a unique inspiration.

Each and every member of the Nanophotonics team has provided a pleasant and fruitful work environment. Special thanks go to Membarka Atantawi for assisting in my experimental work, as well as Dr. Andreas Dörfler who contributed to the refinement of the experimental setup, as well as for his support with the theoretical considerations and Dr. Rajesh Katoch for his scientific expertise. Last but not least, my gratitude goes to Dr. Azza Youssef, who helped me with the French translation.

## **RESUME**

La luminescence thermostimulée, et sa généralisation correspondante à la luminescence pyroélectrique, nous permet de caractériser une grande variété de cristaux diélectriques. Nous exposons les cristaux pyroélectriques à de faibles pressions ambiantes (jusqu'à  $10^{-7}$  mbar) et à des cycles de température, qui génèrent des schémas très spécifiques d'émission de lumière. Le vide très poussé empêche les décharges électrostatiques, ce qui permet la génération de champs électriques très élevés ( $\sim 10^7$  V/m) dus à l'effet pyroélectrique. Cela induit une faible émission de lumière caractéristique pendant la durée du changement de température. En plus des décharges en forme d'étincelles, nous observons des pics d'émission faibles et continus connus sous le nom de luminescence pyroélectrique lisse. Ce phénomène est dû à la recombinaison des porteurs de charge à l'intérieur du cristal, contrairement aux émissions en forme de pointes bien connues dues aux décharges dans l'atmosphère ambiante. Un cas particulier d'émission particulièrement prononcée se produit pendant la transition de phase à l'intérieur du cristal.

Nous développons un modèle microscopique de la luminescence qui permet la description de la luminescence pyroélectrique en fonction du temps, en particulier la détermination des potentiels de pièges profonds qui sont autrement inaccessibles à l'activation thermique. En utilisant ce modèle, nous montrons que le comportement de cette émission dans les cristaux est cohérent avec la libération des électrons piégés par émission de Poole-Frenkel et par effet tunnel de Fowler-Nordheim. Nous pouvons distinguer les deux mécanismes d'émission par la plausibilité physique des paramètres dérivés.

Les expériences portent sur des monocristaux de  $\text{LiNbO}_3$ ,  $\text{BaB}_2\text{O}_4$  et  $\text{BaTiO}_3$ . Notre modèle fournit les fréquences et les énergies d'activation des porteurs de charge piégés comme base de ce mécanisme de conduction, expliquant qualitativement la luminescence observée. Ce résultat fournit également des informations sur la quantité relative de pièges dans le cristal.

Mots-clés :

Luminescence, pyroélectricité, effet Poole-Frenkel, effet tunnel Fowler-Nordheim.

## ABSTRACT

The phenomenon known as thermostimulated luminescence, and its corresponding generalization to pyroelectric luminescence allows us to characterize material characteristics in a large variety of dielectric crystals. We expose pyroelectric crystals to low ambient pressures (down to  $10^{-7}$  mbar) and temperature cycles, which generate very specific patterns of light emission. The very high vacuum prevent electrostatic discharge, which allows the generation of very high electric fields ( $\sim 10^7$  V/m) due to the pyroelectric effect. This induces a characteristic, faint emission of light during the duration of the temperature change. Besides spark-like discharges, we observe faint, continuous emission peaks known as smooth pyroelectric luminescence. This phenomenon is brought about by charge carrier recombination inside the crystal, in contrast to the well known spike-like emissions due to discharges through the ambient atmosphere. A special case of especially pronounced emission occurs during the phase transition within the crystal.

We develop a microscopic model of the luminescence allows the description of the time-dependent pyroelectric luminescence, in particular the determination of deep trap potentials that are otherwise inaccessible to thermal activation. Using this model, we show that the behavior of this emission in crystals is consistent with the release of trapped electrons by Poole-Frenkel emission and Fowler-Nordheim tunneling. We can distinguish between the two emission mechanisms by the physical plausibility of derived parameters.

The experiments focus on  $\text{LiNbO}_3$ ,  $\text{BaB}_2\text{O}_4$ , and  $\text{BaTiO}_3$  single crystals. Our model provides the frequencies and activation energies of trapped charge carriers as the basis of this conduction mechanism, qualitatively accounting for the observed luminescence. This results also provides information on the relative amount of traps within the crystal.

Keywords:

Pyroelectricity, Luminescence, Poole-Frenkel effect, Fowler-Nordheim Tunneling

## LIST OF TABLES

Table 2.1	Parameters of Paschen's law .....	28
Table 3.1	Pyroelectric, electronic and geometric sample properties .....	69
Table 3.2	Temperature and time lag in the sample materials .....	71
Table 4.1	Fitting parameters of thermoluminescence model, LiNbO <sub>3</sub> .....	82
Table 4.2	Fitting parameters of thermoluminescence model, BaB <sub>2</sub> O <sub>4</sub> .....	86
Table 4.3	Fitting parameters of thermoluminescence model, BaTiO <sub>3</sub> .....	90
Table 4.4	SPEL model parameters for LiNbO <sub>3</sub> during cooling .....	99
Table 4.5	SPEL model parameters for the heating cycle of BaB <sub>2</sub> O <sub>3</sub> .....	102
Table 4.6	SPEL model parameters for the cooling cycle of BaB <sub>2</sub> O <sub>3</sub> .....	103
Table 4.7	Phase parameters in BaTiO <sub>3</sub> .....	105
Table 5.1	Comparison between TSL and SPEL .....	109
Table A.1	Fitting parameters of thermoluminescence model, LiNbO <sub>3</sub> , general order model .....	136
Table A.2	Fitting parameters of thermoluminescence model, BaB <sub>2</sub> O <sub>4</sub> general order model .....	137
Table A.3	Fitting parameters of thermoluminescence model, BaTiO <sub>3</sub> , general order model .....	138

# LIST OF FIGURES

Figure 1.1	Classification of luminescence phenomena .....	2
Figure 1.2	Overview between the relation between piezo- pyro- and ferroelectric crystals .....	5
Figure 1.3	Overview over the properties emerging from the various crystal classes.....	6
Figure 1.4	The piezoelectric effect .....	7
Figure 1.5	The pyroelectrically induced spontaneous polarization Ps .....	8
Figure 1.6	Change of pyroelectric polarization $\Delta P_s$ due to heating and cooling.....	9
Figure 1.7	Pyroelectric coefficient over temperature (schematic) .....	10
Figure 1.8	Permittivity over temperature (schematic).....	11
Figure 1.9	Schematic showing origin of spontaneous polarization .....	13
Figure 1.10	Schematic of a ferroelectric hysteresis loop .....	14
Figure 1.11	Pyroelectric luminescence of Type 1 and 2 of a coumarine crystal.....	17
Figure 1.12	Smooth pyroelectric luminescence (Type 3) of a coumarin crystal .....	17
Figure 2.1	Change of pyroelectric polarization $P_s$ and the resulting total polarization .....	21
Figure 2.2	Conduction and Discharge Mechanisms in Pyroelectrics .....	22
Figure 2.3	Schematic power band diagram of direct tunneling .....	24
Figure 2.4	Schematic power band diagram of Fowler-Nordheim (F-N) mechanism .....	25
Figure 2.5	Schematic power band diagrams of Thermionic (Schottky) mechanism .....	27
Figure 2.6	Paschen's law for common gas species .....	29
Figure 2.7	Energy diagram of the fluorescence process .....	31
Figure 2.8	Band diagram of thermally stimulated luminescence.....	33
Figure 2.9	Thermoluminescence glow curve of doped $\text{La}_2\text{O}_3$ , including peak fits .....	34
Figure 2.10	Polarization and agglomeration of surface charges shielding this polarization .....	36
Figure 2.11	Polaron generated by a self-trapped electron within the crystal.....	40
Figure 2.12	Polaron excitation and recombination.....	42
Figure 2.13	Poole-Frenkel barriers as a function of electric field .....	46
Figure 2.14	Change of the breakdown voltages in ambient gas .....	47
Figure 2.15	Detrapping mechanisms of electrons.....	53
Figure 3.1	Crystal structure and polarisation.....	55
Figure 3.2	$\text{LiNbO}_3$ band diagram – polaron excitation and relaxation.....	57
Figure 3.3	Phase diagram of $\text{Li}_2\text{O}-\text{Nb}_2\text{O}_5$ .....	58
Figure 3.4	Absorption coefficient, $\text{LiNbO}_3$ .....	59
Figure 3.5	$\text{BaB}_2\text{O}_4$ phase diagram .....	61
Figure 3.6	Tetragonal crystal structure of $\text{BaTiO}_3$ .....	62
Figure 3.7	Pyroelectric coefficient .....	63
Figure 3.8	Absorption coefficient, $\text{BaB}_2\text{O}_4$ .....	64
Figure 3.9	Ferroelectric switching in crystal structure of $\text{BaTiO}_3$ .....	65
Figure 3.10	$\text{BaTiO}_3$ phase transition .....	66
Figure 3.11	Absorption coefficient, $\text{BaTiO}_3$ .....	67
Figure 3.12	Experimental setup, schematic .....	68
Figure 3.13	Quantum efficiency of the Photon Counting Head.....	73
Figure 4.1	Emission during cooling in $\text{LiNbO}_3$ .....	76
Figure 4.2	Emission during cooling in $\text{BaB}_2\text{O}_4$ .....	77
Figure 4.3	TSL observed during the heating of $\text{LiNbO}_3$ .....	78
Figure 4.4	TSL observed during the heating of $\text{BaB}_2\text{O}_4$ .....	78
Figure 4.5	TSL emission during heating of $\text{LiNbO}_3$ .....	81
Figure 4.6	Arrhenius plot of the emission during the heating of $\text{LiNbO}_3$ .....	83
Figure 4.7	TSL emission during heating of $\text{BaB}_2\text{O}_4$ .....	85
Figure 4.8	Arrhenius plot of the emission during the heating of $\text{BaB}_2\text{O}_4$ .....	87
Figure 4.9	TSL emission during heating of $\text{BaTiO}_3$ (heuristic model) .....	89
Figure 4.10	Arrhenius plot of the emission during the heating of $\text{BaTiO}_3$ .....	91
Figure 4.11	Trap release mechanisms of electrons .....	94

Figure 4.12	LiNbO <sub>3</sub> SPEL emission during cooling.....	98
Figure 4.13	BaB <sub>2</sub> O <sub>3</sub> SPEL emission during heating.....	101
Figure 4.14	BaB <sub>2</sub> O <sub>3</sub> SPEL emission during cooling.....	102
Figure 4.15	Spontaneous polarization in BaTiO <sub>3</sub> .....	104
Figure 4.16	Barium Titanate: BaTiO <sub>3</sub> . Emission during heating. ....	105
Figure A.1	Energy diagram of the phosphorescence process.....	129
Figure A.2	Proposed mechanism for the regeneration of trapped states .....	130
Figure A.3	Trap conduction mechanisms (schematic).....	134
Figure A.4	LiNbO <sub>3</sub> , general order model.....	136
Figure A.5	BaB <sub>2</sub> O <sub>4</sub> general order model .....	137
Figure A.6	BaTiO <sub>3</sub> , general order model.....	138
Figure A.7	Pyroelectric Luminescence, cooling of BaTiO <sub>3</sub> .....	139

# TABLE OF CONTENTS

Acknowledgements .....	i
Résumé.....	ii
Abstract .....	iii
List of Tables.....	iv
List of Figures.....	v
Table of Contents.....	vii
<b>1      Introduction .....</b>	<b>1</b>
1.1 <i>Motivation</i> .....	3
1.2 <i>Electric Ordering in Crystals</i> .....	4
1.2.1    Piezoelectricity .....	6
1.2.2    Pyroelectricity .....	7
1.2.3    Ferroelectricity.....	11
1.3 <i>Historical background</i> .....	14
1.4 <i>Applications of luminescence</i> .....	15
1.5 <i>State of the art – present research</i> .....	16
1.5.1    Thermoluminescence and Pyroelectric Luminescence.....	16
1.5.2    Investigated Ferroelectric Materials.....	18
1.6 <i>Research Objectives</i> .....	19
<b>2      Fundamentals .....</b>	<b>20</b>
2.1 <i>Pyroelectric polarization and surface charge</i> .....	20
2.2 <i>Conduction and Discharge Mechanisms in Pyroelectrics</i> .....	21
2.2.1    Direct Tunneling and Hopping Conduction.....	22
2.2.2    Fowler-Nordheim Tunneling .....	24
2.2.3    Schottky Emission and Poole-Frenkel Emission .....	25
2.2.4    Gas discharge: Paschen's law .....	27
2.3 <i>Overview of Luminescence phenomena</i> .....	29
2.3.1    Thermally stimulated luminescence .....	32
2.3.2    Pyroelectric luminescence .....	35
2.3.3    Optical excitation of a bulk crystal.....	39
2.3.4    Polaron and trapped charges .....	40
2.4 <i>Models of Thermoluminescence</i> .....	42
2.4.1    Arrhenius Law .....	42
2.4.2    First order kinetic glow peaks.....	44
2.5 <i>Conduction in Pyroelectric Crystals</i> .....	45
2.5.1    Pyroelectric Crystal Discharge Mechanism.....	46
2.5.2    Poole-Frenkel emission .....	47

2.5.3	Coulombic potential .....	48
2.5.4	Dirac potential .....	51
2.5.5	Fowler-Nordheim Tunneling of trapped charges .....	52
<b>3</b>	<b>Materials and methods .....</b>	<b>54</b>
3.1	<i>Materials</i> .....	54
3.1.1	Lithium Niobate .....	54
3.1.2	Barium Metaborate .....	59
3.1.3	Barium Titanate .....	65
3.2	<i>Experimental Setup</i> .....	68
3.2.1	Sample preparation .....	69
3.2.2	Temperature-controlled Cryostat.....	70
3.2.3	Heat transfer and time delay within the crystal .....	70
3.2.4	Measurement of Thermostimulated Luminescence.....	71
3.2.1	Photomultiplier tube quantum efficiency.....	72
3.2.2	Electric field measurement.....	73
<b>4</b>	<b>Results .....</b>	<b>75</b>
4.1	<i>Qualitative Overview</i> .....	75
4.2	<i>Density of occupied traps</i> .....	79
4.3	<i>Models of Thermostimulated Luminescence</i> .....	79
4.4	<i>Experimental results of Thermostimulated Luminescence</i> .....	80
4.4.1	Lithium Niobate .....	80
4.4.2	Beta Barium Borate.....	84
4.4.3	Barium Titanate .....	88
4.5	<i>Model of Smooth Pyroelectric Luminescence</i> .....	92
4.6	<i>Experimental results of SPEL</i> .....	96
4.6.1	Lithium Niobate .....	96
4.6.2	Beta-Barium Borate .....	99
4.6.3	Barium Titanate: Luminescence during phase transitions .....	103
<b>5</b>	<b>Summary and Conclusion .....</b>	<b>107</b>
5.1	<i>Summary</i> .....	107
5.2	<i>Conclusion and Outlook</i> .....	109
<b>6</b>	<b>References.....</b>	<b>111</b>
<b>Appendix</b>	<b>.....</b>	<b>129</b>
<b>A.1</b>	<b>Theory of regeneration of trapped states without UV.....</b>	<b>129</b>
A.1.1	Jablonski Diagram of Phosphorescence.....	129

A.1.2	<i>Hypothetical model of regenerating traps</i> .....	130
A.2	<b>Derivation of Trap Depletion by Arrhenius' law</b> .....	131
A.3	<b>Estimation of conductivity as observed by the emission rate</b> .....	132
A.4	<b>Trap-based conduction mechanisms (schematic)</b> .....	134
A.5	<b>General Order Thermoluminescence</b> .....	135
A.5.1	<i>General Order Fits</i> .....	136
A.6	<b>Pyroelectric Luminescence of BaTiO<sub>3</sub></b> .....	139
<b>Luminescence pyroélectrique continue dans le niobate de lithium, le beta borate de baryum et le titanate de baryum</b> .....		140
1	<b>Introduction</b> .....	141
1.1	<i>La luminescence thermiquement stimulée</i> .....	143
1.2	<i>La luminescence pyroélectrique</i> .....	146
1.3	<i>Objectifs de cette thèse</i> .....	149
2	<b>Méthodologie</b> .....	150
2.1	<i>Matériaux</i> .....	151
2.1.1	Titanate de baryum.....	151
2.1.2	Niobate de lithium .....	152
2.1.3	Beta-baryum borate .....	152
3	<b>Résultats</b> .....	152
3.1	<i>Conclusions</i> .....	157
3.2	<i>Perspectives</i> .....	159

# Chapter 1

## 1 INTRODUCTION

Luminescence is "cold light", light from non-thermal sources of energy. It is driven by a variety of energy sources not directly related to thermal radiation. Luminescence is widely used in day-to-day appliances, and also represents a class of well-established analytical techniques in material science [1]. Luminescence is commonly classified into two parts based on its duration of emission: On one hand, fluorescence, which decays typically in nanoseconds, and phosphorescence on the timescales longer than microseconds. Furthermore, Thermostimulated luminescence (TSL) is a kind of fluorescence that is thermally activated, and thus highly dependent on temperature.

Certain materials have been demonstrated to show emission dependent not only on temperature, but changes in temperature. This behavoir has been linked to the pyroelectricity of studied materials, that generate an electric field upon temperature changes. This electrically induced promotion of emission has been termed pyroelectroluminescence (PEL) or thermally stimulated field emission (TSFE) [2]. This phenonenon is clearly distinguished from pure thermoluminescence in that it may also emit light during a cooling cycle. An overview of the classification of luminescence phenomena is shown in Figure 1.1.

Smooth pyroelectric Luminescence (SPEL) is a special case of TSFE, where a pyroelectric material can produce its own electric field to assist the release of the contained trapped charges. Compared to TSL, SPEL is thought to be able to release trapped charges that are inaccessible to pure thermal activation due to their high activating energy. A related technique to SPEL is electrostimulated thermoluminescence, which operates on the same physical mechanism, but uses an externally generated field.[3]

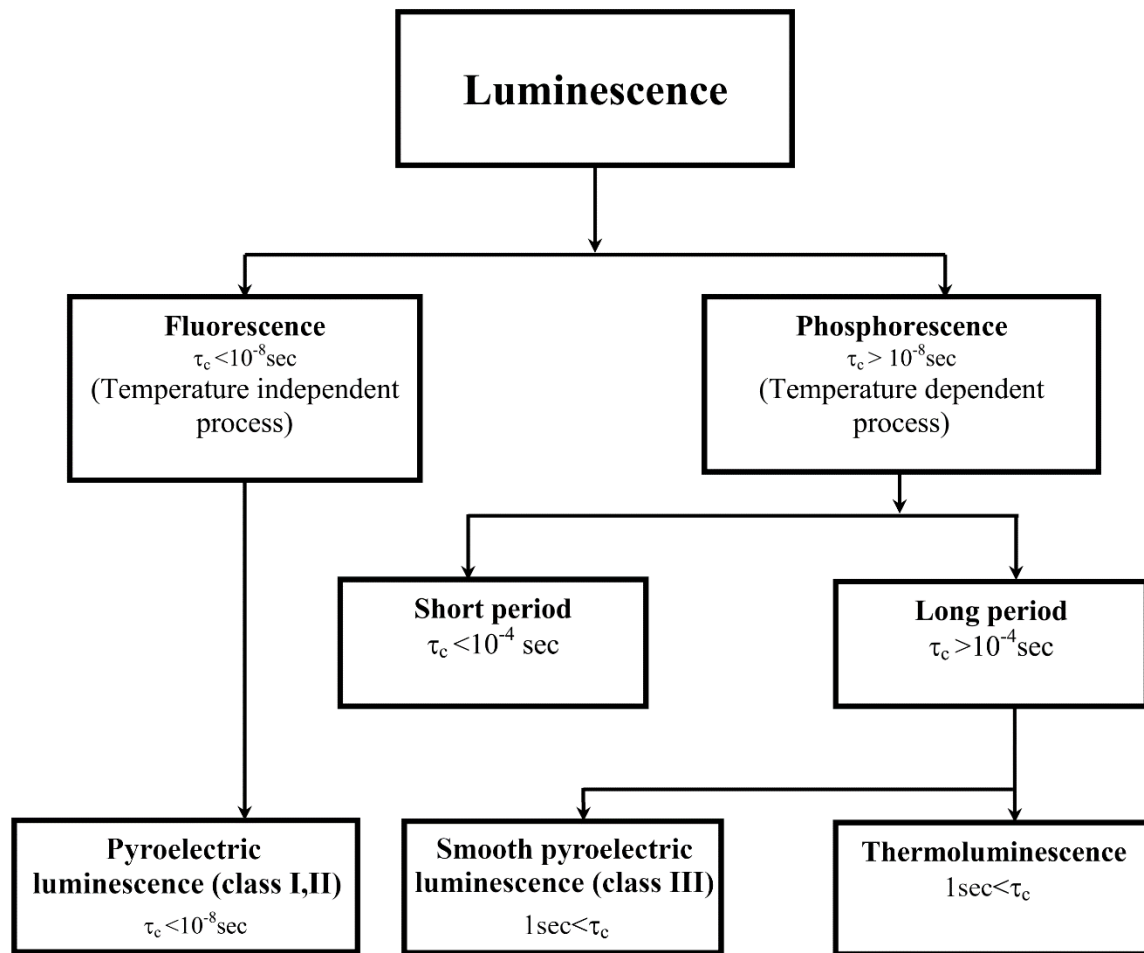


**Figure 1.1** Classification of luminescence phenomena. The pyroelectric luminescence types are restricted non-centrosymmetric pyroelectric crystals. Adapted from Ref. [4]

A variety of technical applications, which serve to investigate different material properties such as crystal defects in semiconductors. Indeed, a wide range of experimental methods has been used to study crystal defects [5].

## 1.1 Motivation

Thermostimulated luminescence (TSL) is a phenomenon that occurs in a wide variety of semiconductors and insulators [5]. It provides insights about the electronic structure, more specific, the characteristics of charge traps within the material, such as defects or polarons. The smooth pyroelectric luminescence (SPEL) is a related phenomenon that applies to pyroelectric materials. Besides the temperature, the SPEL is induced by the electric field. This allows for the activation of deeper traps within the studied material, but also permits an investigation at reduced temperatures. These traps levels can be activated by the combined effect of temperature and electric field. Despite the potential benefits, the technique has only sparsely been studied, which may be attributed to its increased technical requirements. This makes it a field of study that is not explored very well, which includes the application of this technique to some of the most widely used pyroelectric materials.

Besides the activation energy of traps, SPEL can provide insights about the trap density as well as their contribution to leakage currents under high electric fields. Additionally, we investigate the relationship between the SPEL and phase transitions. The dependence between temperature and electric field can also provide insights into the trap properties and physical mechanism of the release of SPEL emission.

We focus in our work on three materials of major technological and industrial interest: Lithium niobate ( $\text{LiNbO}_3$ ), beta barium borate ( $\text{BaB}_2\text{O}_4$ ) and barium titanate ( $\text{BaTiO}_3$ ). Both  $\text{LiNbO}_3$  and  $\text{BaB}_2\text{O}_4$  are heavily used in nonlinear optics, including applications such as higher harmonics generation and optical parametric oscillators [6], [7].  $\text{LiNbO}_3$  is especially popular for electromechanical transducers, such as surface acoustic wave filters [8] due to its large piezoelectric coefficient.  $\text{BaTiO}_3$  has a large dielectric permittivity, which makes it an ideal material for capacitor applications. Besides that, it is also used in electromechanical transducers, nonlinear optics [9], as well as a photocatalyst as nanoparticles [10]. Common applications of pyroelectrics include infrared detectors, motion sensors, energy harvesting [11] [6] [7], temperature sensors [14], thermal imaging [15] and catalytic converters [16].

## 1.2 Electric Ordering in Crystals

The polarization in dielectric crystals describes a displacement between positive and negative charges. Polarization is a result of alignment of the electric dipole moments in certain classes of materials lacking center of symmetry or inversion center [17], [18]. There exist a total of 32 crystal point symmetry groups (see Figure 1.3). These 32 point groups contain 21 non-centrosymmetric, out of which 20 polarizable groups (point group 432 is cubic).

Of these, there are 10 with a unique polar axis and therefore, may exhibit spontaneous electric polarization ( $P_s$ ) that persists independent of any external electric field. Some examples include the groups 1, 2, m, 2mm, 3, 3m, 4, 4mm, 6 and 6mm.

These 10 groups are pyroelectrics, out of which some exhibit ferroelectric properties, meaning that their polarization can be switched under the effect of an external electric field. We detail these in the next sections.

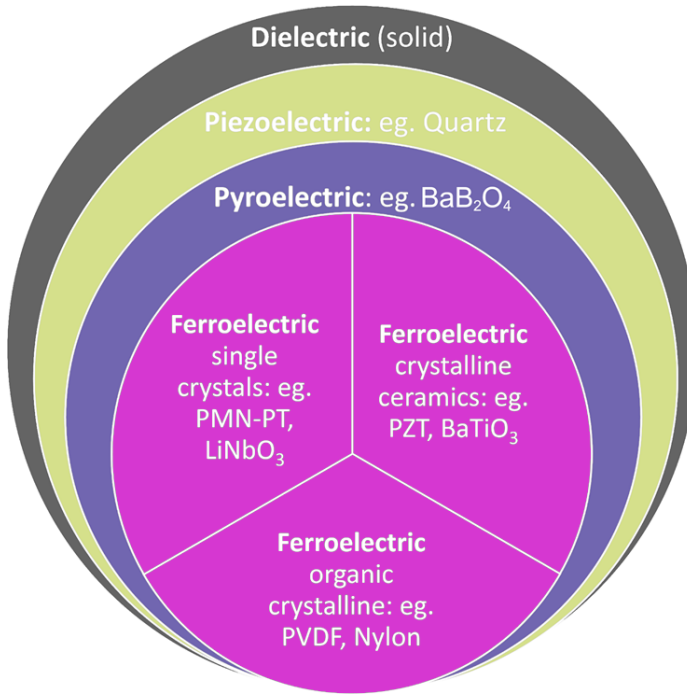


**Figure 1.2** Overview between the relation between piezo- pyro- and ferroelectric crystals. Inner circles have additional properties compared to their outer group, and include all of their properties.[19].

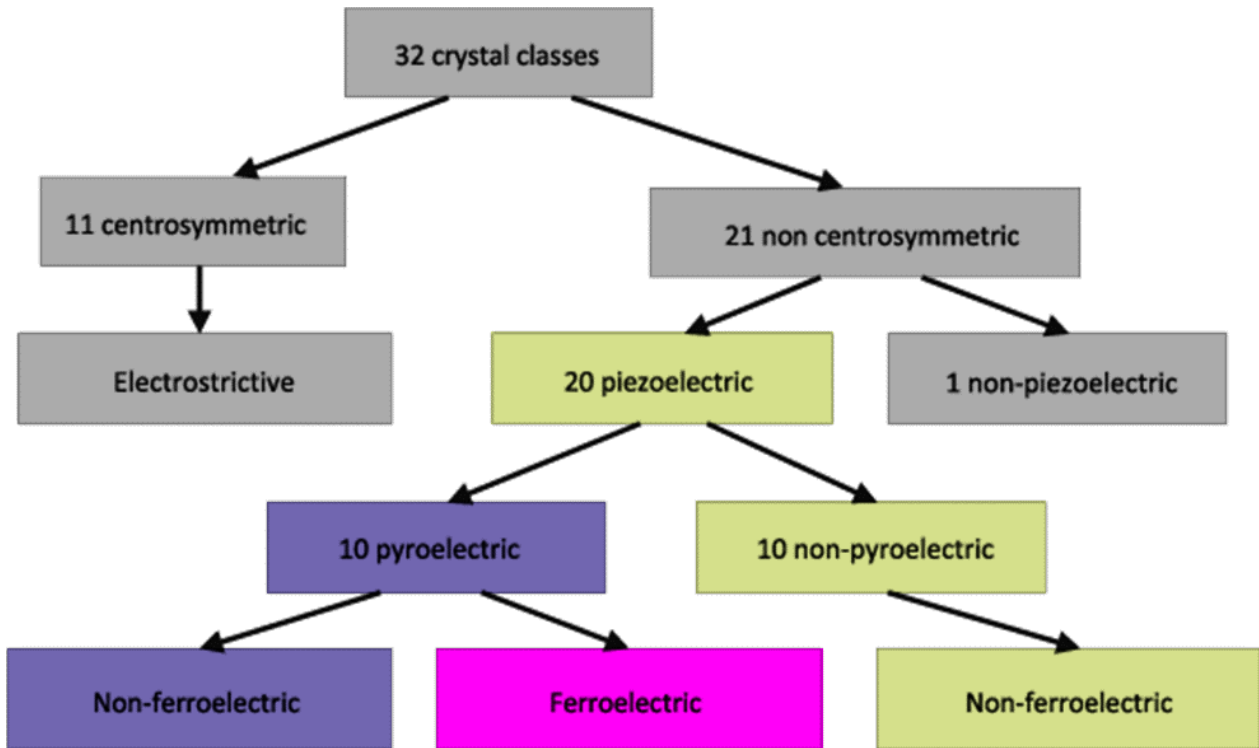


**Figure 1.3** Overview over the properties emerging from the various crystal classes. There exist a total of 32 crystal classes, which are categorized according to their physical properties. [20]

### 1.2.1 Piezoelectricity

The crystals that exhibit polarization ( $p_i$ ) depending on mechanical stress ( $\sigma_{jk}$ ) are called piezoelectrics. This phenomenon works in both directions: Exposure to external stress creates polarization, and exposure to an external electric field ( $E_i$ ) creates mechanical stress. The first one is called the direct piezoelectric effect, the latter the converse piezoelectric effect [17], [18]. They can be expressed as

$$\Delta P_i = d_{ijk} \sigma_{jk} \quad (1.1)$$

where  $d_{ijk}$  is the piezoelectric coefficient, a third rank tensor, and  $\varepsilon_{jk}$  the strain tensor.  
The converse effect

$$\varepsilon_{jk} = d_{ijk}E_i \quad (1.2)$$

and  $d_{ijk}$  is the coefficient of the converse effect.

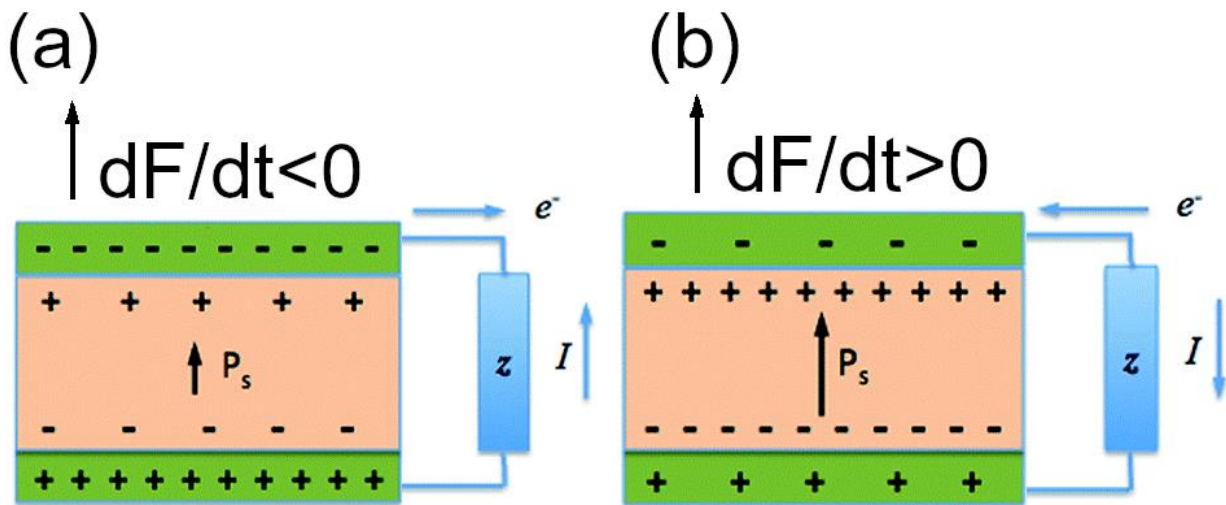


**Figure 1.4** The piezoelectric effect [2 1] The resistor  $z$  symbolizes the leakage current  $I$ . (a) A decreasing force in tensile direction lowers the spontaneous polarization. The induced leakage currents compensate for the lower amount of shielding charges required on the crystal surface. (b) An increasing force enlarges the spontaneous polarization, causing additional shielding charges to leak to the surface.

### 1.2.2 Pyroelectricity

Crystals that change spontaneous polarization along a polar axis as a function of temperature are called pyroelectrics. The spontaneous polarization is quantified as a

surface charge density. While this temperature-charge coupling is typically linear, highly nonlinear cases occur when approaching the temperature of phase transitions between pyroelectric phases.

The pyroelectric effect can be quantified by a polarization change with temperature [18]

$$\Delta P_i = \gamma_i \Delta T \text{ for } i=1,2,3 \quad (1.3)$$

where  $\gamma_i$  are the pyroelectric coefficients. Applications of pyroelectrics include temperature sensors, energy harvesters[12], [13], amongst others.

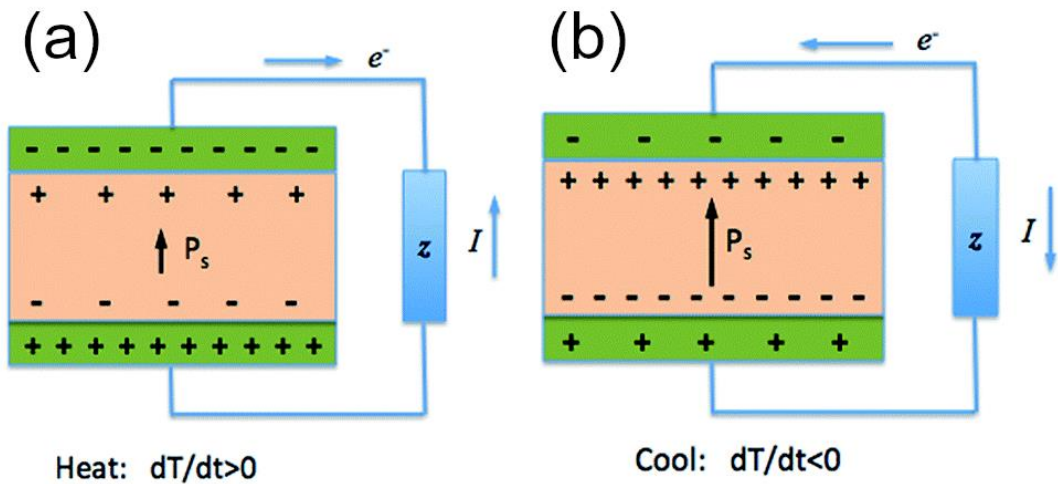


**Figure 1.5** The pyroelectrically induced spontaneous polarization  $P_s$  and its relation to the induced electric field. The resistor  $z$  symbolizes the leakage current  $I$ . Higher temperatures can lead to increased leakage currents, leading to reduced net polarization. Since leakage is a time-dependent process, fast temperature changes at low temperatures may generate the largest fields. (a) Heating generally lowers  $P_s$ , inducing a leakage current parallel to  $P_s$ . (b) cooling causes increased  $P_s$  and an antiparallel current. [20]

The structural mechanism that forms the spontaneous polarization without an external electric field is found in the crystal structure [22]. The polarization can be found in ionic bonds, due to a relative shift in opposite charged ions, and in polarized covalent bonds, that can change their alignment [23].

With increasing temperatures, the spontaneous polarization within the pyroelectric decreases due to an increasing loss of orientation caused by thermal vibrations. Correspondingly, decreasing temperatures allow the dipoles to regain their orientation leading to an increase in the level of spontaneous polarization.[24]

The effects of cooling and heating on the spontaneous polarization are visualized in Figure 1.6.

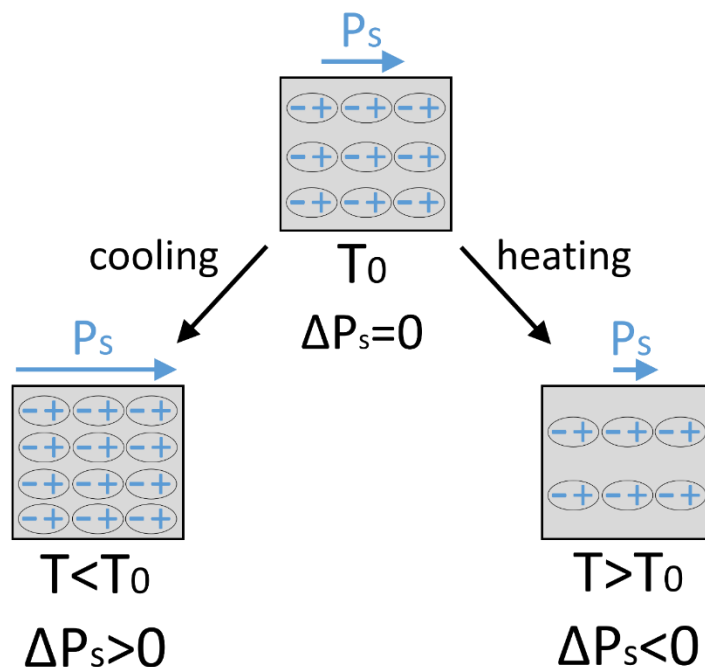


**Figure 1.6** Change of pyroelectric polarization  $\Delta P_s$  due to heating and cooling. When the temperature increases and approaches the Curie temperature, the spontaneous polarization decreases.

The temperature that extinguishes the pyroelectric property is called Curie temperature (see Figure 1.7). Only certain materials can reach this temperature due to other thermal constraints.

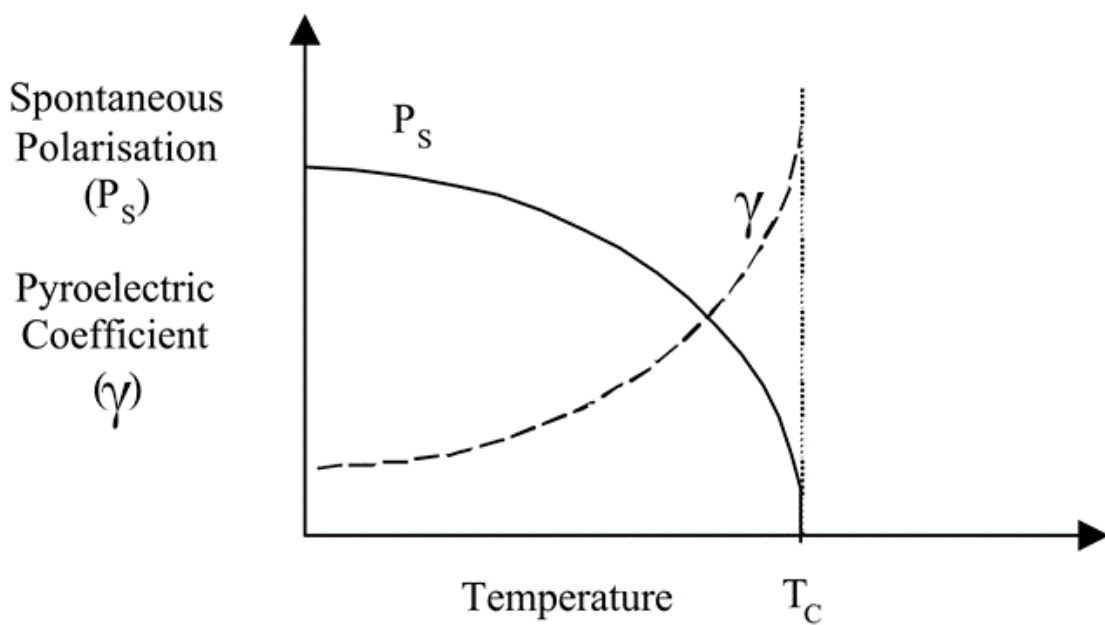


**Figure 1.7** Pyroelectric coefficient over temperature (schematic). When the temperature increases and approaches the Curie temperature, the spontaneous polarization decreases. Due to the increasing slope, the pyroelectric coefficient increases (dashed line) [23].

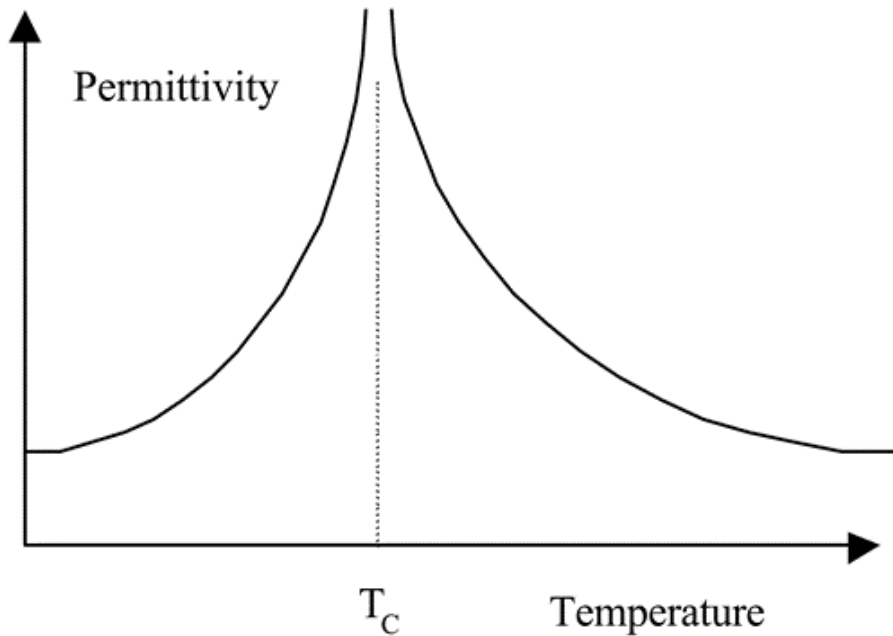


**Figure 1.8** Permittivity over temperature (schematic). The permittivity becomes very large near  $T_c$  [23].

### 1.2.3 Ferroelectricity

Ferroelectricity is the spontaneous formation of polarization  $P_{s,i}$  in a material, which can be reoriented by application of an external electric field [25]. Amongst the piezo- and pyroelectric contributions, the ferroelectric material has an additional contribution of spontaneous polarization  $P_{s,i}$ . In contrast to the quasi-permanent polarization of electrets, the polarization states in ferroelectrics are thermodynamically stable [26]. The spontaneous polarization occurs when the temperature decreases below a critical point (Curie temperature,  $T_c$ ), triggering a phase transition from the high temperature paraelectric (centrosymmetric) to a low temperature ferroelectric (without inversion symmetry) [27] (Figure 1.9a).

The alignment of the spontaneous is not necessarily uniform: Two opposing forces balance to minimise the overall energy of the system. One is the depolarising field of bound charges of spontaneous polarization on the surface of the crystal, and the second is the energy of domain boundaries. As a result of this, we typically see regions of distinct dipole alignment separated by other regions of dipole alignment separated by a boundary. These regions of dipole alignment are known as domains and the boundary separating two different regions are called domain walls, as shown in Figure 1.9b.

The combined dipole moment of a ferroelectric crystal is the sum over the individual dipole moments of all domains of the crystal. Without an external electric field, the crystal is apparently unpolarised. As a consequence, domains with dipoles parallel to the direction of the applied field grow at the expense of those with different alignments, generating a net dipole moment. This process can be inverted by changing the polarization of the external electric field, constituting the characteristic ferroelectric hysteresis [28] (see Figure 1.10a).

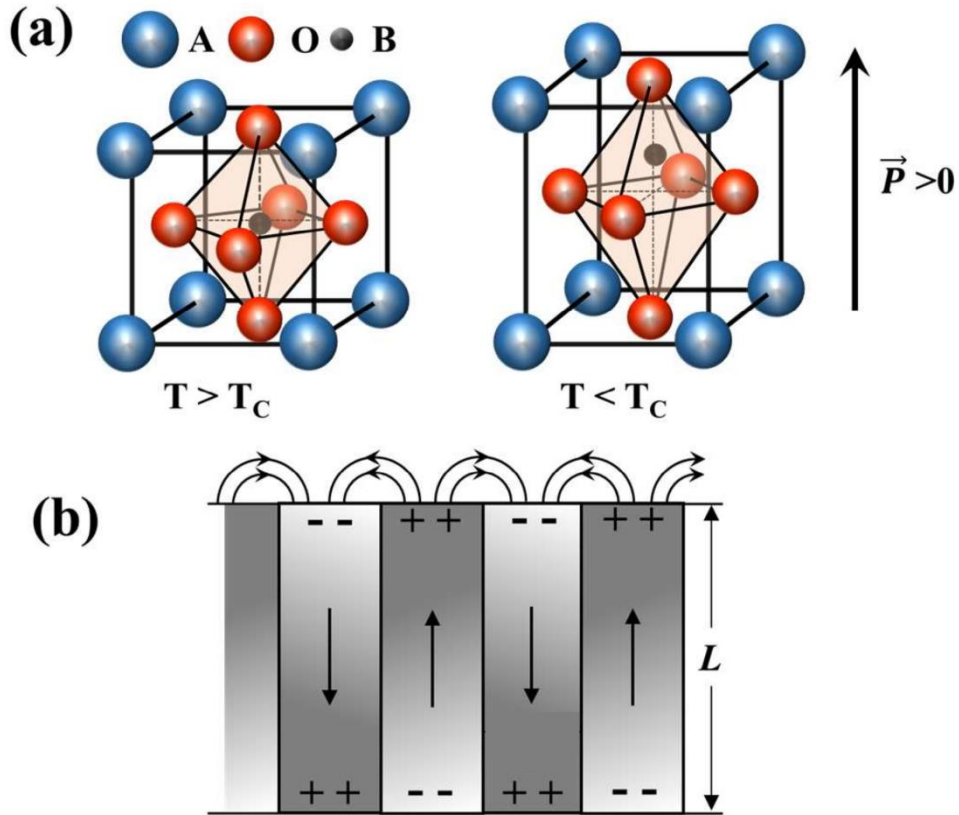


**Figure 1.9** Schematic showing origin of spontaneous polarization (a) in  $\text{ABO}_3$  type perovskite compound below Curie temperature. (b) Schematic of 180° domain structure in a ferroelectric [28].

Ferroelectrics have at least two minima of free energy corresponding to the spontaneous polarization directions. The barrier separating these states can be overcome by a sufficiently high electric field. [25]. Due to the interaction between the domains in the crystal, the switching process is in general rather complex [26]. As shown schematically in Figure 1.10b,

Stage I shows the initiation of nucleation of domains parallel to the applied field. In Stage II, a rapid expansion parallel to the field takes place, which then proceeds into a creeping sideways growth in Stage III. This process can continue until the full domain is occupied.

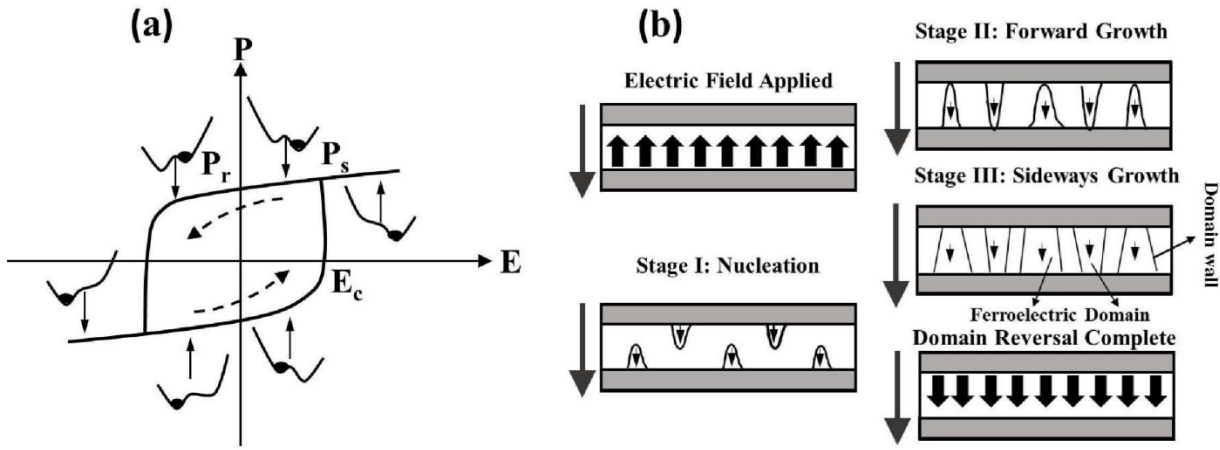


**Figure 1.10** Schematic of a ferroelectric hysteresis loop. (a)  $P_r$ , and  $P_s$ , represent remnant and spontaneous polarization;  $E_c$  is the coercive field. (b) Schematic of three phases of domain reversal: (i) nucleation of domains aligned to electric field (fast), (ii) forward growth of domains (fast) (iii) sidewise growth of domain. Arrows represent electric field ( $E$ ) direction [25][26].

### 1.3 Historical background

Ferroelectricity was first observed in Rochelle salt in 1921. [29], [30]. Within a few decades, related properties such as polarization, dielectric constant and strain were investigated and consecutive models explaining their relation to ferroelectricity were developed, including theories accounting for anomalous dielectric, piezoelectric, elastic, and phase transition behaviors emerged [29][31]. The later decades saw the emergence of another group of ferroelectric materials based on  $\text{KH}_2\text{PO}_4$  and a theory of phase transition was developed [32]. The discovery of ferroelectricity in some perovskite-structured compounds such as  $\text{BaTiO}_3$ , in the 1940s was a major breakthrough, as these compounds had simple structures and could be easily manufactured and investigated [33].

In 1969 Schmidt and Petersson [34] observed electric sparks in ferroelectric triglycine sulfate (TGS). In 1975, Yockey and Aseltine [35] reported about high voltage discharges after  $\gamma$ -irradiation of other ferroelectrics like Rochelle salt, guanidinium aluminium sulfate hexahydrate (GASH) and potassium dihydrogen phosphate (KDP) induced by changing temperatures. Only one year later, Cooke and Alexander [36] showed that irradiation with  $\gamma$ -rays is not required for the observation of discharges. Later, several other publications followed reporting this type of luminescence in tourmaline [37],  $\text{LiNbO}_3$  [38][39], proustite and pyrargyrite [40], sodium nitrite and ammonium tartrate [41], N-isopropyl carbazole [42] and various other materials [43].

The term 'pyroelectric luminescence' (PEL) was coined by Patel and Hanson [43] in 1981 for both the spike-like discharges through the ambient atmosphere, and a smooth emission slowly varying with temperature and consequently with time. For brevity we shall refer to this second type as smooth pyroelectric luminescence as SPEL.

The spike-like discharges and their dependence on ambient gas, atmosphere pressure and heating rate have been clarified in detail by Dreger and Kalinowski [42].

As opposed to thermoluminescence, pyroelectric luminescence is also observable upon cooling. The temperature changes induce an electric field, which allows the phenomenon to be observed during both cooling and heating cycles. It is believed to be based on the same recombination mechanism as electroluminescence, yet it does not require an external circuit in order to introduce charge carriers [44].

## 1.4 Applications of luminescence

The ability of pyroelectrics to convert temperature changes to a voltage is commonly used in infrared detectors including motion sensors, as well as energy harvesting.[11] [12], [13] Furthermore, applications include temperature sensors[14], thermal imaging[15], catalytic converters[16], amongst others.

Materials that exhibit thermostimulated luminescence are commonly used in radiation dosimetry, where the emitted light is a measure for the total quantity of absorbed radiation. It is also used in archeological dating of inorganic materials, a technique that is complementary to radiocarbon dating [45]. Furthermore, it is a highly sensitive tool to study defects and has found application in material science. [4], [46]. A range of example applications can be found in Mihóková and Nikl [47]. Pyrostimulated luminescence combines the properties of pyroelectrics with luminescence, coupling the emission of light to the electric field.

## 1.5 State of the art – present research

### 1.5.1 Thermoluminescence and Pyroelectric Luminescence

The observed phenomenon of pyroelectric luminescence is classically split into three categories, depending on the gas pressure of the environment [44][43]: Class I luminescence is characterized by a series of electrical discharges due to the dielectric breakdown ionizing the surrounding gas. This behavior generally occurs when the pressure of the ambient atmosphere is above 1 mbar.

Class II luminescence is similar to class I and characterized by more frequent and less intense pulses. It is generally found to occur when the pressure of the ambient atmosphere is between 1 mbar and  $10^{-3}$  mbar. An example of this luminescence type is shown in Figure 1.11.

According to Patel and Hanson 1981[43] who first demonstrated pyroelectric emission in coumarin, we distinguish three different emission types. Depending on the ambient pressure, three different types of this phenomenon can be observed.

Below  $10^{-3}$  mbar, electric discharges eventually cease and in certain materials, a steady, slowly changing glow is observable as the temperature changes. This phenomenon is termed class III luminescence (see Figure 1.12). The luminescence glow varies gradually over a relatively narrow temperature range, and peaks at a temperature characteristic of the crystal under investigation [48]–[51]. The understanding of this phenomenon still incomplete. It is attributed to charge carrier recombination processes occurring inside the

crystal and has, since the early reports been suspected to involve defect states [43], [44], [52].

The gradual shift between class I over class II to class III is explained by the reduction of the electrical breakdown field due to Paschen's law. The mechanism of class III is still not fully understood, although past studies have proposed a relation to defects, such as the work by Nelson et al [44] and Patel et al [43]. The faint, continuous emission is also known as smooth pyroelectric luminescence (SPEL).

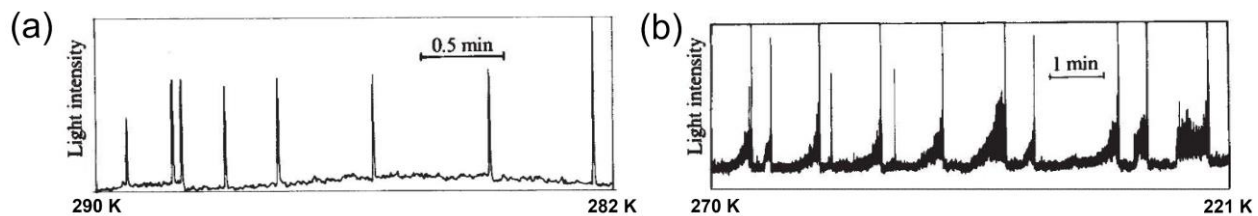


**Figure 1.11** Pyroelectric luminescence of Type 1 and 2 of a coumarine crystal, (a) Type 1 under pressure ( $10^3$  mbar) during cooling the light emission consists of consecutive sparks. (b) Type 2 at reduced pressure  $10^{-3}$  mbar during cooling the light emission consists of low intensity sparks with high frequency[41].

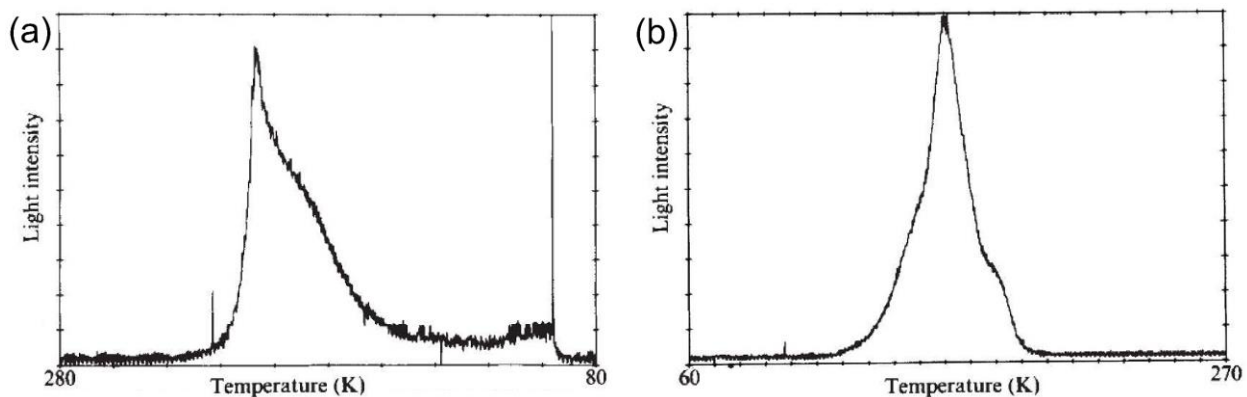


**Figure 1.12** Smooth pyroelectric luminescence (Type 3) of a coumarin crystal (a) during the cooling cycle and (b) during the heating cycle. The pressure is given as  $7 \times 10^{-5}$  mbar. [41].

While thermoluminescence is frequently investigated in literature [53], pyroelectric luminescence which also takes into account the effects of pyroelectrically induced fields is rarely mentioned.

The current methods describing thermoluminescence are first-order kinetics glow-curves [54], which do not take into account this pyroelectric effect. This has previously led to unphysical parameter estimations, for example by the work of R. Singh et al., 2017 [53].

A precise description of the mechanisms involved in smooth pyroelectric luminescence in the aforementioned materials remains unknown. Our research focuses on explaining this process in detail, and shows how critical material parameters can be obtained from the emission signature.

Examples of the materials that have previously been observed to show SPEL include m-bromonitrobenzene[44], coumarin[43], and  $\text{Sn}_2\text{P}_2\text{S}_6$  [55]. Although pyroelectric discharges in  $\text{LiNbO}_3$  [56] and  $\beta\text{-BaB}_2\text{O}_4$  [57] have been observed, the presence of SPEL is yet to be demonstrated for both materials.

### 1.5.2 Investigated Ferroelectric Materials

In this section, we summarize the key characteristics of the three materials that we investigate in this thesis: lithium niobate ( $\text{LiNbO}_3$ ), Barium Metaborate ( $\beta\text{-BaB}_2\text{O}_4$ ) and the ferroelectric phase of barium titanate ( $\text{BaTiO}_3$ ). All three materials have not been extensively studied with regards to their pyroelectric luminescence properties.

Lithium niobate is a pyroelectric, which can also show ferroelectric behavior in certain cases [7]. It is commonly used in second harmonic generation, electro-optic modulation, as well as acousto-optic and piezoelectric devices. Especially the piezoelectric properties are an important domain of research for the improvement of surface acoustic wave filters [8]. Doped  $\text{LiNbO}_3$ , such as  $\text{MgO}:\text{LiNbO}_3$  has been studied by infrared spectroscopy[58]. Various dopants of  $\text{LiNbO}_3$ , such as  $\text{Sm}^{3+}$ ,  $\text{Tb}^{3+}$ , or  $\text{Dy}^{3+}$  ions have been investigated by thermoluminescence [59].

Barium betaborate is the ferroelectric phase of barium metaborate. Its non-linear optical properties have been widely investigated [32]–[35], while its pyro- and piezoelectric properties are not conclusively understood [57], [60], [61]. Its relatively large pyroelectric coefficient of 12-15  $\mu\text{C}/(\text{Km}^2)$  [60][61] lends itself to the investigation of analysis by pyroelectric luminescence. Adamiv et al. [57] described isolated flashes coinciding with pyroelectric current oscillations in the range of 80-400 K below  $10^{-1}$ - $10^{-2}$  mbar. They showed that intensity and repetition frequency could be modulated by the heating rate and ambient pressure, both of which affect the buildup of electric fields within the crystals. Barium  $\beta$ -borate ( $\text{BaB}_2\text{O}_4$ ) has not been studied with regards to its pyroluminescence or electroluminescence properties.

Barium titanate is a perovskite ferroelectric which forms rhombohedral, orthorhombic, tetragonal and cubic crystals, depending on temperature. Its bulk structure is typically non stoichiometric and it exhibits a very large dielectric constant.[62] While there exist articles about thermostimulated luminescence [63], [64] and electroluminescence [65], the material has not yet been investigated using pyroelectric luminescence.

## 1.6 Research Objectives

The aim of this work is to study pyroelectric crystals in  $\text{LiNbO}_3$ ,  $\beta\text{-BaB}_2\text{O}_4$ ,  $\text{BaTiO}_3$  and show the feasibility of generating smooth pyroelectric emissions with the various materials, in order to establish a novel method for the characterization of defect properties and trapped charges, such as their activating energies. To attain this, a measurement setup is developed, which probes the crystal luminescence under varying temperatures and pyroelectrically generated fields. To obtain quantitative results, the measurement of the electric field within a confined vacuum cryostat was required. Based on the setup, a qualitative understanding of the physical processes, as well as a novel quantitative investigation of the pyroelectric luminescence was to be developed. To attain this, a numerical model describing the observed phenomenon was required.

With regards to  $\text{BaTiO}_3$ , the relationship between the phase transition and its relation to the luminescence signal was investigated as a secondary result.

# Chapter 2

## 2 FUNDAMENTALS

In this chapter, we present an overview over the physical topics relevant for the thermos- and pyroluminescence phenomena, ranging from the pyroelectric material polarization under vacuum conditions, the resulting high-voltage conduction mechanisms, as well as the band states responsible for luminescence, as well as polarons. With this basis, we explain the quantitative modeling of the observed luminescence curves by different models.

### 2.1 Pyroelectric polarization and surface charge

The change of pyroelectric polarization  $P_s$  and the resulting total polarization is schematically shown in Figure 2.1.

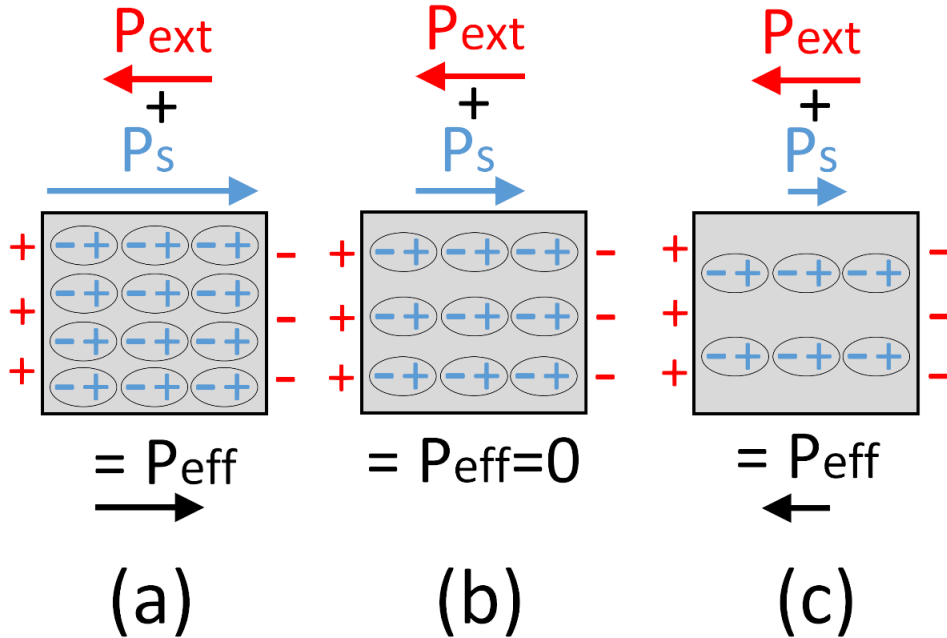


**Figure 2.1** Change of pyroelectric polarization  $P_s$  and the resulting total polarization. (b) Neutralized polarization, e.g. due to short-circuiting the opposing surfaces. (a) Decreased temperature with respect to (b) under insulated conditions: The spontaneous polarization increases, yielding an effective (total) polarization. (c) Increased temperature with respect to (b). The increased temperature lowers the spontaneous polarization, resulting in an effective polarization opposite to case (a).

## 2.2 Conduction and Discharge Mechanisms in Pyroelectrics

There exist a large amount of possible conduction mechanisms in dielectric crystals, some of which are shown in Figure 2.2, only some of them allowing for luminescence. We describe two key mechanisms for luminescence: First, the release of a trapped electron into an elevated energy state, allowing the subsequent emitting relaxation into the valence band. Second, the discharge of surface-bound electrons through the ambient atmosphere.

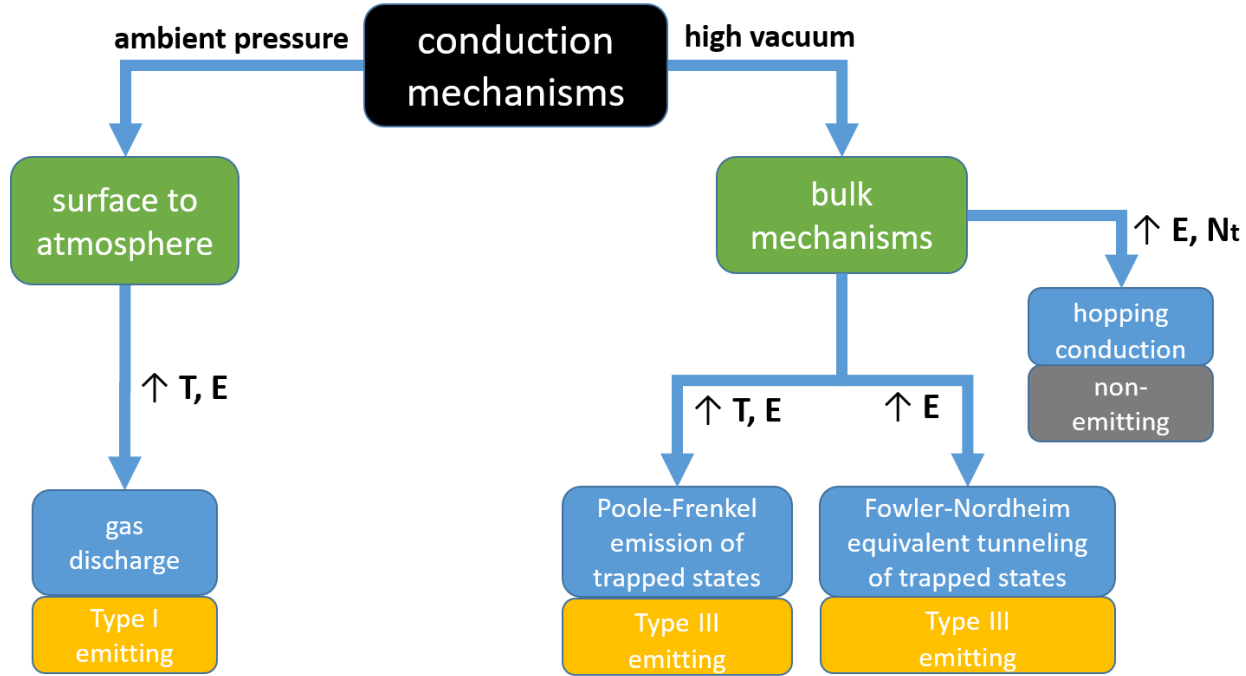


**Figure 2.2 Conduction and Discharge Mechanisms in Pyroelectrics**

This bulk bound conduction through the pyroelectric crystal requires a buildup of high electric fields due to temperature changes, thus requiring vacuum, and trap defects in an energy range amenable to release by a combination of strong electric fields and temperature.

### 2.2.1 Direct Tunneling and Hopping Conduction

The non-scattering tunneling through a potential barrier of fixed width is described by direct tunneling (Figure 2.3). The simplest approximation of direct tunneling current density is given by Gruverman *et al.*, 2019 [66].

$$J_{DT}(E) = \frac{q^2}{h^2} \sqrt{2m^*\varphi} \exp\left[-4\pi d \frac{\sqrt{2m^*\varphi}}{h}\right] E \quad (2.1)$$

where  $\varphi$  is the effective potential barrier height,  $d$  is the tunneling distance,  $m^*$  is the reduced electron mass, and  $E$  is the electric field.

Hopping conduction is due to the tunneling effect of trapped electrons between trap sites to another in dielectric materials. The energy band diagram of hopping conduction as compared to the Poole-Frenkel mechanism is shown in Figure A.3 (left).

The current density is given by [67]

$$J(E, T) = q n a \Gamma(E, T) \quad (2.2)$$

where the hopping rate between traps is [67]

$$\Gamma(E, T) = \nu \exp\left(\frac{qaE}{k_B T} - \frac{W_a}{k_B T}\right) \quad (2.3)$$

where  $a$  is the mean hopping distance (i.e., the mean spacing between trap sites),  $n$  is the electron density in traps,  $\nu$  is the frequency of thermal vibration of electrons at trap sites, and  $W_a$  is the activation energy between trap and conduction band.

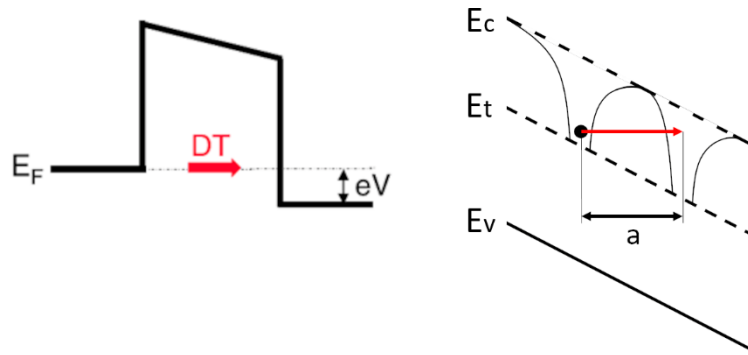


**Figure 2.3** Schematic power band diagram of direct tunneling. The trap hopping mechanism (right) is the bulk-limited analogue. Adapted from [68].

### 2.2.2 Fowler-Nordheim Tunneling

Fowler-Nordheim tunneling (FNT) describes the transmission of electrons confined by a triangular shape barrier (Figure 2.4). With insufficient energy to enter the barrier, the charge carrier can tunnel to the opposite side of the barrier. This becomes a relevant conduction mechanism when the width of the barrier is in the nanometer range. The triangular potential barrier decreases its effective width when the applied electric field increases. [67]

Besides the classic description of tunneling between electrodes, we also observe a Fowler-Nordheim-type tunneling in the tunneling from traps to the conduction band (see Figure A.3 (right)).

This mode of conduction occurs when the voltage across the barrier is large enough, and the potential barrier is deformed into a triangular barrier. The current density becomes [69]

$$J_{FNT}(E) = \frac{q^3 m}{8\pi h m^*} \frac{E^2}{\varphi_B} \exp \left[ -8\pi \frac{\sqrt{2m^*}}{3hq} \frac{\varphi_B^{3/2}}{E} \right] \quad (2.4)$$

where  $\varphi_B$  is the barrier height of the triangular potential shape.

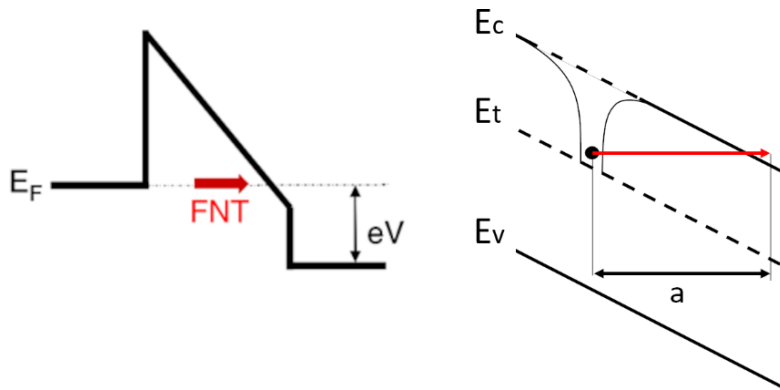


**Figure 2.4** Schematic power band diagram of Fowler-Nordheim (F-N) mechanism. FN tunneling occurs when the applied electric field is large compared to the barrier potential, so that the effective barrier width is reduced. The Bulk-limited analogue is the trap-conduction-band tunneling (right). Adapted from reference [68].

### 2.2.3 Schottky Emission and Poole-Frenkel Emission

Also known as thermionic emission, this mechanism is classically shown in a Schottky barrier configuration of a metal-insulator junction (see Figure 2.5). The Poole-Frenkel effect is the bulk-limited analogue of the contact-limited Schottky effect (see section 2.5.2). In the Poole-Frenkel mechanism, the charge carrier originates from a trap within the material instead of a metal interface [70].

The Schottky emission is commonly expressed as

$$J_S(E, T) = A^{**} T^2 \exp\left[-\frac{1}{k_B T} \left(\varphi - \sqrt{\frac{q^3 E}{4\pi \epsilon_0 \epsilon_r}}\right)\right] \quad (2.5)$$

where  $\varphi$  is the potential barrier,  $A^{**}$  the effective Richardson's constant, and  $\epsilon_r$  the permittivity of the material.

The Poole-Frenkel Emission is commonly written as [67]

$$J(E, T) = q\mu N_c E \exp\left(\frac{-W_a - W_{pf}}{k_B T}\right) \quad (2.6)$$

where  $\mu$  is the electronic drift mobility,  $N_c$  the density of states in the conduction band,  $W_{pf} = \sqrt{\frac{q^3 E}{\pi \epsilon_\infty \epsilon_0}}$  is the Poole-Frenkel lowering for a Coulombic trap potential, and  $W_a$  is the trap activating energy.

A comparison between the Schottky and Poole-Frenkel conduction mechanism is shown in Figure 2.5.

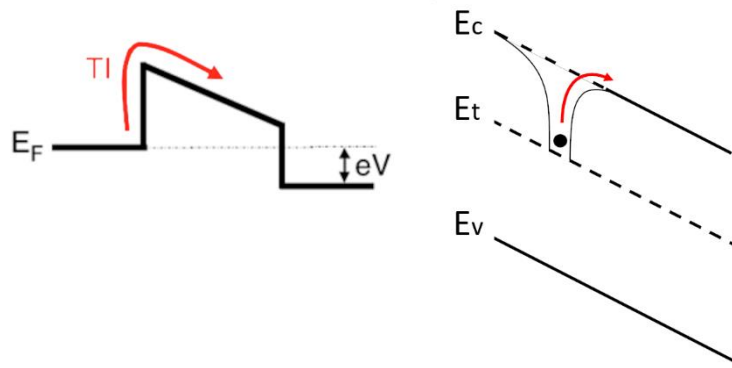


**Figure 2.5** Schematic power band diagrams of Thermionic (Schottky) mechanism. Left: Thermal excitation permits charge carriers to enter the conduction band of the insulator. Right: The thermal excitation of traps is the bulk-limited analogue. This can be described by Poole-Frenkel emission. Figure adapted from reference [68].

## 2.2.4 Gas discharge: Paschen's law

The breakdown voltage  $V_B$  can be described by Paschen's law[71]–[73]. The transition due to changing pressure from class I to class III is shown in Figure 2.14. When pressures decrease with respect to the normal pressure, the breakdown voltage decreases at first due to the small collision distances of ions, preventing them from gaining significant kinetic energy. At even lower pressures, the collision probability becomes too small to form an ionization channel, therefore greatly increasing the breakdown voltage below a critical threshold of around 0.5 mbar over a distance of 1 centimeter. This is described by the equation [74]

$$V_B = \frac{Bpd}{\ln(Apd) - \ln[\ln(1 + \frac{1}{\gamma_{se}})]} \quad (2.7)$$

$\gamma_{se}$  is the secondary electron emission coefficient, A and B are heuristic material parameters. Values of common materials are shown in Table 2.1.

Atmosphere	A	B	$\gamma_{se}$
N <sub>2</sub>	11.8	32.5	0.032
O <sub>2</sub>	6.5	190	0.026
Ar	11.5	176	0.035
He	2.8	77	0.168
H <sub>2</sub>	4.8	136	0.095

**Table 2.1 Parameters of Paschen's law [74]**

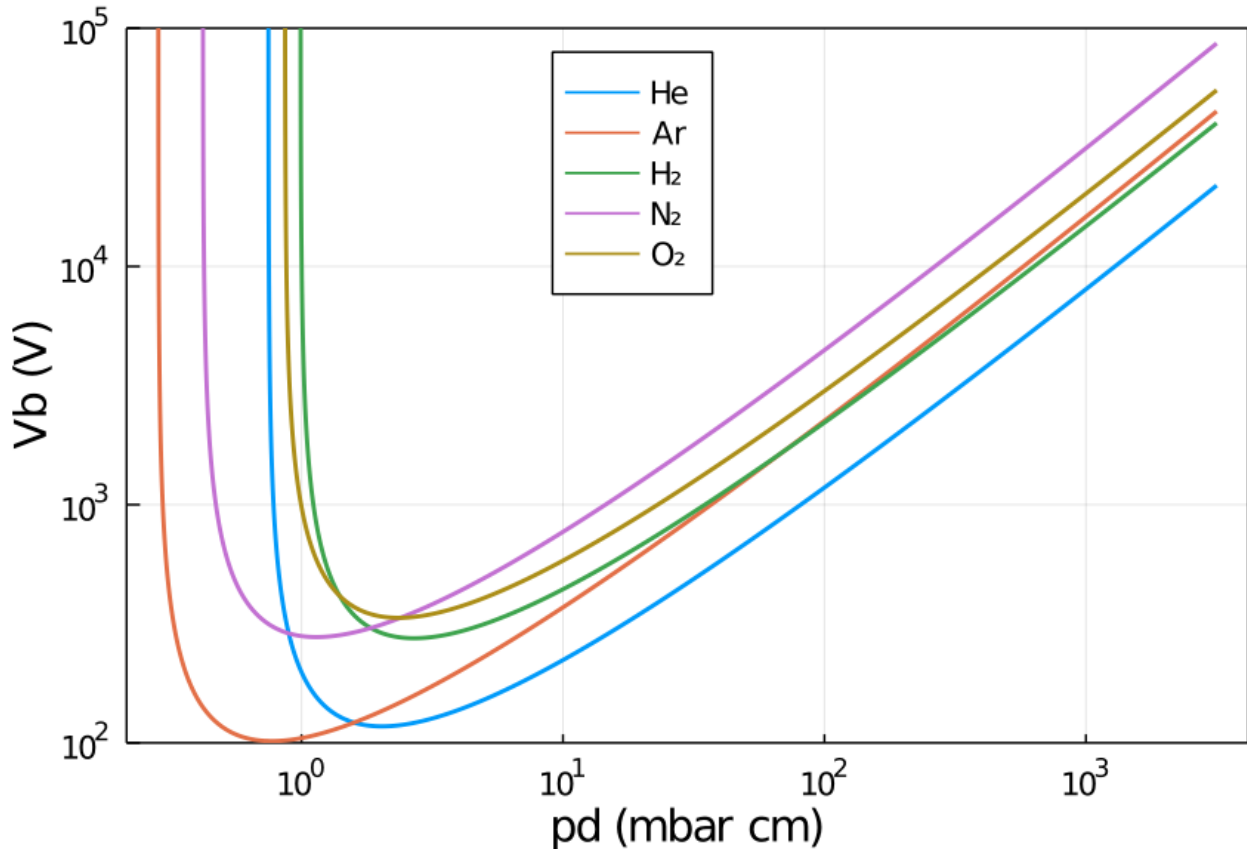


**Figure 2.6** Paschen's law for common gas species. Parameters according to Table 2.1.

## 2.3 Overview of Luminescence phenomena

There exist a large variety of luminescent phenomena. Despite the various terms, they are typically based on related physical mechanisms.

For example, chemiluminescence can result from a variety of chemical processes[75], mechanoluminescence, a result of a mechanical action on a solid[76], radioluminescence

induced by ionizing radiation[77]. Crystalloluminescence is induced by crystallization processes. [78] In electroluminescence, the emission is solely induced by an electric current[79].

Photoluminescence (PL) is a result of absorption of photons that can emit at vastly different timescales, depending on the relaxation mechanism[80], and thermoluminescence, where the re-emission of absorbed energy is activated by heating[81].

Finally, the phenomena of thermally stimulated luminescence and pyroelectric luminescence are investigated in detail in Section 4.

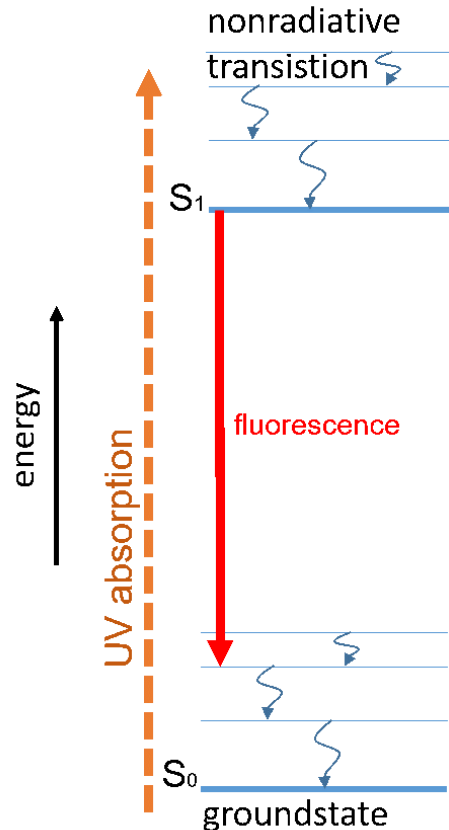


**Figure 2.7** Energy diagram of the fluorescence process. The excited states relax in the nanosecond range[4], meaning that the emission of light stops almost immediately with illumination.

In certain crystals, pyroelectric luminescence can be observed, even after repeated heating and cooling cycles. This is not explained by the classic energy diagram (Figure 2.7). A hypothetical mechanism that could explain this phenomenon is shown in Figure A.1.

### 2.3.1 Thermally stimulated luminescence

Thermally stimulated luminescence is observed in certain materials that have been exposed to a source of radiation of sufficient energy. This process can generate excited metastable states. The luminescence can subsequently be released by heating the material to a characteristic temperature threshold. The temperature functions as a trigger to release the metastable states.

Since these metastable traps are often the result of defects, thermoluminescence is a highly sensitive method to study these [54]. At about 450 K, any material emits significant amounts of infrared black body radiation that becomes a limiting factor in the detection of the thermoluminescence signal.

A wide variety of material types can exhibit TSL, such as glasses, ceramics, semiconductors plastics and other organic solids. By far insulating solids doped with suitable chemical impurities, termed as activator, are the most sensitive TL materials [3, 4,6]. To occupy these trapped states, exposure to radiation must precede the release of these states, which is done by heating [82]. This simple model of excitation, trapping, release and recombination is shown in Figure 2.8. We would like to emphasize that the detrapping alone does not automatically cause emission. A second step of an emitting recombination transition is required.

According to this model, since the traps are depleted after heating, a TL material cannot emit light again when cooling and reheating without repeated illumination [54]. However, as we show in section 4, this model is not always sufficient, and a second emission can be observed.

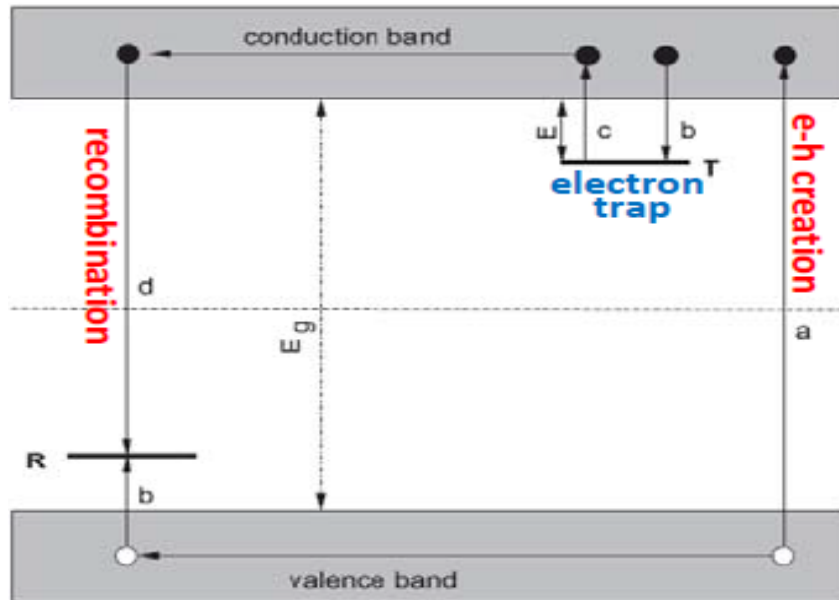


**Figure 2.8** Band diagram of thermally stimulated luminescence. a: electron-hole generation by absorption of a photon, b: capturing of the electron inside a trap, c: release from the trap  $T$  by thermal excitation over the trap depth  $E$ , d: recombination in a recombination center  $R$  with the hole by emission of light [54].

The band diagram (Figure 2.8) shows the energy transitions when electrons and holes are generated by UV irradiation. Defect-induced localized energy levels within the band gap can trap these electrons and holes. Upon thermal excitation or high electric fields, these trapped charge carriers can escape. At this point, they can recombine or become trapped again. The location of recombination is called recombination center, also called luminescence center in case of radiative recombination.

The graph of intensity of luminescence over temperature is called thermoluminescence glow curve (see Figure 2.10). Depending on the trap energies within the material, one or more peaks can be visible. The peak position, shape and intensity is a fingerprint of the specific material and its impurities and defects. [54]

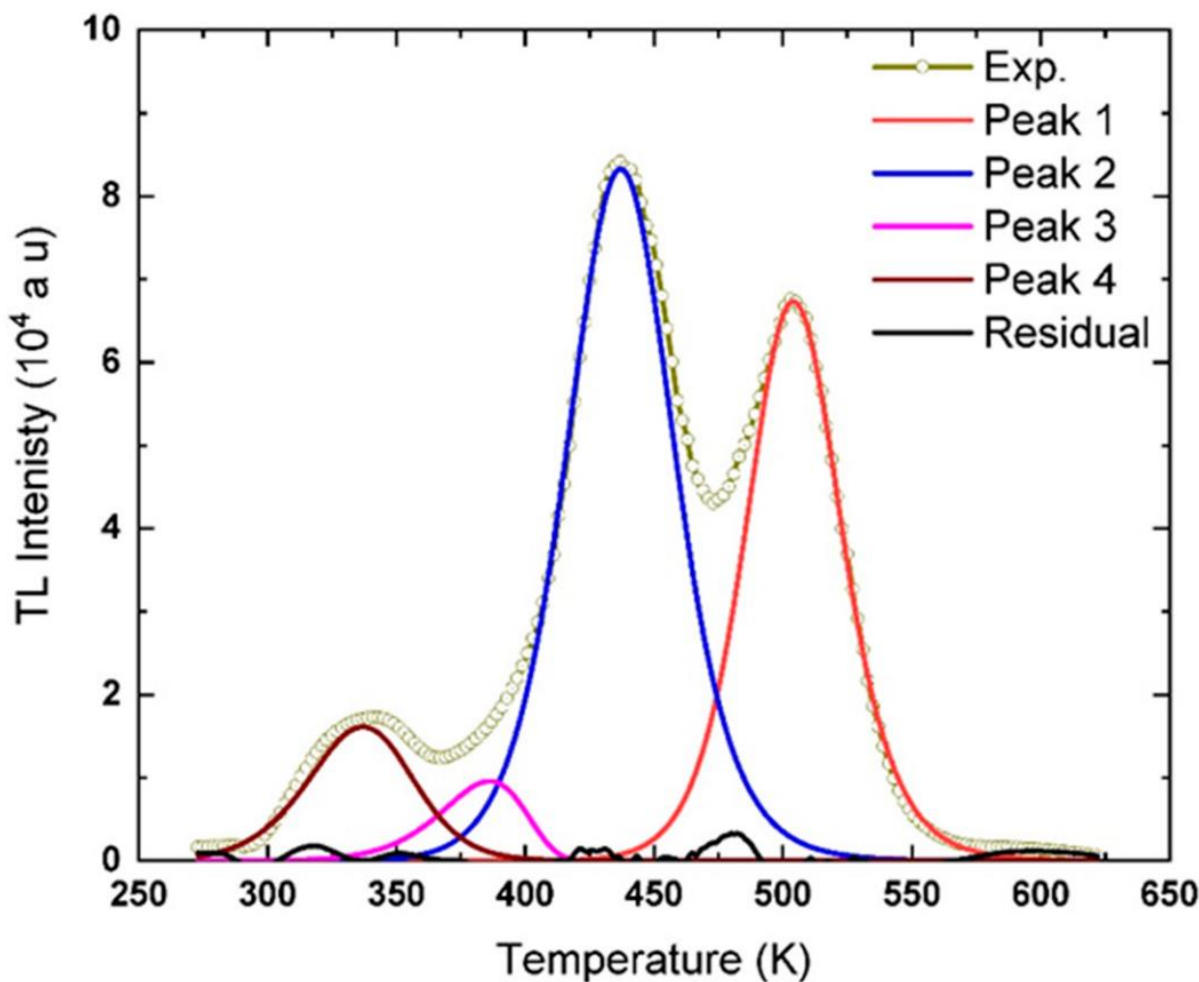


**Figure 2.9** Thermoluminescence glow curve of doped  $\text{La}_2\text{O}_3$ , including peak fits [83]

Depending on the shape of the luminescence curve, it is possible to determine if the emission is caused by a first- second or mixed (general) order process. The first order process assumes no significant regeneration of traps during the emission.

Thermally stimulated luminescence (TSL) is used to determine the fundamental properties of localized electronic states in insulators and semiconductors. [84] TSL can be seen as an initial photoexcitation and metastable trapping of charge carriers with

subsequent thermal activation of defects in the dark. TSL peak gives information about the trap depth and the density of traps[84]. This relationship can to a first approximation be described by the Arrhenius law.

### 2.3.2 Pyroelectric luminescence

In pyroelectric luminescence, the change in temperature of a pyroelectric material leads to emission of light. The nature of PEL is different from that of thermoluminescence. PEL is a spontaneous light emission process that occurs with a change of temperature, also upon cooling and it is accompanied by a change in spontaneous polarization and subsequent creation of a pyroelectric field. All ferroelectrics show a change of polarization under changing temperature as shown in Figure 2.10.

PEL was first discussed by Patel and Hanson in (1981)[43] It is comprised of three types of phenomena. Type 1 and 2 are spike-like discharges and have been quantitatively described by Kalinowski and Dreger (1987)[42] .Type 3 is continuous luminescence that slowly varies according to temperature and time [43][39].The different types of PEL are based on the dependence of the ambient pressure[39]. This pressure dependence is comparable for all the crystals and can be divided into three different mechanisms[44] as shown in Figure 1.11 and Figure 1.12.

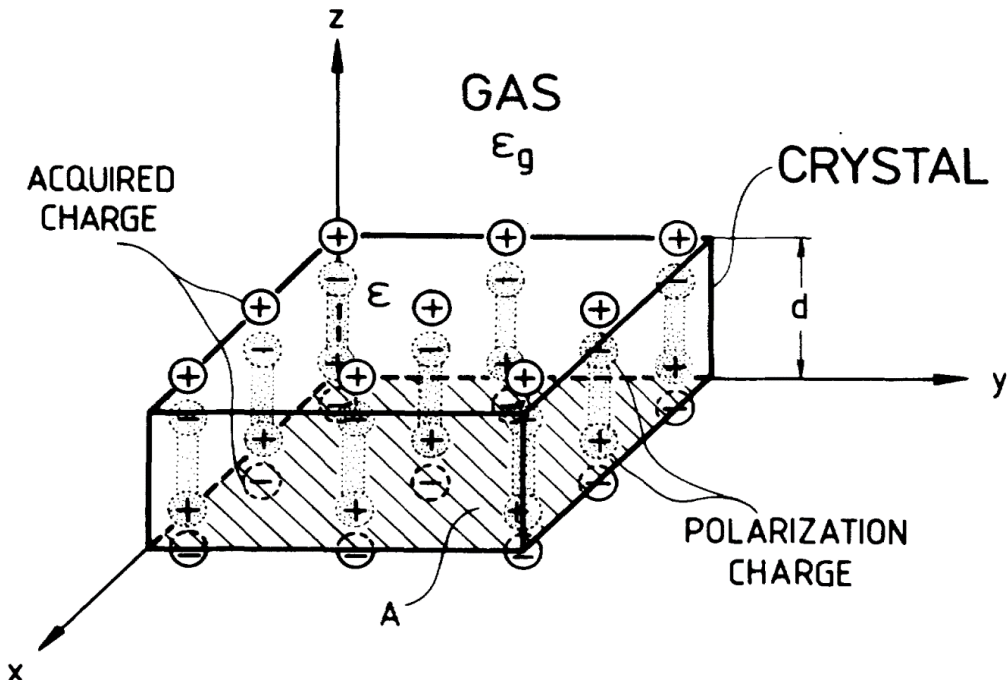


**Figure 2.10** Polarization and agglomeration of surface charges shielding this polarization[42]

The change of polarization in a pyroelectric under changing temperature is given by[42] (see also Section 1.2.2):

$$\frac{dP_s}{dT} = \gamma_p \quad (2.8)$$

In case of no electric conduction with initial polarization zero, we obtain the change in polarization

$$\Delta P_s = P_s(T) - P_s(T_0) = \int_{T_0}^T \gamma_p dT = \int_{t_0}^t \gamma_p \beta dt \quad (2.9)$$

$P_s$  is the spontaneous polarization of the pyroelectric,  $\beta$  is the heating rate  $\frac{dT}{dt}$ ,  $\Delta T$  is temperature change with time, and  $\gamma_p$  is the pyroelectric coefficient. The polarization of a pyroelectric material is accompanied by the electric field growing along the pyroelectric axis of a crystal and can be seen as:

$$\Delta E = \frac{\Delta P_s}{\chi \epsilon_0} = \frac{\gamma_p \Delta T}{\chi \epsilon_0} \quad (2.10)$$

where  $\chi = \epsilon_r - 1$  is the electric susceptibility at low frequency (at the time scale of seconds) and  $\epsilon_0$  is permittivity of free space. From equation (2.10), strictly valid for insulator only, the resulting electric field is correlated with temperature variation by equation

$$\Delta E = \frac{\gamma_p \beta \Delta t}{\chi \epsilon_0} \quad (2.11)$$

If  $\gamma_p, \chi$  are independent on temperature than equation (2.11) becomes:

$$\frac{dE}{dt} = \frac{\gamma_p(T)\beta}{\chi(T)\epsilon_0} \quad (2.12)$$

Equation (2.12) describes the electric field as a function of polarization and temperature with time. When the pyroelectric is not an insulator equation (2.12) has to be rewritten to compensate for leakage as equation:

$$\frac{dE}{dt} = \frac{\gamma_p\beta}{\chi(T)\epsilon_0} - \frac{\sigma E}{\epsilon_r(T)\epsilon_0} \quad (2.13)$$

where the term  $\sigma E$  is leakage current and depends on electric conductivity  $\sigma$  and  $\chi = (\epsilon_r - 1)$ ,  $\chi \approx \epsilon_r$  when  $\epsilon_r$  is large. The differential equation is then solved to

$$E(t) = \frac{\gamma_p\beta}{\sigma} \left( 1 - \exp \left( -\frac{\sigma}{\epsilon_r\epsilon_0} t \right) \right) \quad (2.14)$$

Using this approximation, the maximum electric field is  $E_{\max} = \gamma_p\beta/\sigma$ .

Validity of the approximation:

Equation (2.14) provides an explicit expression for the macroscopic electric field caused by the pyroelectric effect in the presence of leakage currents as a function of time. It is however important to notice that this explicit solution only holds true under the assumption that none of the experimental or material parameters is temperature-dependent, which is

a very crude approximation. So, in principle, Eq. (2.14) is only valid over a small temperature range over which the respective parameters  $\beta$ , the heating- (or cooling-) rate,  $\gamma_P$ , the pyroelectric coefficient,  $\sigma$ , the electric conductivity, and  $\epsilon_r$ , the dielectric permittivity can be considered constant. This immediately raises the question over, which temperature range the approximation holds true, which I shall discuss now:

The rate of temperature change  $\beta$  is subject to the control of the experimental conditions. Temperature changes are achieved via a balance of heating through an electric resistor in thermal contact with the sample holder.

### 2.3.3 Optical excitation of a bulk crystal

There exist three basic pathways to produce excited states within a crystal using UV light. First, if the photon energy is large enough, the valence band electrons can be directly excited into the conduction band. Second, if this is not the case, a trap can act as intermediary energy level between the absorption of two photons. Third, two photons can be absorbed virtually at the same time in case of very high intensities, as typically found in lasers. For our experiments, only the first two options are considered.

When the optical energy approaches the band gap, the absorption coefficient of an insulator becomes very large. In other words, the material becomes opaque and only the surface is exposed to the UV light. This volumetric absorption can be quantified by Lambert Beer's Law [85]

$$T = \exp(-\lambda d)$$

where  $T$  is the transmission,  $\lambda$  is the absorption coefficient, and  $d$  is the transmission distance. We see that the optical intensity drops to  $1/e$  at a depth of  $1/\lambda$ . From this, we can see that once we cross the band gap, no excitation within the bulk crystal is possible. If we however remain below these energies, it may be possible to generate trapped states in the crystal homogeneously by using a two-step process using an intermediary trap state as described above. The absorption coefficients  $\lambda$  for our crystals can be seen in Figure 3.4, Figure 3.8 and Figure 3.11, respectively.

Although light of sufficient energy cannot penetrate deeply into the bulk crystal, the electrons that are excited into the conduction band may diffuse significantly deeper into the crystal until they become trapped. For this reason, it may take a significant amount of time to create a homogeneously excited crystal sample. On the other hand, since the emission energy is below the band gap, it can radiate from the crystal, even from deeper locations.

### 2.3.4 Polaron and trapped charges

In insulators and semiconductors, there is no requirement of defects or dopants to create permanent traps. Poole-Frenkel behaviors typically have their origin in small polaron hopping [86]. Polarons are quasiparticles that result from interactions between an impurity and nearby atoms in the crystal lattice. This impurity can be an electron, as shown in Figure 2.11. The net effect of the combined impurity and lattice response gives rise to the polaron pseudoparticle, which has an effective mass different from that of the isolated impurity.

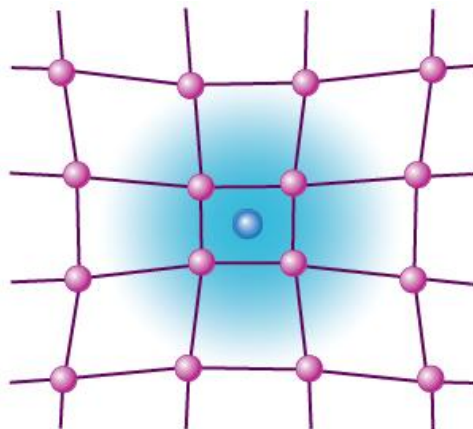


**Figure 2.11** Polaron generated by a self-trapped electron within the crystal. The positively charged lattice ions (purple) are attracted to the electron (blue), generating a potential well [87]

There exist several types of polarons:

**Small bound polaron.** In positively charged defects, such as those induced by congruent crystallization, electrons can be trapped at this location, locally distorting the crystal. The electron is bound to that site [88].

**Small free polaron.** Electrons can also be self-trapped at sites of charged ions and form another type of polaron, a so-called "small free polaron". Both the stability of bound and small free polarons can be highly temperature dependent. The typical lifetime of small polarons is in the microsecond range in strongly reduced crystals [89].

**Bound bipolaron.** Another possibility is that polarons of opposite charge bind two electrons forming a bound bipolaron. These bound bipolarons can be stable at room temperature and can be dissociated thermally or optically by absorbing light [90].

**Small bound hole polaron.** In the case of illumination with high photon energy such as ultraviolet or X-ray irradiation, direct excitation of an electron from the valence band (VB) to the conduction band (CB) is possible which leaves a hole in the VB [91].

Due to the local deformation of the lattice that propagates alongside the charge carriers, the effective permittivity can be significantly enhanced. The movement of polarons in an electric field can constitute a significant electric current.

Polarons play a vital role in the understanding of pyroelectric luminescence. The process is schematically shown in Figure 2.12, using the example of LiNbO<sub>3</sub>. Using a high energy light source, a concentration of electron-hole-pairs are created. These can either remain bound as a self-trapped exciton (STE), or dissociate with the electron forming a small free polaron and move though the lattice by thermal activation [92], [93], which can subsequently recombine with the trapped holes, forming STEs again, or annihilate with the hole (see Figure 2.12). The material, temperature and doping may affect the ratio between the generated bound STEs and free polarons. Besides the free polaron recombination, STEs can also have significant mobility. These may get pinned on defects, similarly to the formation and trapping of single-site small polarons. STEs may also have significant mobility that allows them to radiatively recombine at defects. [89]

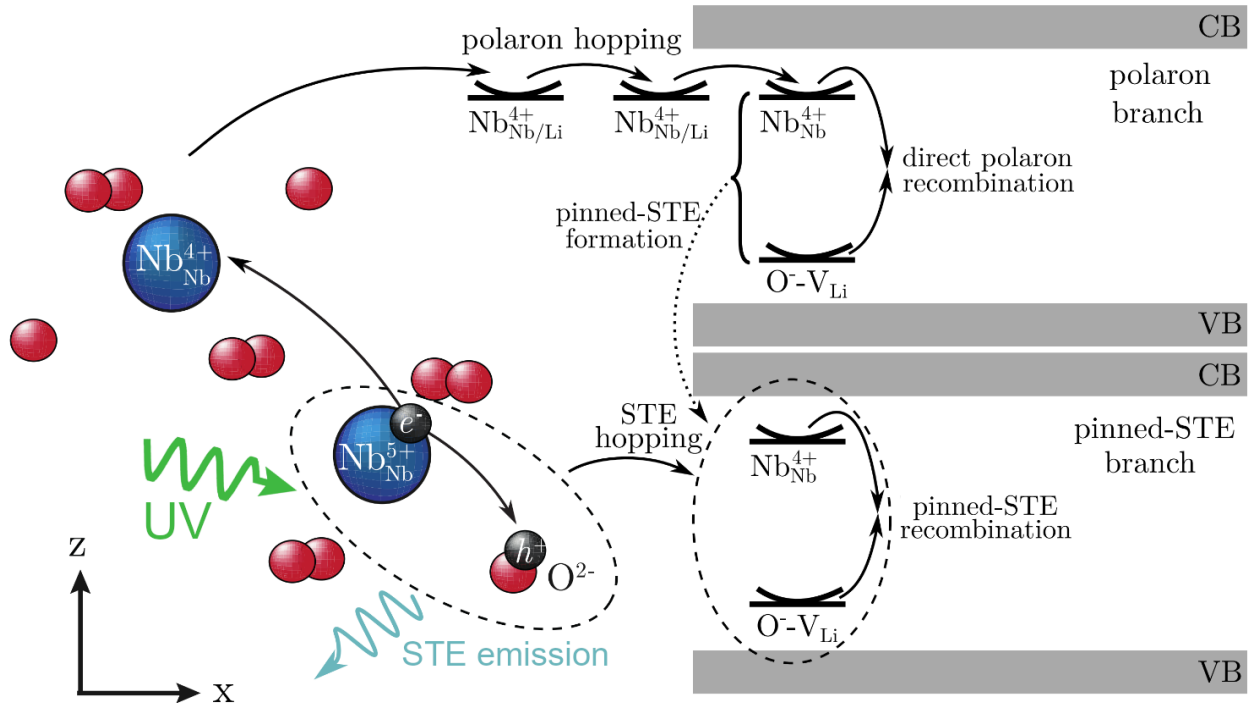


**Figure 2.12** Polaron excitation and recombination. The excitation can be achieved by UV light of sufficient energy. Part of the generated electron-hole pairs recombine directly, while the remainder can (1) form STEs at the  $\text{NbO}_6$  site, (2) Dissociate into separate positively and negatively charged small polarons. The recombination paths are divided into a polaron and an exciton branch. Adapted from [94]

## 2.4 Models of Thermoluminescence

### 2.4.1 Arrhenius Law

The Arrhenius Law is the simplest description of a thermally activated exponential process. It results directly from the assumption that the rate of change of a quantity is proportional to its current amount, the ratio of thermal activating energy  $k_B T$  and energy

barrier  $W_a$ . (see Appendix A.2). From this simple statement, the model in the context of TL describes the thermally activated release of trapped charge carriers [54]

$$\frac{N(T)}{N_0} = c e^{\left(\frac{-W_a}{k_B T}\right)} \quad (2.15)$$

where  $\frac{N(T)}{N_0}$  is the probability that a trapped charge carrier is thermally released.  $W_a$  is the activation energy to release an electron from the trap,  $k_B$  is the Boltzmann constant ( $8.617 \times 10^{-5}$  eV. K $^{-1}$ ) and  $T$  is the absolute temperature, and  $c$  is a proportionality constant. The intensity of luminescence is proportional to the number of occupied traps [55]

$$I(T) \propto N(T) \quad (2.16)$$

The exponential relationship holds true as long as the change in occupied trapped states is small. For this reason, the Arrhenius law is valid only on the onset of emission, where the initial slope of a y-logarithmic plot be used to determine the trap depth  $W_a$  [55]. However, the process of trap depletion that reduces the emission cannot be represented in this way.

Using the Arrhenius model, we can extract the TSL activation energy. The activating energy can directly be visualized by graphing the data in an Arrhenius plot. The slope of the linear fit at the onset of emission is a direct measure of the activating energy. Since the Arrhenius model assumes a constant, non-replenishing initial number of occupied traps  $N_0$ , the model is limited to describing the onset of the emission peak.

Thus, the Arrhenius law to describes the onset of the intensity peak is

$$I(T) = cN_0 \exp\left(-\frac{W_a}{k_B T}\right) \quad (2.17)$$

where  $N_0$  is the number of trapped states, and  $c$  is a proportionality constant that describes the likelihood of one released trap to be detected as photon in the PMT. Reformulating this equation to a linear expression yields

$$\underbrace{\log(I(T))}_{y \text{ axis}} = \underbrace{\log(cN_0)}_{y \text{ intersect}} - \underbrace{\left(\frac{W_a}{k_B}\right)}_{\text{slope}} \underbrace{\left(\frac{1}{T}\right)}_{x \text{ axis}} \quad (2.18)$$

As indicated in the equation, the measured quantities  $\frac{1}{T}$ ,  $\log(I(T))$  can easily be graphed in a Cartesian plot to obtain a linear progression with y-intercept  $\log(cN_0)$  and the slope quantifying the activating energy  $\frac{W_a}{k_B}$ .

### 2.4.2 First order kinetic glow peaks

The first order glow peak assumes that no significant regeneration (refilling) of traps takes place during the emission process. The first order model from Bos et al. 2003 [95] to describe thermoluminescence peaks is

$$I(T) = I_m \exp\left(\frac{W_a}{kT_m} - \frac{W_a}{kT}\right) \exp\left[\frac{W_a}{kT_m} \alpha\left(\frac{W_a}{kT_m}\right) - \frac{T}{T_m} \alpha\left(\frac{W_a}{kT}\right) \exp\left(\frac{W_a}{kT_m} - \frac{W_a}{kT}\right)\right] \quad (2.19)$$

where  $W_a$  is the activating energy, and  $T_m$  is the temperature of peak emission, and  $\alpha$  is an approximation of the exponential integral expression  $x \exp(x) Ei(x)$ , given by

$$\alpha(x) = \frac{a_0 + a_1x + a_2x^2 + a_3x^3 + x^4}{b_0 + b_1x + b_2x^2 + b_3x^3 + x^4} \quad (2.20)$$

With the parameters  $a_0 = 0.267773734$ ,  $a_1 = 8.6347608925$ ,  $a_2 = 8.05901697$ ,  $a_3 = 8.5733287401$ ,  $b_0 = 3.9584969228$ ,  $b_1 = 21.0996530827$ ,  $b_2 = 25.6329561486$ ,  $b_3 = 9.5733223454$  [95].

The *tgcd* software package for the R statistical computing language implements this model and is used to fit subsequent luminescence curves [96], [97].

## 2.5 Conduction in Pyroelectric Crystals

The field assisted mechanisms rely on the modification of the barrier to transport charge.

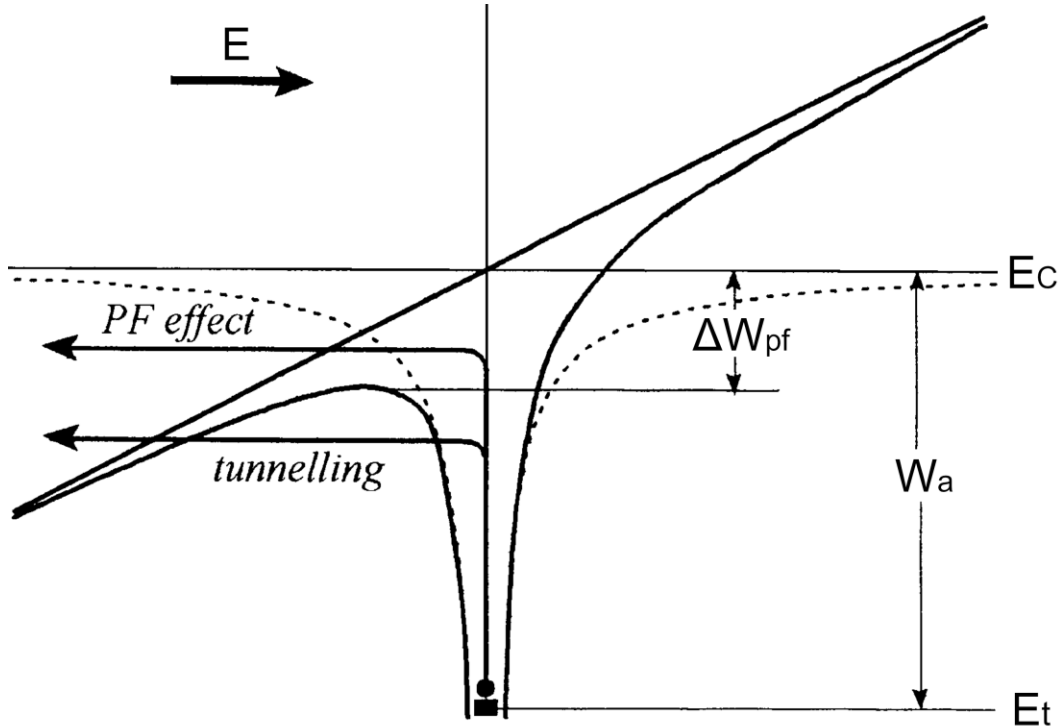


**Figure 2.13** Poole-Frenkel barriers as a function of electric field. A positively charged trap potential (dashed line) is deformed in the presence of a macroscopic electric field. This lowers its activating energy by  $\Delta E_c$  (solid line). Electrons can be emitted by elevation over the , tunneling through the barrier or by a combination of both [98].

### 2.5.1 Pyroelectric Crystal Discharge Mechanism

The transition due to reduced discharges through the surrounding atmosphere with decreasing pressure from class I to class III is shown in Figure 2.14.

In our study of pyroelectric crystals, the sparks of pyroelectric luminescence (PEL) can mostly be suppressed, and we observe a new continuous emission (Type 3) at heating and cooling[41]. The process is associated with the detrapping of charge carriers in defect

states that requires a higher electric field than Type 1 or Type 2 described in the following sections.

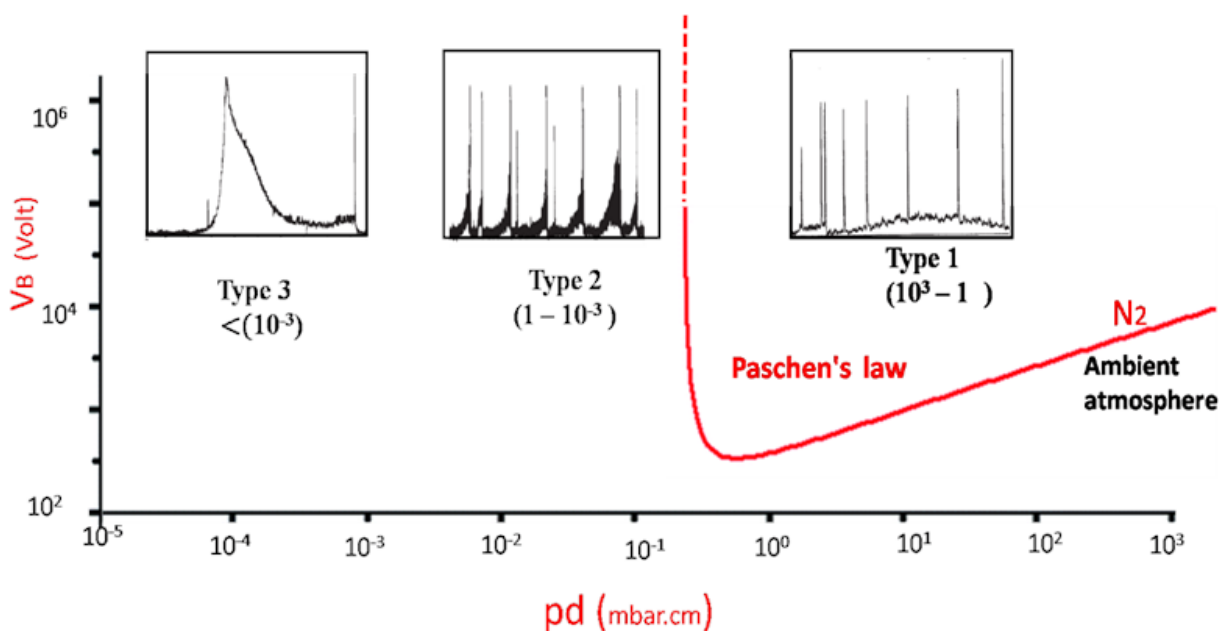


**Figure 2.14** Change of the breakdown voltages in ambient gas, depending on the pressure. Adapted from[43].

### 2.5.2 Poole-Frenkel emission

The pyroelectric emission is investigated in terms of Poole-Frenkel effect to describe the mechanism of SPEL under the high vacuum. A high pyroelectric field reduces the activation energy barriers shown in Figure 2.13, which allows for luminescence through radiative charge carrier recombination through the Poole Frenkel effect[99]

$$I(t, T) = \frac{\partial}{\partial t} N(t) = N(t) e^{-\left(\frac{W_a - W_{pf}}{k_B T}\right)} \quad (2.21)$$

Here,  $W_a$  is the activation energy required for the charge carrier to elevate to the conduction band without electric field.  $W_{pf}$  is the reduction due to the electric field.

The emission of multiple, independent emitting traps is

$$I(t, T) = \sum_{i=1}^N I_i(t, T) \quad (2.22)$$

with  $N$  emitting traps of different activating energies  $W_{a,i}$  and Poole-Frenkel lowering  $W_{pf,i}$ .

### 2.5.3 Coulombic potential

The classical Poole Frenkel mechanism assumes a Coulombic potential shape that is lowered by an external electric field.

Smooth pyroelectric luminescence is associated with the pyroelectric field in high vacuum as a result of temperature change in the crystal. This emission can be described through release of trapped charge carriers and triggered by the pyroelectric field.

From Figure 2.13, the total potential of charge carrier given by equation:

$$W(r) = -Eer - \frac{e^2}{4\pi\epsilon_{\infty}r^2\epsilon_0} \quad (2.23)$$

The radius at the peak barrier potential is the Poole-Frenkel radius. It is found by setting the derivative to zero:

$$\left. \frac{\partial W(r)}{\partial r} \right|_{r=r_0} = 0 \quad (2.24)$$

Which yields the Poole-Frenkel-Radius

$$r_0 = \sqrt{\frac{q}{4\pi\epsilon_{\infty}\epsilon_0 E}} \quad (2.25)$$

Poole-Frenkel potential as follows:

$$W_{PF} = W(r_0) = \sqrt{\frac{q^3 E}{\pi\epsilon_{\infty}\epsilon_0}} \quad (2.26)$$

Where  $E$  is pyroelectric field,  $\varepsilon_\infty$  optical permittivity of the material ( $\varepsilon_\infty = n^2$ ) where  $n$  is the refractive index of material [16],  $\varepsilon_0$  is the vacuum permittivity ( $8.854 \times 10^{-12} \text{ C}^2 \cdot \text{N}^{-1} \cdot \text{m}^{-1}$ ),  $q$  is a unit of electron charge and  $r_0$  is the Poole-Frenkel radius. Thus, the equation (2.26) is written as follows:

$$w_{\text{PF}} = \lambda_{\text{PF}} \sqrt{E} \quad (2.27)$$

Where the Poole-Frenkel coefficient  $W_{\text{PF}}$  proportional to  $\sqrt{E}$  and  $r_0^{-1}$  respectively.

$$\lambda_{\text{PF}} = \sqrt{\frac{q^3}{\pi \varepsilon_\infty \varepsilon_0}}, \quad (2.28)$$

This yields

$$W_{pf} = q \sqrt{\frac{Eq}{\pi \varepsilon_0 \varepsilon_\infty}} \quad (2.29)$$

Where  $E$  is the electric field,  $\varepsilon_\infty$  is the high frequency permittivity.  $q$  and  $\varepsilon_0$  are the electron charge and vacuum permittivity, respectively. The permittivity is typically described by the refractive index.

$$\varepsilon_{\infty} = n^2 \quad (2.3 \\ 0)$$

The equation becomes

$$I(t, T) \propto \exp \left( \frac{-\left( W_a - q \sqrt{\frac{Eq}{\varepsilon_0 \varepsilon_{\infty}}} \right)}{k_B T} \right) \quad (2.3 \\ 1)$$

#### 2.5.4 Dirac potential

If we assume a rectangular potential shape, the potential lowering is proportional to the width of the potential. This yields

$$W_{pf} = qE \sqrt{\frac{\sigma}{\pi}} \quad (2.32)$$

### 2.5.5 Fower-Nordheim Tunneling of trapped charges

Analog to the classical FNT between two electrodes in Section 2.2.2, can also be applied to when the electron is confined in a trap potential (see Figure 2.15). In this case, the electron is expected to have a significantly higher frequency due to the localization. The FNT emission rate is [69]

$$I(t) \propto \frac{E^2}{W_a} \exp\left(-\frac{8\pi\sqrt{2m^*}}{3hq} \frac{W_a^{3/2}}{E}\right) \quad (2.33)$$

where  $m^*$  is the effective mass of the charge carrier.

Smooth pyroelectric luminescence is associated with the pyroelectric field in high vacuum as a result of temperature change in the crystal. This emission can be described through release of trapped charge carriers triggered by a very large pyroelectric field. During the heating and cooling cycles, the rate of change in temperature  $dT/dt$  is sufficient to produce electric fields  $E$  up to  $10^7$ - $10^8$  V/m as a result of the buildup of pyroelectric charge{}, especially at the reduced pressures of  $\sim 10^{-6}$  mbar that prevents charge carrier recombination outside the sample. Such fields, triggered by the pyroelectric discharge, are sufficient to release trapped charge carriers and cause dielectric breakdown and induce luminescence from the crystal itself [43][41]. The electric field enhanced emission takes place through either lowering of the potential barrier (Poole-Frenkel effect) or tunneling of charge carriers across the potential barrier (direct tunneling, Fowler-Nordheim tunneling or phonon-assisted tunneling) [100]–[103]. The lowering of the potential barrier due to the Poole-Frenkel effect results in reducing the ionization energy which in turn enhances the emission rate in the presence of an electric field [55] until either the trap is depleted or the barrier increases again. However, under the influence of high electric fields ( $10^6$ - $10^9$  V/m), charge transport occurs through direct tunneling for very thin barriers ( $d \leq 3$ - $5$  nm), or Fowler-Nordheim tunneling for initially thicker barriers ( $d \geq 10$  nm) [69] or through phonon-assisted tunneling due to the synergistic effect of

temperature and electric field [100][103]. In this study, we consider emission through the Poole-Frenkel effect and Fowler-Nordheim tunneling only.

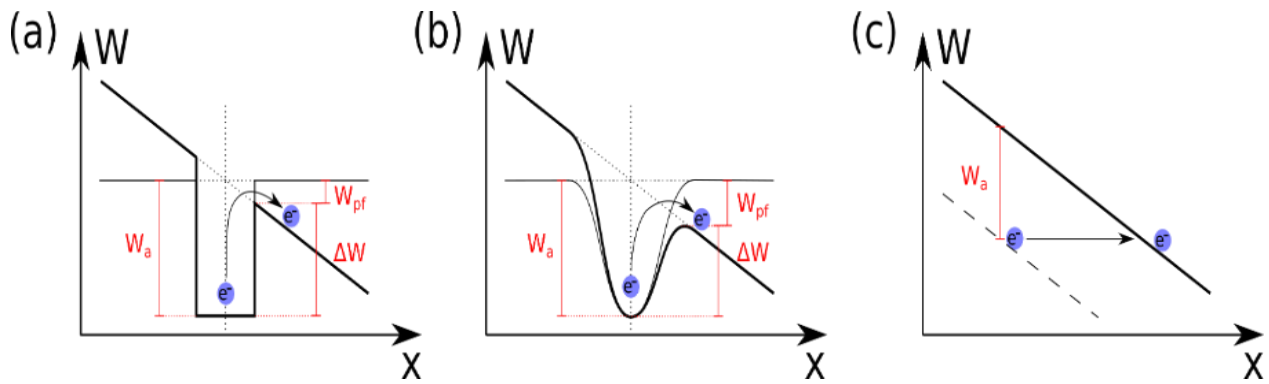


**Figure 2.15** Detrapping mechanisms of electrons: (a) Dirac-well, (b) Coulomb potential, (c) Fowler-Nordheim Tunneling [104]

# Chapter 3

## 3 MATERIALS AND METHODS

### 3.1 Materials

We study  $\text{LiNbO}_3$ ,  $\text{BaB}_2\text{O}_3$  and  $\text{BaTiO}_3$ . All materials have a high technological importance and properties that lends themselves to the study of bulk optical phenomena, such as high transparency. The samples we use are single crystals that are specified as nominally pure. However, all of them are known to contain impurities originating from the crystallization out of the molten phase. Within the temperature range that we study,  $\text{LiNbO}_3$  and  $\text{BaB}_2\text{O}_4$  remain retain a single ferroelectric phase, while  $\text{BaTiO}_3$  exhibits 4 phases with highly nonlinear material properties. The choice of single crystals, as opposed to polycrystalline or powder samples reduces conductivity and thus supports the generation of high electric fields. This is especially true for the highly hygroscopic nanoparticles. Additionally, the electric field in a single crystal is more homogeneous and is experimentally accessible.

#### 3.1.1 Lithium Niobate

Lithium niobate ( $\text{LiNbO}_3$ ) has a trigonal crystal structure (see Figure 3.1) with  $R3c$  space group symmetry (point group  $3m$ ) at room temperature, which makes it piezoelectric and pyroelectric [105][106][107]. Beyond the phase transition temperature ( $T_c \sim 1140^\circ\text{C}$ ), it becomes centrosymmetric with  $R3m$  space group structure [107][108]. This symmetry makes it an uniaxial crystal with the crystallographic  $c$ -axis being the 3-fold rotational symmetric axis [7].

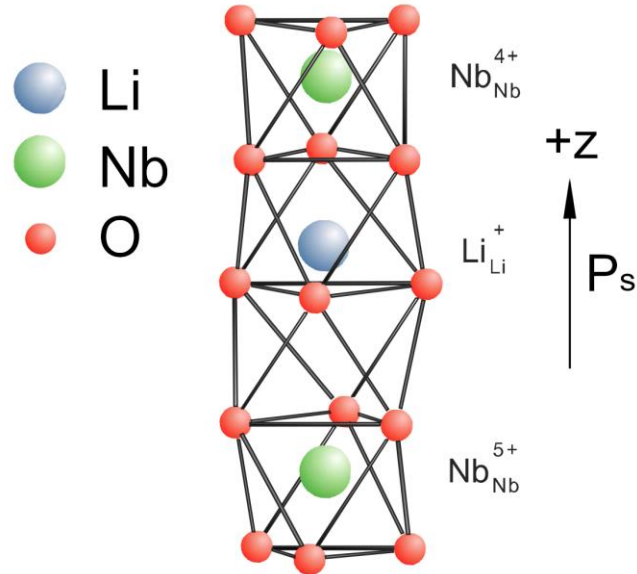


**Figure 3.1** Crystal structure and polarisation [89]

### 3.1.1.1 Defects

Crystal defects are likely the root cause of SPEL, as previous experiments revealed that the energy of emitted photons is substantially lower than the band gap energy of 3.7 eV [109]. Congruent  $\text{LiNbO}_3$  crystals can have intrinsic as well as extrinsic defects which influence the optical and electronic properties. Oxygen vacancies ( $\text{V}_\text{O}$ ) are among the various intrinsic defects [110]. Another type of intrinsic defects are Nb antisite defects where Nb ions occupy Li sites [111][112] along with charge compensators in the form of Li vacancies, vacant Nb sites or  $[\text{Nb}_{\text{Li}}-\text{V}_{\text{Nb}}]$  defect complexes [113]. The loss of oxygen from the surface of  $\text{LiNbO}_3$  crystal may be accompanied by an incorporation of Nb ion onto the empty Li site. The Nb ion acts as a trap for the released excess electrons [114]. Similarly, there can be extrinsic defects in the form of impurities like  $\text{Fe}^{3+}$ ,  $\text{Cu}^{2+}$ ,  $\text{Cr}^{3+}$ ,  $\text{Mg}^{2+}$ ,  $\text{Ni}^{2+}$  among others [115][116][117][58]. There exists a large number of vacant Li and fewer vacant Nb sites in CLN, which can incorporate impurity ions. Interstitial sites are also possible. Although the ionic radii of  $\text{Nb}^{5+}$  and  $\text{Li}^+$  are similar, most impurities prefer empty

Li sites [107]. All these impurities show strong optical absorption bands from the UV up to the near-infrared wavelength range [118]–[120].

From the literature, we find small free polarons require energies between 0.2 eV and 0.3 meV for phonon-assisted hopping transport. The small bound electron polaron at the  $\text{Nb}_{\text{Li}}^{5+}$  has an activating energy of 0.65 eV. [121]

### 3.1.1.2 Band diagram transitions

The optical excitation and relaxation processes are shown in (Figure 3.2). Besides the shown two-photon process, there exists also an excitation over intermediary traps or direct VB-CB excitation for sufficiently small wavelengths. After excitation, the conduction band electron forms a small bound polaron at the niobate site. The recombination from this trap is likely responsible explaining thermo- or pyrostimulated luminescence.

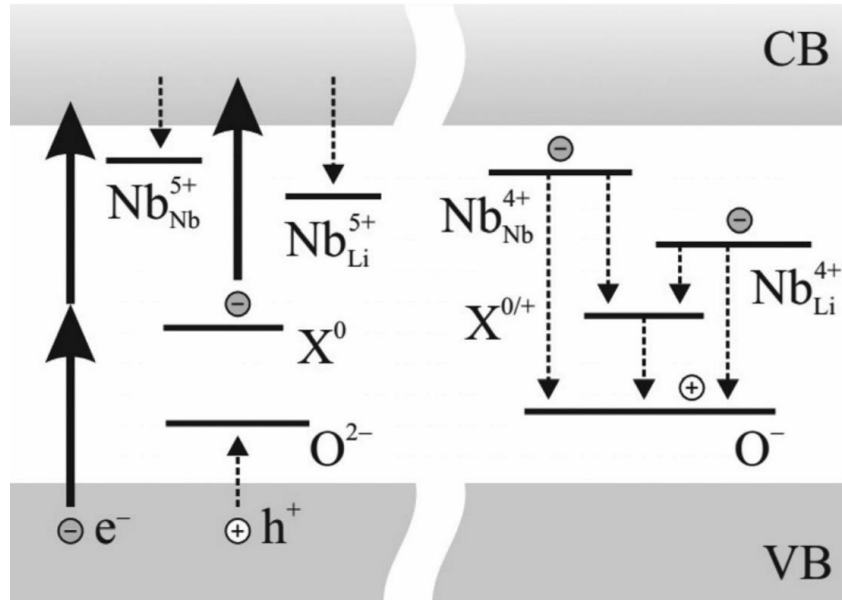


**Figure 3.2**  $\text{LiNbO}_3$  band diagram – polaron excitation and relaxation [121]. Left: Electron-hole pairs are formed by two-photon band-to-band excitation. Carrier localization results in the formation of small free  $\text{Nb}_{\text{Nb}}^{4+}$ , small bound  $\text{Nb}_{\text{Li}}^{5+}$  electron polarons, and small  $O^-$  hole polarons. The two-photon process is observed in lasers, while the excitation from extrinsic defect centers  $X^0$  is the dominant process at low-intensities. Right: Recombination paths are imprinted by electron-hole recombination of free small electron polarons and Bound small electron polarons with hole polarons. The extrinsic  $X^{0/+}$  center may represent an intermediate step.

### 3.1.1.3 Crystal growth and stoichiometry

There are several  $\text{LiNbO}_3$  growth techniques, e.g. Bridgman, Verneuil, flux methods, etc., but the most widely used industrial growth method is the Czochralski growth method [122].  $\text{LiNbO}_3$  is manufactured in the Czochralski process from a melt of  $\text{Li}_2\text{CO}_3$  and  $\text{Nb}_2\text{O}_5$ . The crystallographic axis is determined by the seed crystal. The melt fraction converted into crystal materials of high homogeneity is typically around 50%. The crystal is grown from a congruent melt if the corresponding oxide concentrations are  $c\text{Li}_2\text{O}/(c\text{Li}_2\text{O} + c\text{Nb}_2\text{O}_5) = 48.34 \text{ mol\%}$  and  $c\text{Nb}_2\text{O}_5/(c\text{Li}_2\text{O} + c\text{Nb}_2\text{O}_5) = 51.66 \text{ mol\%}$  [122]. Stoichiometric  $\text{LiNbO}_3$  crystals (SLN), are complicated to grow because they melt incongruently. Although the non-stoichiometry implies a high density of intrinsic crystal

defects, commercial CLN crystals for high-end optical applications are in general non-stoichiometric [123].

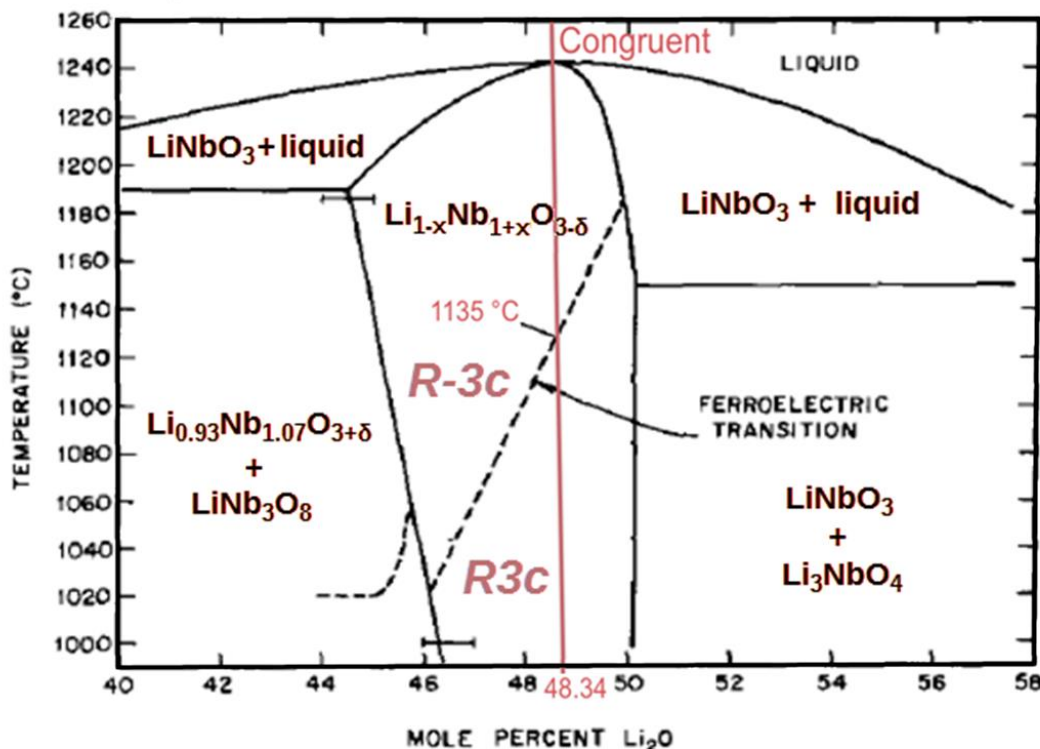


**Figure 3.3** Phase diagram of  $\text{Li}_2\text{O}-\text{Nb}_2\text{O}_5$  near the stoichiometric composition of  $\text{LiNbO}_3$ . The variable  $x$  denotes the ratio  $c\text{Li}/(c\text{Li}+c\text{Nb})$  where  $c\text{Li}$  is the concentration of Li ions and  $c\text{Nb}$  is the concentration of Nb ions [124]

### 3.1.1.4 Optical absorption

To achieve optical excitation in a bulk crystal, the penetration depth of the excitation light is an important factor. This can be quantified by the absorption coefficient, which takes a sharp increase near the energy of the band gap (see Figure 3.4).

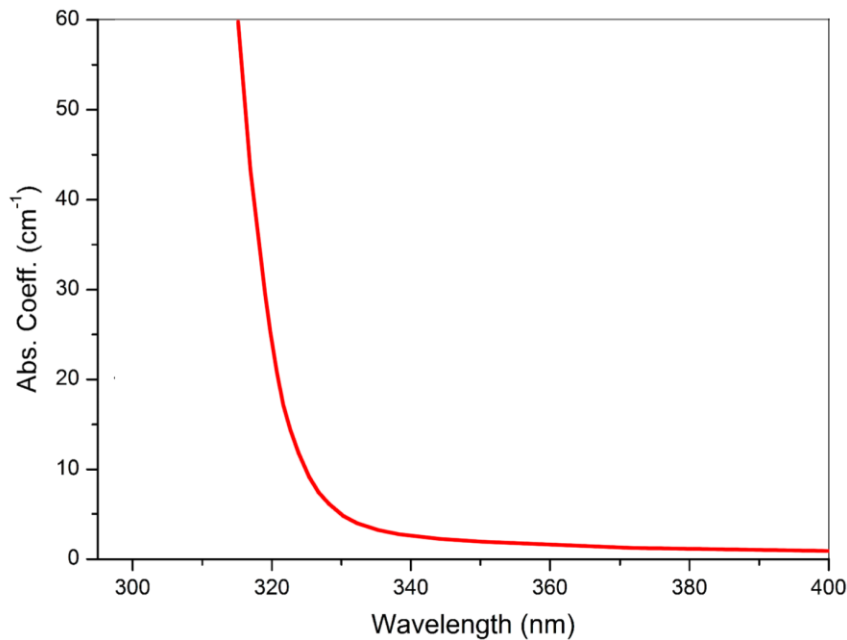


Figure 3.4      Absorption coefficient, LiNbO<sub>3</sub> [125]

## 3.1.2 Barium Metaborate

Barium metaborate ( $\text{BaB}_2\text{O}_4$ ) has two known phases: the quenched high-temperature form ( $\alpha\text{-BaB}_2\text{O}_4$ ) of space group R3c, and the low-temperature phase ( $\beta\text{-BaB}_2\text{O}_4$ ) of the same space group. Because  $\beta\text{-BaB}_2\text{O}_4$  is centrosymmetric, it does not exhibit NLO properties.

### 3.1.2.1 Defects

The most common structural defects in growing BBO crystals by the top seeded solution growth (TSSG) technique are grain boundaries with varying scales of disordered angle orientations and melt inclusions which affect their optical properties. [126] Sodium oxide ( $\text{NaO}_2$ ) is a natural impurity inherited from the flux, which is responsible for the electrical conductivity. [127] Other defects that have been detected by electron paramagnetic resonance in nominally pure bulk crystals include barium vacancies, as well as  $\text{Cu}^{2+}$  and  $\text{Ni}^+$  substitution defects.[128] Besides the permanent structural defects, polarons can create localized, temporary traps within the crystal.

### 3.1.2.2 Band diagram

The activating energies for the electrical leakage current have been determined to be in the range of 1eV to 1.2eV [127] An information about optically induced band excitations is not available in literature.

### 3.1.2.3 Crystal growth

BBO is synthesized at 700 °C and single crystals were grown from the  $\text{BaB}_2\text{O}_4$ –20 m/o  $\text{Na}_2\text{O}$  flux, using the TSSG method and [0 0 1]-oriented seeding crystals.

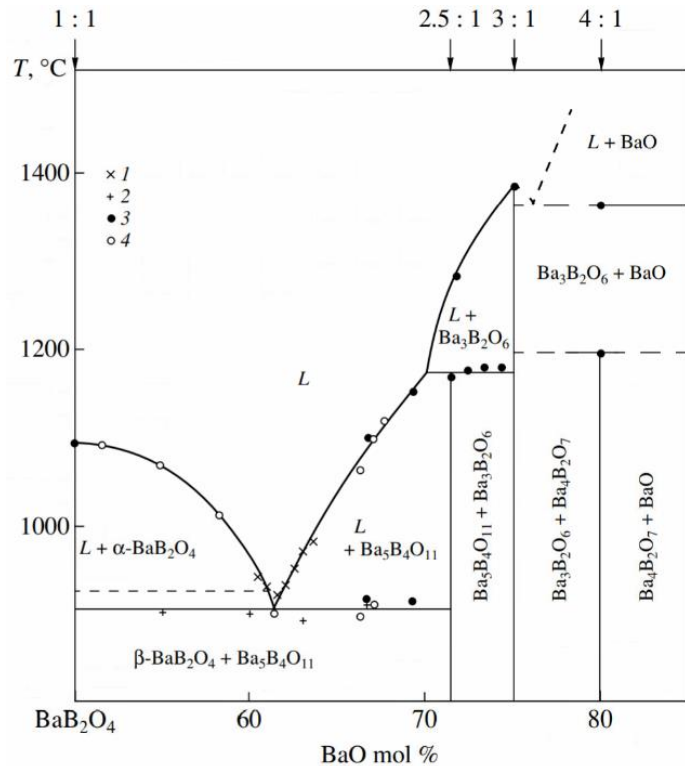


**Figure 3.5**  $\text{BaB}_2\text{O}_4$  phase diagram[129]

The crystal structure of the low-temperature phase is trigonal with unit cell dimensions of  $a/8.380$  and  $a/96.651$  (hexagonal cell:  $a/12.519$  Å,  $c/12.723$  Å),[130] as shown in Fig. 1

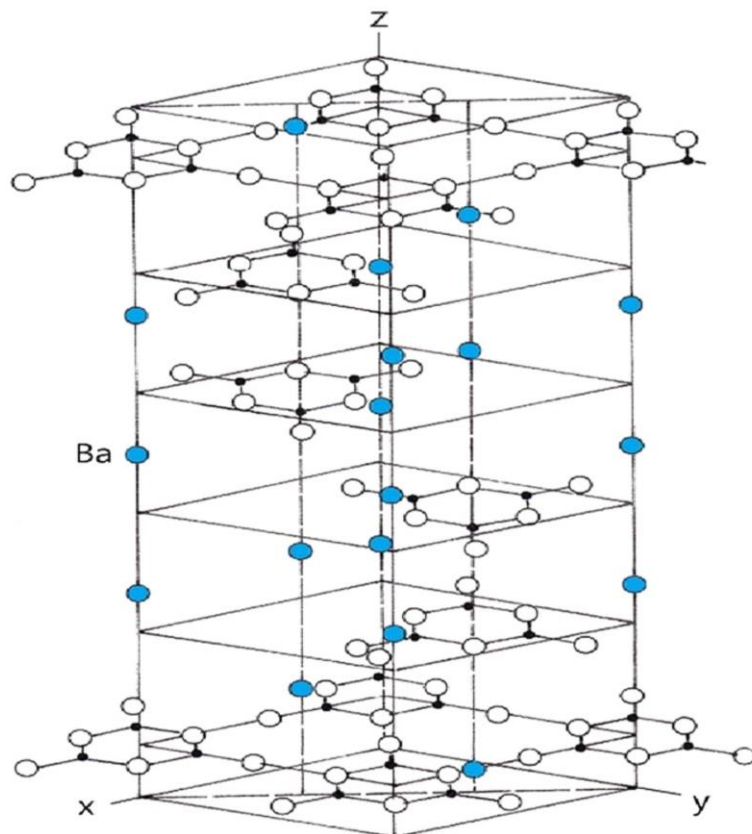


**Figure 3.6      Tetragonal crystal structure of BaTiO<sub>3</sub> [130]**

Near and below room temperature, BaB<sub>2</sub>O<sub>4</sub> occurs in the low-temperature, non-centrosymmetric  $\beta$ -form with R3c space group. It has a band gap of 5.6 eV (215 nm)[131] and the crystals have a fairly high pyroelectric coefficient  $\sim 15 \mu\text{C/m}^2 \text{ K}$  [61], which remains almost constant in the range of 100 –300 K. As a result, temperature changes of the crystal could generate large electric fields,  $E > 10^8 \text{ V/m}$  depending on the rate of change. Under the influence of strong electric fields, charge conduction can occur in semiconductors and insulators due to Schottky emission, Poole-Frenkel effect, direct tunneling, Fowler-Nordheim tunneling, hopping conduction and others. The Poole-Frenkel effect occurs for charged impurities only, whereas direct tunneling in the strong

electric fields is possible for impurities in all charge states [132]. In semiconductors and insulators, defects and impurities introduce localized energy states within the forbidden energy gap which can act as trapping centers for the charge carriers. Deep electron-type traps in the forbidden energy gap are generated while growing  $\beta$ -barium borate crystals by TSSG technique [51]. The activation energy for the electron traps have been calculated in a wide range of 0.03 eV- 1.30 eV through thermal activation methods. Charge conduction could take place due to enhanced emission from trap states under the influence of sufficiently strong electric fields which can lead to potential barrier lowering and reducing the activation energy for charge de-trapping [100], [102].

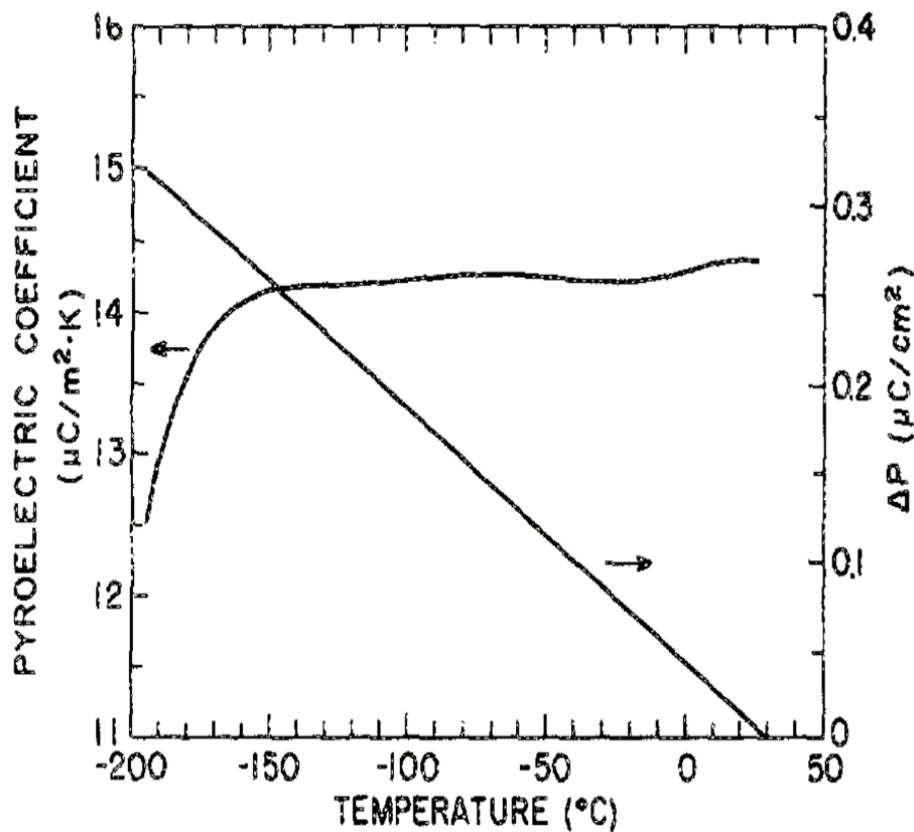
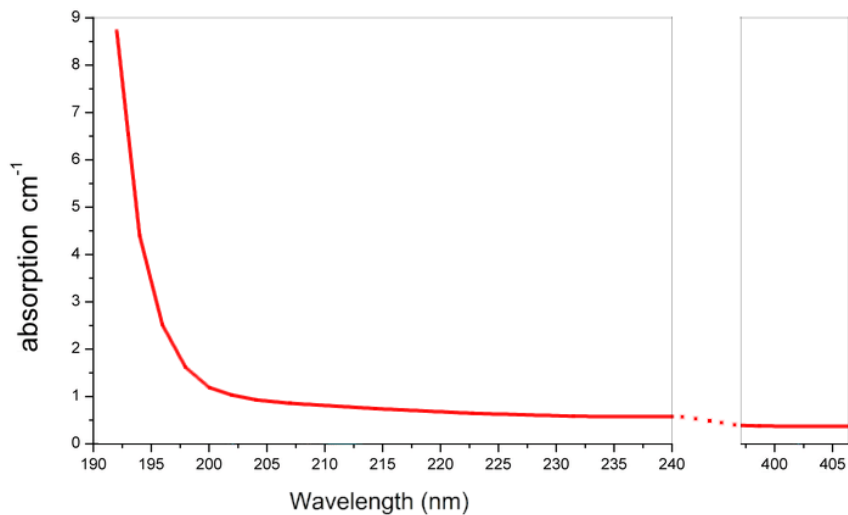


Figure 3.7 Pyroelectric coefficient [61]

### 3.1.2.4 Optical absorption



**Figure 3.8**      **Absorption coefficient,  $\text{BaB}_2\text{O}_4$  [133]**

### 3.1.3 Barium Titanate

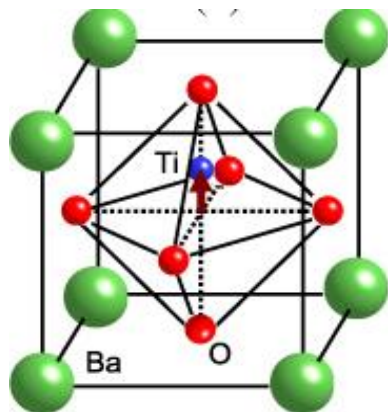


**Figure 3.9 Ferroelectric switching in crystal structure of BaTiO<sub>3</sub> at 278 K [134]**

Barium titanate ( $\text{BaTiO}_3$ ) offers excellent ferroelectric properties with high dielectric constant, low dielectric loss; and its chemical and mechanical stability. It is used in many technological applications, and is one of the most investigated ferroelectric materials due to its ferroelectricity and simple crystallographic structure. The crystal undergoes several phase transitions at different temperatures, making it highly sensitive to temperature and stress [29, 30].

#### 3.1.3.1 Phase transitions

Above the Curie temperature ( $\sim 133^\circ\text{C}$ ) [135], the crystal structure is cubic ( $\text{Pm}3\text{m}$ ) [136]. When cooling through the Curie temperature between  $130^\circ\text{C}$  and  $0^\circ\text{C}$ , the tetragonal structure ( $\text{P}4\text{mm}$ ) is formed [136]. The formation of the tetragonal structure makes the unit cells turn out to be permanently polarized, which leads to spontaneous polarization along the c-axis [27], [137]. Since there are six equivalent  $\langle 100 \rangle$  axes in the cubic phase, upon cooling the polarization can arise parallel to any one of these six equivalent directions. It is the ability to reorient the spontaneous polarization with an external electric field that makes this ferroelectric material so interesting to study. When cooling below  $0^\circ\text{C}$ , the unit cell distorts again and the tetragonal structure changes to orthorhombic structure [138] and below  $-80^\circ\text{C}$ , the rhombohedral phase is formed [134].

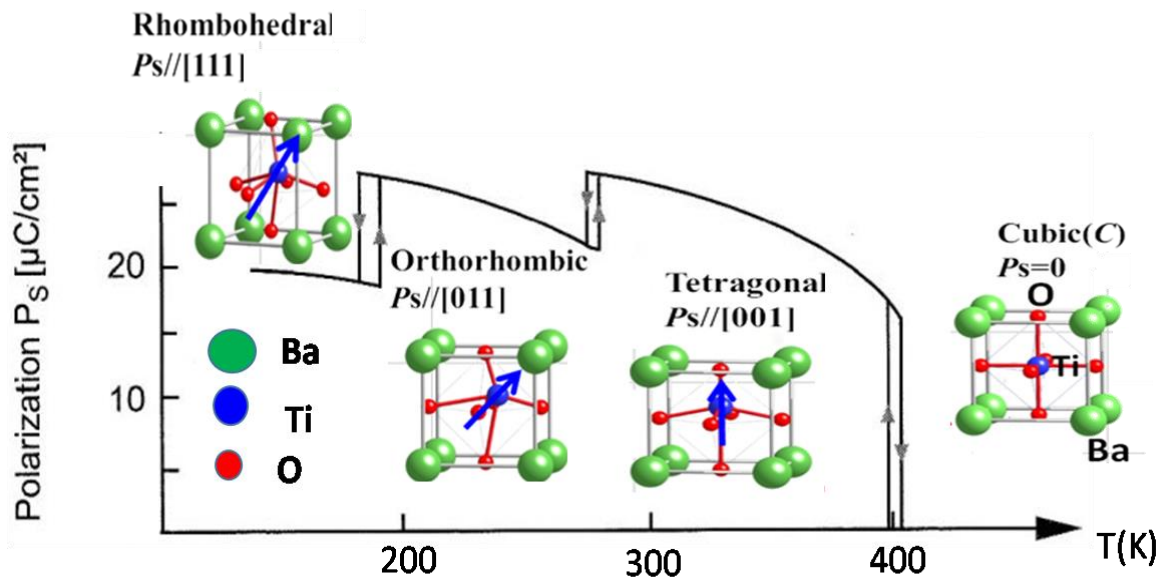


**Figure 3.10**  $\text{BaTiO}_3$  phase transition. Difference Phase transition of  $\text{BaTiO}_3$  with changing temperature (adapted from [134][139]).

### 3.1.3.2 Optical absorption

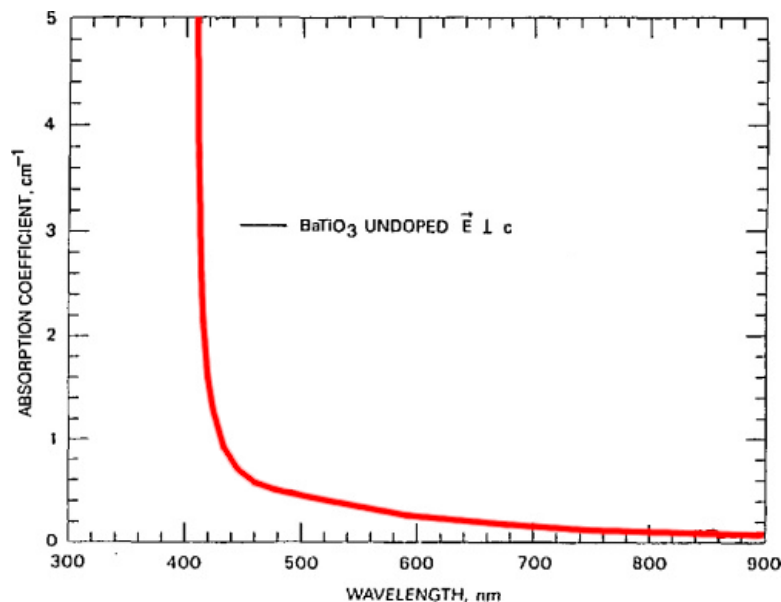


**Figure 3.11** Absorption coefficient,  $\text{BaTiO}_3$  [140] Here the polarization coefficient for unpolarised light is shown. For ordinary and extraordinary polarizations, the curve deviates slightly.

### 3.2 Experimental Setup

Central to our experimental setup is the cryostat, which contains the sample, and allows for accurate temperature control under vacuum conditions. The sample is observable through a 2" diameter glass window, through which the optical emission is observed. The experimental setup is shown in Figure 3.12.

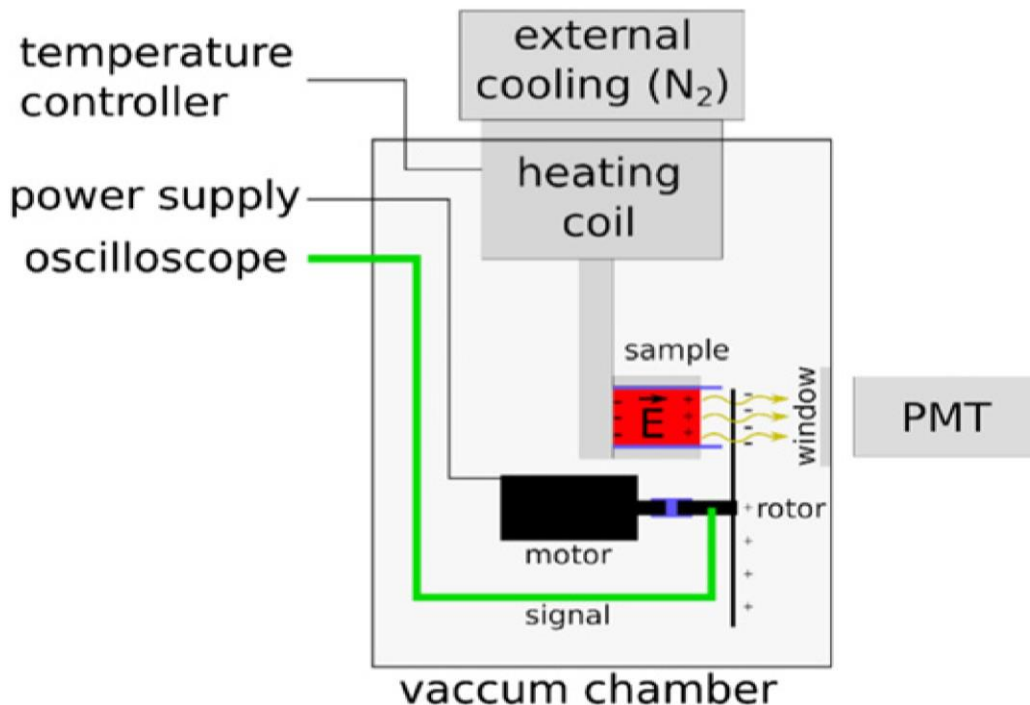


**Figure 3.12** Experimental setup, schematic[52] The sample (red) is attached to the temperature control unit by a thermally conductive sample holder. The horizontal elements of the sample holder are employed to improve the heat transfer to the crystal. To provide electrical insulation, two thin ceramic plates (blue) are employed. A rotor in proximity to the polar crystal surface provides information on the electric field. The luminescence is observed by the PMT though a glass window.

The setup is contained in an opaque enclosure, shielding ambient light from the PMT during the experiment. The essential components and experimental considerations are listed in the following subsections.

### 3.2.1 Sample preparation

The orientation of the crystal polarization axis is chosen perpendicular to the conductive sample holder, in order to avoid electrostatic discharge. The size of the pyroelectric crystal along the polarization axis is an important parameter is indirectly proportional to the electric field that is generated by the changing temperature. However, the crystal should be large enough prevent early discharges.

In order to populate trapped states, charge carriers from the valency band need to be excited. This is attained by illumination using UV light illumination (365 nm). To occupy trapped states within the crystal, this light source should have sufficiently small wavelength to exceed the band gap of the material. However, LiNbO<sub>3</sub> and BaB<sub>2</sub>O<sub>4</sub> have bandgaps above the excitation energy (3.7 eV [141] and 5.6 eV [131]), the optical penetration depth should be sufficiently large to illuminate throughout the bulk of the crystal. For BaTiO<sub>3</sub>, the crystal will likely only experience surface illumination, since the bandgap of 3.2 eV [142] is well below the 3.4 eV of the UV lamp.

Generally, uncoated crystals should be used to avoid optical or electrical interference. Since charge transport can occur over surface contaminants, surfaces must be thoroughly cleaned before each experiment. Each sample is initially heated to 500 K in order to desorb surface humidity.

Sample	Crystal size (xyz)	$\gamma$ ( $\mu\text{C}/\text{m}^2/\text{K}$ )	$E_g$ (eV)
LiNbO <sub>3</sub>	5×10×10 mm <sup>3</sup>	38	3.7 [141]
BaB <sub>2</sub> O <sub>4</sub>	4×4×5 mm <sup>3</sup>	12-15	5.6 [131]
BaTiO <sub>3</sub>	3×3×5 mm <sup>3</sup>	200	3.2 [142]

Table 3.1 Pyroelectric, electronic and geometric sample properties at room temperature. All materials are specified as nominally pure by the manufacturer.

### 3.2.2 Temperature-controlled Cryostat

The cryostat provides an environment of well-defined vacuum and temperature for the experiment (Optistat DN-V2 (Oxford Instruments)). A connected turbomolecular pump provides vacuum down to  $10^{-8}$  mbar. The temperature is controlled by a PID regulated integrated temperature controller (Mercury). Temperature ranges between 77 K and 500 K are archived by a heating element operating in combination with liquid nitrogen cooling. The distance of the temperature controller to the sample means that a small delay between the measured temperature on the sample holder, and actual sample temperature exists.

Constant cooling and heating rates of maxima of -0.25K/s and 0.43K/s respectively were maintained by the PID controller. Three sides of the sample are kept in thermal contact with the heating element to keep internal temperature gradients to a minimum.

### 3.2.3 Heat transfer and time delay within the crystal

There exists a time delay between set temperature and crystal temperature due to the thermal conductivity and size of the sample.

The equation that describes the temperature offset for a one-sided heating is

$$\Delta T = \frac{\beta \rho c_p d^2}{k} \quad (3.1)$$

Where  $\beta$  is the heat rate,  $\rho$  the density,  $c_p$  is the thermal capacity,  $d$  the thickness in direction of heat flow, and  $k$  the thermal conductivity. Since the temperature difference can get prohibitively large due to the size of our crystals, we employ two lateral thermal

contacts over ceramic elements to provide thermal contact from 3 sides (see Figure 3.12). We use the effective thickness of half the distance between the ceramic plates to obtain the temperature difference.

We employ highly insulating ceramics from the top and bottom faces of the sample to provide faster heat exchange. From the equation (3.1), we can see that the temperature difference quadratically increases with the thickness of the sample, which will artificially broaden the peak observed during a heating or cooling cycle by  $\Delta t = \Delta T/\beta$ .

For our crystals, this yields

Crystal	$C_p$ (J/kg/K)	K (W/m/K)	$\rho$ (kg/m <sup>3</sup> )	$d_{eff}$ (mm)	$\Delta T$ (K)	$\Delta t$ (s)
LiNbO <sub>3</sub>	630	4.6	6650	2.5	1.7	5.7
BaB <sub>2</sub> O <sub>4</sub>	385	1.4	3850	1.5	0.071	0.24
BaTiO <sub>3</sub>	439	6.0	6020	1.5	0.30	1.0

**Table 3.2** Temperature and time lag in the sample materials. The temperature gradient within the material results from a finite heat conductivity and a heating or cooling rate of  $|\beta|=0.3$  K/s. Calculations for at room temperature. We use the effective thickness  $d_{eff}$  of half the distance between the ceramic plates as the characteristic length.

The importance of the ceramic plates to improve the thermal contact becomes obvious in case of the LiNbO<sub>3</sub> sample which is 10 mm long in z-direction: Due to the quadratic relationship, the measurement without ceramic would increase our temperature and time differences by a factor of 16. The estimates of  $\Delta T$ ,  $\Delta t$  in Table 3.2 should be taken as best-case values, since they neglect the finite thermal conductivities of the ceramics and sample holder mount.

### 3.2.4 Measurement of Thermostimulated Luminescence

To obtain a measurement of thermoluminescence, we prepare the crystal attached to the heating element within the cryostat and evacuate below  $10^{-6}$  mbar. Then, the sample is heated to 500 K to evaporate any remaining surface contaminants. Then, the cryostat is cooled to 77 K using liquid nitrogen. At this low temperature, we illuminate the crystal through the cryostat window (~3 min, 365 nm) to fill luminescence traps. The low temperature allows us to stabilize relatively shallow traps.

The measurement begins with setting a defined heating rate (0.3 K/s) and recording temperature and emission using the photomultiplier tube at a time resolution of 1 Hz.

Pyroelectric luminescence yields relatively very weak emission, and is thus generally not observable by the naked eye. Typical intensities as detected by the photomultiplier tube (PMT) range between  $10^2$  and  $10^5$  counts per second.

### **3.2.1 Photomultiplier tube quantum efficiency**

The high sensitivity of the PMT allows to maintain a low integration time (sample rate of 1 Hz) despite the low intensities. A wavelength-dependent measurement would be beneficial for our setup, however, the sensitivity of spectrometers generally is not sufficient for these ultra-low intensities. However, boundaries of the wavelength are given by the wavelength sensitivity off the PMT.

The quantum efficiency of the photomultiplier tube ranges between 18% at 320 nm, and drops off continuously to 0% at 870 nm (see Figure 3.13). As long as the trap is close to the conduction band, the quantum efficiency is near the detector maximum.

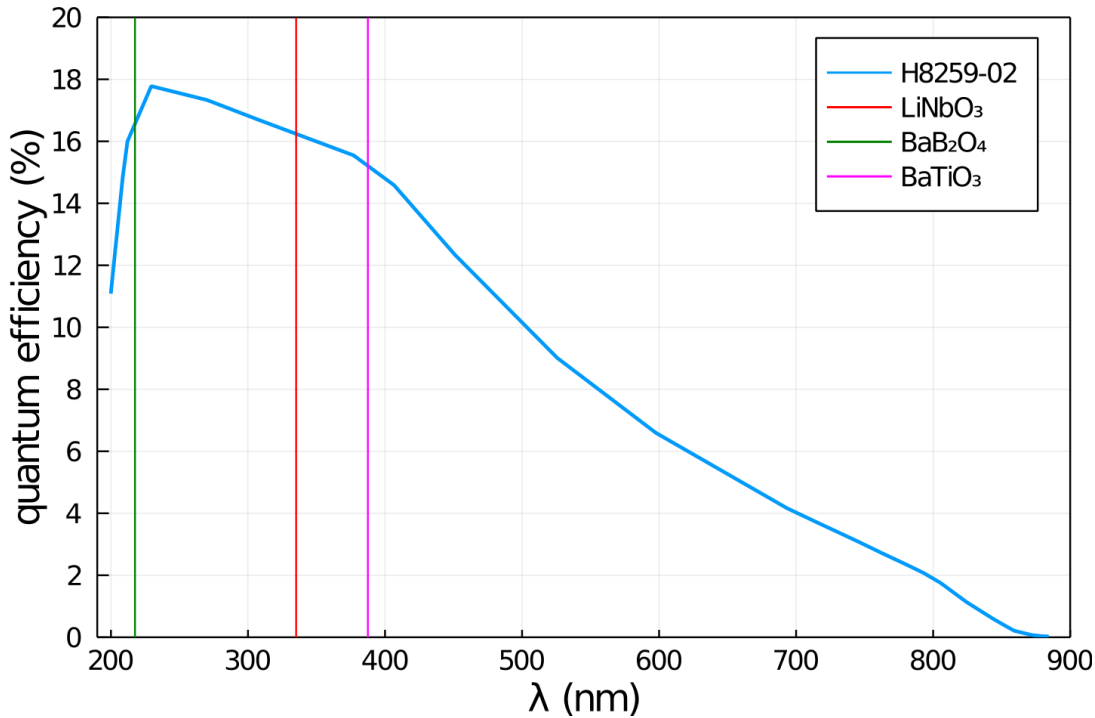


**Figure 3.13** Quantum efficiency of the Photon Counting Head Hamamatsu H8259-02, corresponding to an energy range of between 1.42 eV and 6.20 eV [143]. The band gaps of our materials are shown as comparison. They provide the minimum wavelength that can be emitted from each material.

### 3.2.2 Electric field measurement

A metal rotor rotating over the polarized surface of the crystal is used to detect the electric field. The rotor is mounted on an electric motor. The rotor blades act as a variable capacitor, detecting induced surface charges via a connected oscilloscope. This allows to quantify the electric field from the induced voltage.

The two-bladed rotor is spun at constant speed, making the blades pass with frequency  $f$  over the polarized crystal. The frequency is measured by the oscilloscope and kept

constant over the measurement. An optimum distance of 5 mm between the rotor and crystal surface was found to be sufficiently large to prevent electrical discharges, and small enough to induce sufficient charge for the measurement. Since Maxwell's equations of electrodynamics allow linear superposition, the induced charge  $\Delta Q$  is proportional to the electric field  $\Delta E$ . During rotation, the blade is exposed to an electric field change  $\Delta E$  in a timespan of  $\Delta t$ , therefore the amplitude of the induced voltage over a constant resistance  $R$  is

$$U = R \times \Delta Q / \Delta t \sim \Delta E / \Delta t \sim \Delta E \times f \quad (3.2)$$

The calibration that yields absolute values of the electric field is subsequently done by using a sample of known pyroelectric coefficient  $\gamma$ . The calibration constant  $c$  between the measured voltage amplitude  $U$  and electric field within the crystal  $E$  is

$$c = \frac{\gamma}{\varepsilon_0 \varepsilon_r} \frac{\partial T / \partial t}{\partial U / \partial t} \quad (3.3)$$

Thus, the electric field within the crystal is

$$E = cU \quad (3.4)$$

# Chapter 4

## 4 RESULTS

In this section, we present our results of both thermostimulated luminescence and pyroelectric luminescence in  $\text{LiNbO}_3$ ,  $\text{BaB}_2\text{O}_4$  and  $\text{BaTiO}_3$ . The thermostimulated luminescence is performed analogous to the pyrostimulated luminescence, with the only difference being that the electric field is short-circuited by connecting the polar surfaces with aluminum foil. We develop a model that quantitatively accounts for the dependency of luminescence on temperature and electric field. This model has three variants: Two temperature-dependent trap release mechanisms with a Coulomb and Dirac-shaped potential well, and one tunneling mechanism. We show for the first time smooth pyroelectric luminescence in  $\text{LiNbO}_3$  and  $\beta\text{-BaB}_2\text{O}_4$ , which previous studies had only done without taking the electric field into consideration. We also present luminescence measurements in  $\text{BaTiO}_3$  during various phase transitions. However, since the crystal is prone to fracture during phase transitions, this investigation proved to be challenging.

Our results are presented in an overview (Section 4.1), two sections of thermoluminescence (Sections 4.3, 4.4), and two sections of pyroluminescence (Sections 4.5, 4.6), first describing the model, followed by measurement results, respectively.

### 4.1 Qualitative Overview

We observed the relationship between emission, electric field and temperature for  $\text{LiNbO}_3$ ,  $\text{BaB}_2\text{O}_4$  crystals during cooling and heating cycles according to the experimental setup described in section 3.2. In all 4 measurements, the crystal was exposed to UV light at the starting temperature.

As detailed in section 2.3.4, the conduction in  $\text{LiNbO}_3$  and  $\text{BaB}_2\text{O}_4$  can be explained by the transport of small polarons within the insulator. The thermal activation energy of polarons that allows them to move between lattice sites can be indirectly observed by the amount of emitting recombinations that occur when the polaron is annihilated at a recombination site, or when reaching the positively charged crystal surface. Since the electric field modulates the activating energy and provides a directional bias of polaron propagation, it is expected that the recombination rate increases with the electric field strength. As can be seen in the following datasets, the trends do not show a full depletion of these polarons, which could indicate that there is a mechanism of polaron regeneration during our measurements. This appears to be true for both  $\text{LiNbO}_3$  and  $\text{BaB}_2\text{O}_4$ .

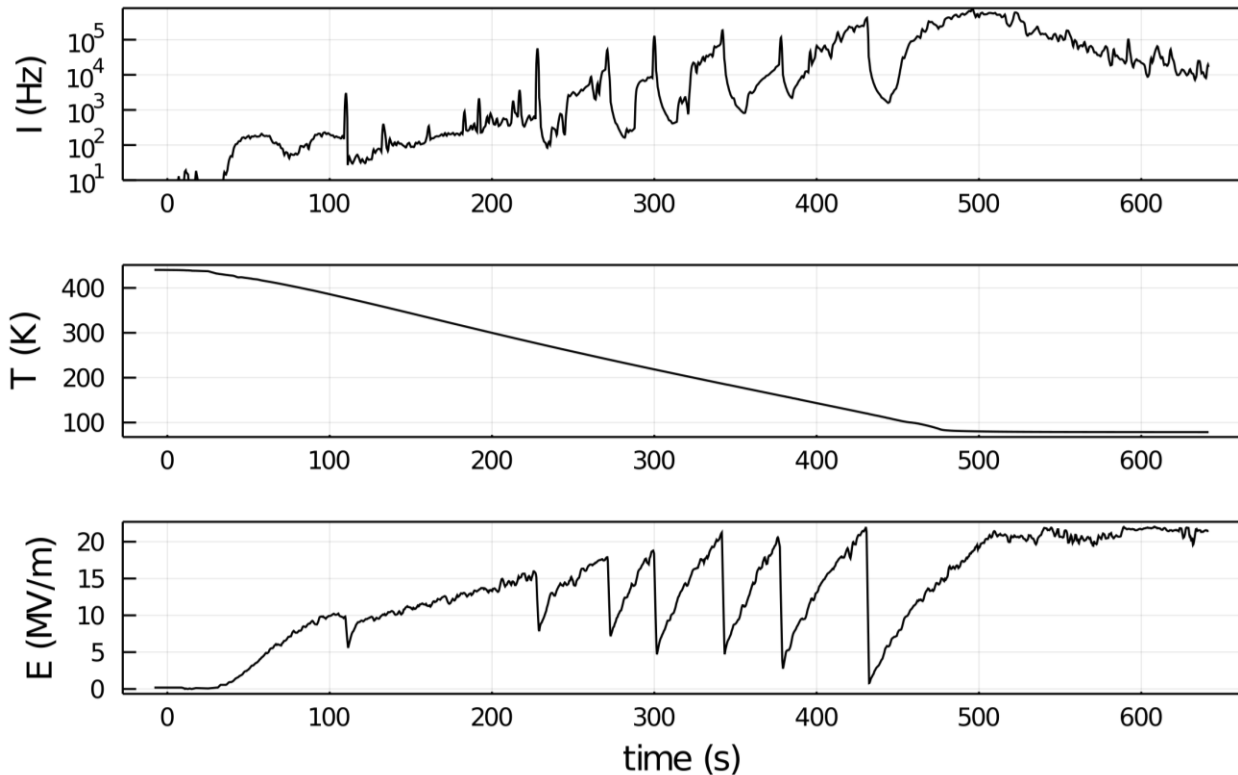


**Figure 4.1** Emission during cooling in  $\text{LiNbO}_3$ . We observe the cooling cycle of  $\text{LiNbO}_3$  starting at 440 K. Initially, we see a steady increase in the electric field, accompanied by the first emission maximum. This peak declines while the electric field is still increasing, which points to a depletion of this specific trap up to around 75 s. At around 100 s, there is a small electrical discharge, and the electric field increases at a reduced

rate. The intensity in the logarithmic plot increases linearly as well, which points to an exponential relationship between the two, up to 220 s. At around 15 MV/m, we observe periodic discharges that become increasingly large as the temperature decreases, with a peak of around 20 MV/m dropping to 2 MV/m at 440 s. As soon as the temperature settles at 77 K, no further discharges are visible, although the intensity remains large. This means that the conduction that is related to the photon emission is small compared to the total amount of pyroelectric polarization charges.

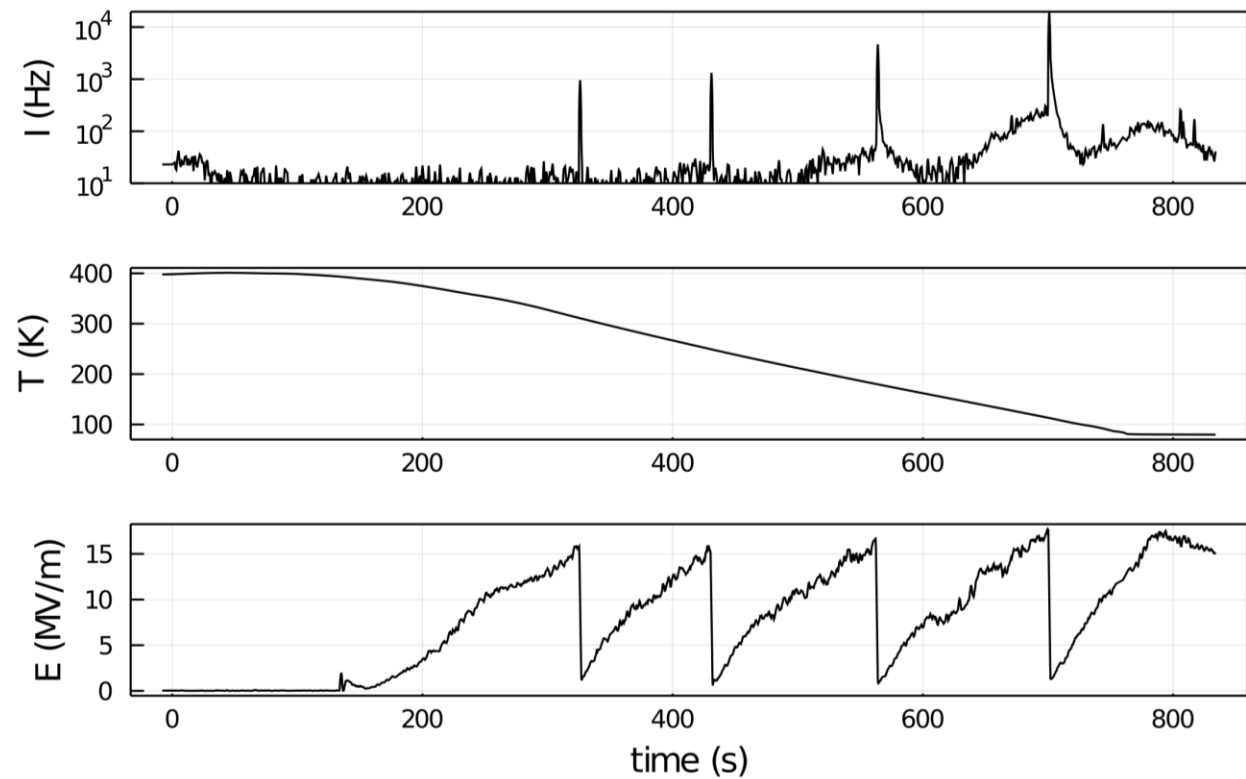


**Figure 4.2** Emission during cooling in  $\text{BaB}_2\text{O}_4$ . We observe an initial increase in the electric field with a decreased slope when the field strengths rise above  $\sim 10$  MV/m. At  $\sim 15$  MV/m, a rapid electrical discharge occurs. This pattern is repeated down to 77 K. Starting from 500s, we also observe a smooth luminescence, which is pyroelectric due to its dependence on the electric fields. There exist sufficient trapped charge carriers to show this luminescence for at least 3 iterations.

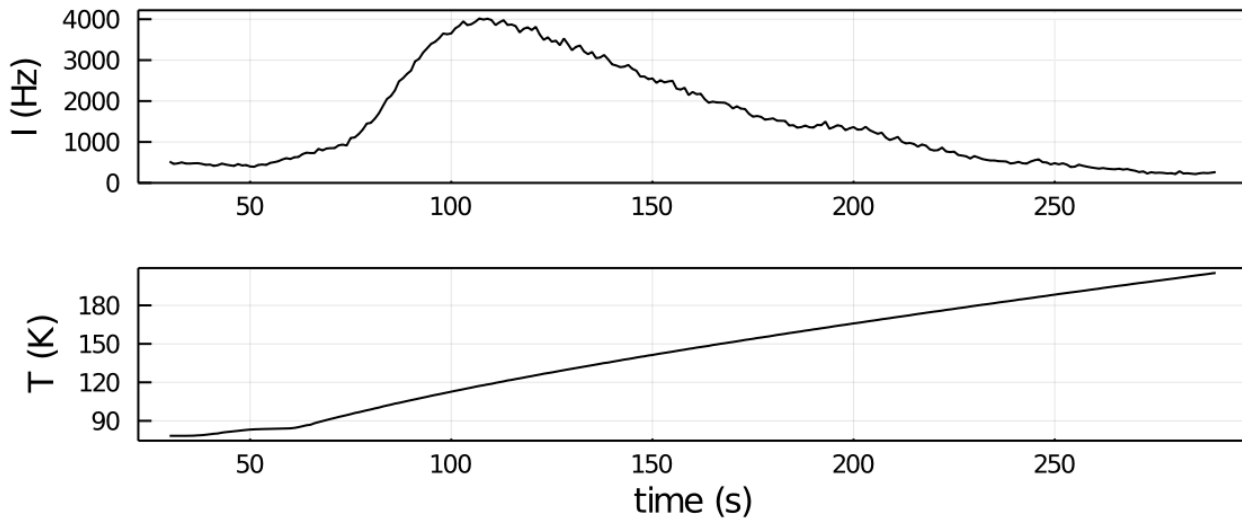


**Figure 4.3** TSL observed during the heating of  $\text{LiNbO}_3$ . The Emission starts right at the onset of heating at 77 K, and tapers off at 190 K.

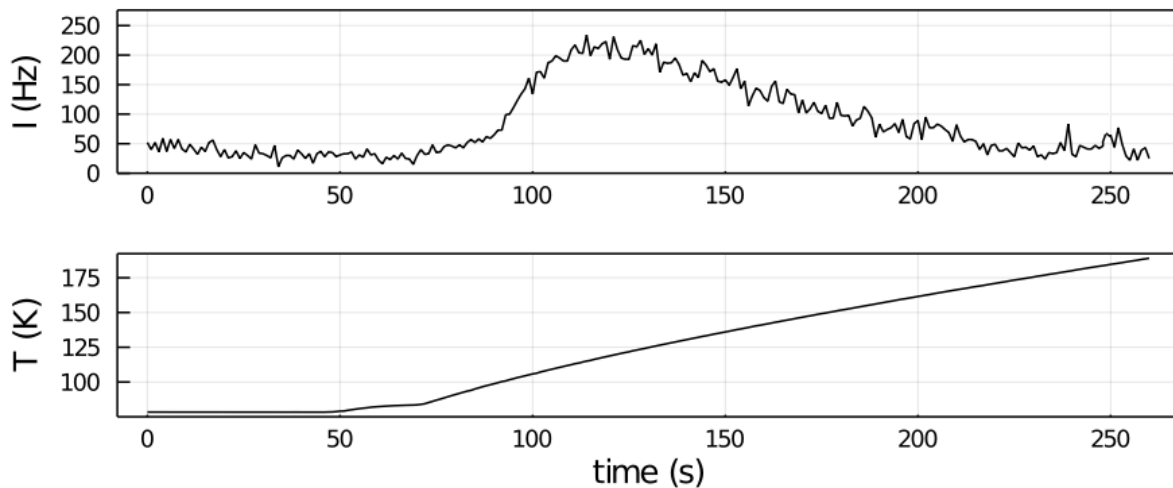


**Figure 4.4** TSL observed during the heating of  $\text{BaB}_2\text{O}_4$ . We find a continuous, smooth luminescence peak in the region between 77 K and 360 K.

## 4.2 Density of occupied traps

We can estimate the density of occupied traps  $n_t$  by

$$n_t = \frac{1}{\eta_{PMT}} \frac{1}{V_{sample}} \frac{A_{PMT}}{4\pi(d_{sample-PMT})^2} \times \int_{peak} I(t) dt \quad (4.1)$$

where  $\eta_{PMT}$  is the quantum efficiency of the PMT (see Section 3.2.1),  $A_{PMT}$  is the opening slit of the PMT,  $I(t)$  is the measured emission frequency,  $V_{sample}$  is the geometric volume of the sample, and  $d_{sample-PMT}$  is the distance between sample and PMT sensor. This assumes that the crystal itself is mostly transparent to the emitted light, and the traps are completely depleted during the process.

The equation (4.1) allows us to determine the number of traps that emit under the experimental conditions. Besides the quantum efficiency of the PMT, this calculation involves only a geometric consideration of the setup and is independent of the physical mechanism of emission.

This number becomes important when almost all traps can be filled, since the number then corresponds to the defect density within the crystal. The pre-integral factors are  $0.0156 \text{ cm}^{-3}$ ,  $0.0487 \text{ cm}^{-3}$  and  $0.0866 \text{ cm}^{-3}$  for the  $\text{LiNbO}_3$ ,  $\text{BaB}_2\text{O}_4$  and  $\text{BaTiO}_3$  crystals respectively, assuming a quantum efficiency of 0.1 at 500 nm (see Section 3.2.1). The intensity integral is determined by the following measurements.

## 4.3 Models of Thermostimulated Luminescence

Here we present the Arrhenius model, which only takes into account the initial slope to obtain the activating energy, and a heuristic model from literature that takes into account the entire luminescence peak. Both models assume negligible retrapping during the emission, which is referred to in literature by first order luminescence [54].

## 4.4 Experimental results of Thermostimulated Luminescence

In this section, we present our findings of thermostimulated luminescence in  $\text{LiNbO}_3$  and  $\text{BaB}_2\text{O}_4$ . In each case, we attach the crystal by Kapton tape to the sample holder of the heating element within the setup as described in section 3.2. After evacuation to less than  $10^{-6}$  mbar, the sample is heated to 500 K to evaporate any remaining surface contaminants, such as condensed water. Then, the cryostat is cooled to 77 K using liquid nitrogen. At this low temperature, we illuminate the crystal through the cryostat window by UV ( $\sim 3$  min, 365 nm, 3.4 eV) to fill as many luminescence traps as possible. In case of  $\text{BaTiO}_3$  ( $E_g=3.2$  eV), the excitation across the bandgap is directly possible, while for  $\text{LiNbO}_3$  ( $E_g=3.7$  eV) and  $\text{BaB}_2\text{O}_4$  ( $E_g=5.6$  eV), a two-step process is required. The low temperature allows us to allow for stable shallow trap states that would be unstable at room temperature.

The measurement begins with setting a defined heating rate (0.3 K/s) and recording temperature and emission using the photomultiplier tube.

We find that the first order kinetic model (section 2.4.2) describes the evolution of luminescence similarly well as the general order model in the three materials (section A.5). This is why we limit ourselves to the first order model here. The fitting of the general order model (Equation (A.10)) can be found in the Appendix.

### 4.4.1 Lithium Niobate

From our experiment, we find one single emission peak starting from 82 K (Figure 4.5). Smaller sparks are visible on the luminescence curve, but tiny relative to the luminescence signal.

#### 4.4.1.1 Multipeak fit

In Figure 4.5 and subsequent multipeak fits, we use the R software package tgcd to fit the emission curves [96]. The fitting parameters are listed in table Table 4.1.

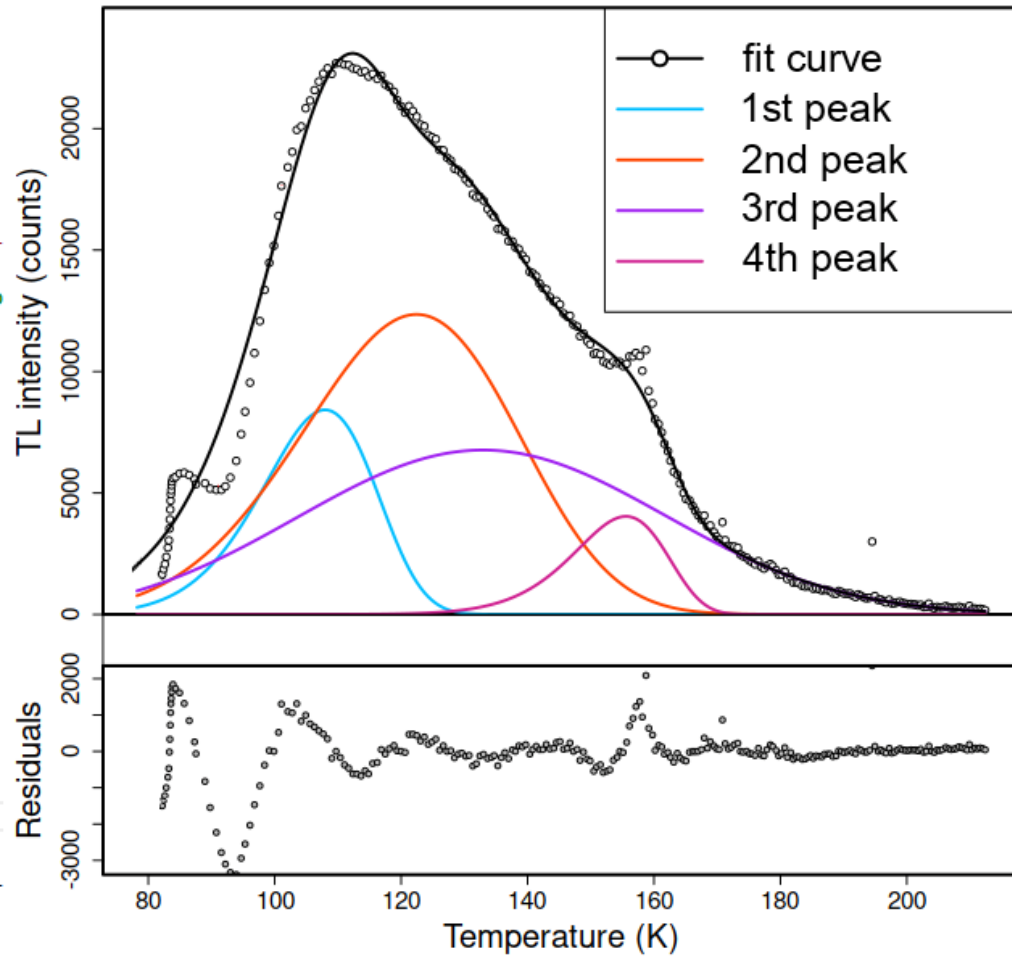


**Figure 4.5** TSL emission during heating of  $\text{LiNbO}_3$  (heuristic model). The sample was illuminated by UV light before heating from 82 K. The largest emission is visible

between 120 K and 180 K. The initial kink at 90 K is an artefact caused by the overshooting PID temperature controller. Since the emission peak appears to begin a little bit below our minimum temperature of 77 K, the accuracy of the result is likely reduced.

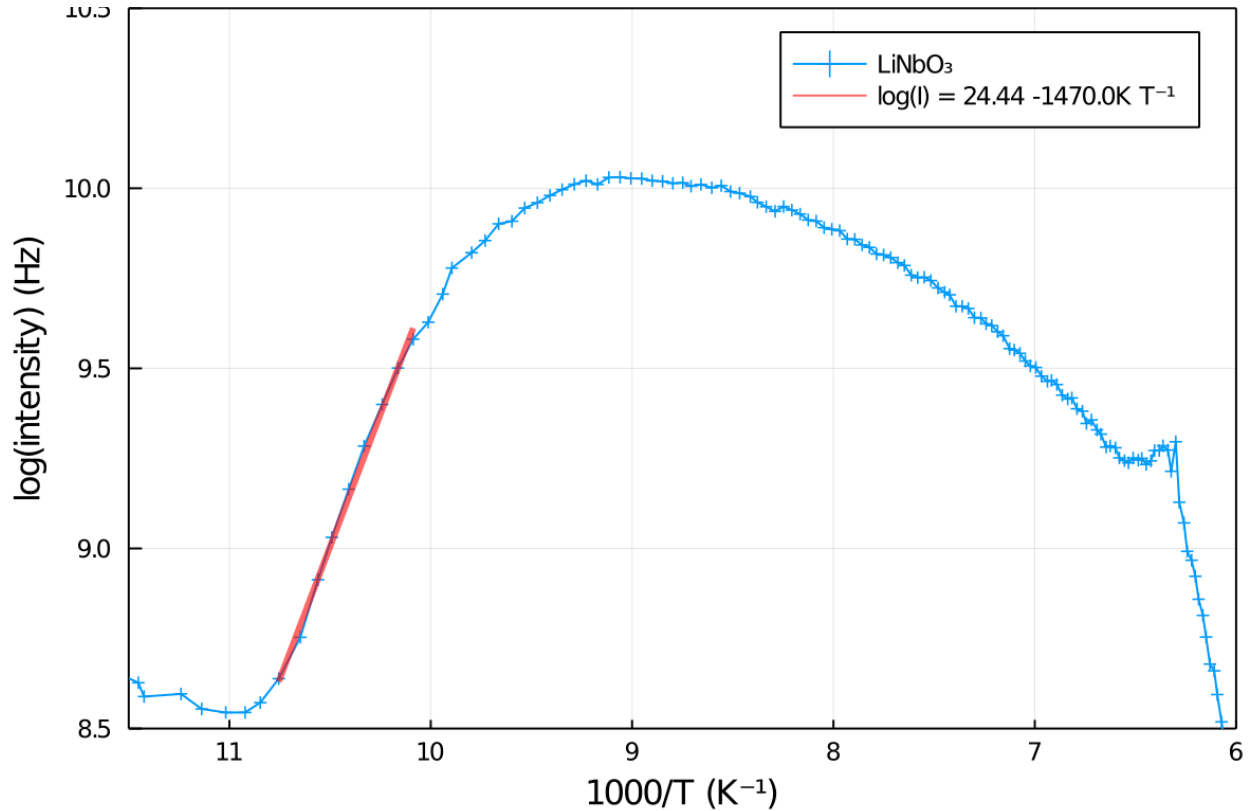
	I (Hz)	Wa (meV)	Tm (K)
1st-Peak	8430	103	108.0
2nd-Peak	12400	66.1	122.4
3rd-Peak	6770	42.7	133.0
4th-Peak	4040	269	155.6

Table 4.1 Fitting parameters of thermoluminescence model, LiNbO<sub>3</sub>

In literature, while there exist a variety of TSL measurements in doped LiNbO<sub>3</sub>, e.g. Chirila et al. 2002 [144], we have not found values for nominally pure bulk LiNbO<sub>3</sub> measured under similar conditions in order to compare these results. However, EFP measurements provide activation energies for phonon-assisted hopping transport of small free polarons around 0.2 eV to 0.3 eV, which is roughly consistent with our results. [121]. These small polarons are thought to transfer between Nb<sup>4+</sup> sites. [121]

#### 4.4.1.2 Arrhenius fit

Since the multipeak fitting form the previous section is not unambiguous, we model the onset of the emission from the Arrhenius relationship (Section 2.4.1). The heating of LiNbO<sub>3</sub> shows a clear initial linear trend in the Arrhenius plot between 93 K and 99 K. The energy from the slope of 127 meV is roughly in the same range as the 1<sup>st</sup> peak determined from the tgcd fit (103 meV, Table 4.1). This confirms that our determined activating energy is in the correct range as the first of the multipeak fits, despite the kinks in the luminescence curve that cannot be represented by the fit model.



**Figure 4.6** Arrhenius plot of the emission during the heating of LiNbO<sub>3</sub> between 87 K and 167K. The data range was chosen slightly smaller than in Figure 4.5 to remove the small initial kink. The activating energy for the TSL model is determined from the linear initial slope (red line) to be 127 meV.

## 4.4.2 Beta Barium Borate

A clear, long-lasting emission peak occurs between 80 K and 180 K. We again use a multipeak fit and Arrhenius model to compare the results.

### 4.4.2.1 Multipeak fit

Similar to the approach in LiNbO<sub>3</sub>, we find that 3 peaks are sufficient to describe the TL curve. However, due to the lower emission levels, the trend is slightly less clear (Figure 4.7). The emission is relatively low with a measured peak of just below 200 Hz. This gives rise to the large relative fluctuations during the emission, which are just statistical in nature: The standard deviation of a discrete number of statistically independent events grows with the square root of the expectation value.

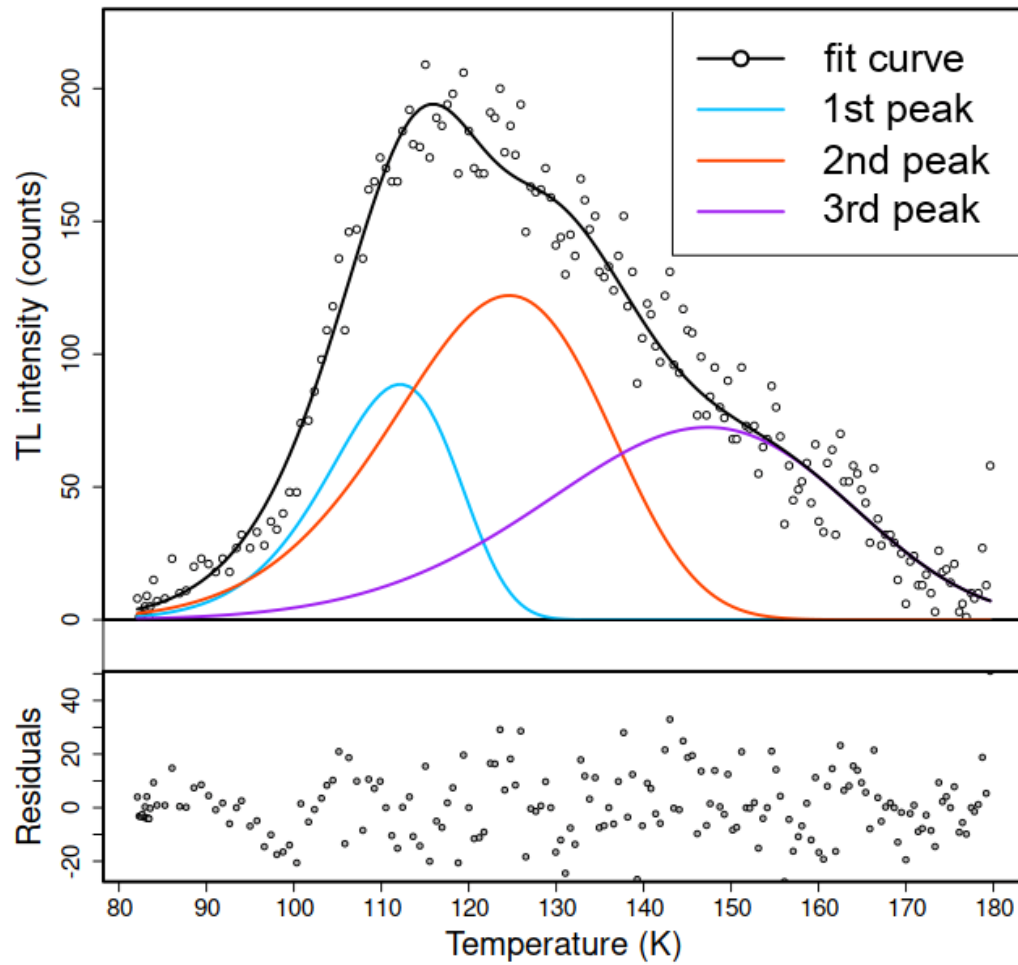


**Figure 4.7** TSL emission during heating of  $\text{BaB}_2\text{O}_4$  (heuristic model). The sample was illuminated by UV light before heating from 82 K. The largest emission is visible between 120 K and 180 K. The initial small peak at 90 K is attributed to a slight overshoot in the PID temperature controller

	I (Hz)	Wa (meV)	Tm (K)
1st-Peak	88.7	136	112.2
2nd-Peak	122	98.8	124.6
3rd-Peak	72.5	95.8	147.3

**Table 4.2 Fitting parameters of thermoluminescence model, BaB<sub>2</sub>O<sub>4</sub>**

#### 4.4.2.2 Arrhenius fit

The Arrhenius relationship (Section 2.4.1) yields an initial linear trend in the Arrhenius plot between 98 K and 105 K. The energy from the slope of 126 meV is roughly in the same range as the 1<sup>st</sup> peak determined from the tgcd fit (136 meV, Table 4.2).

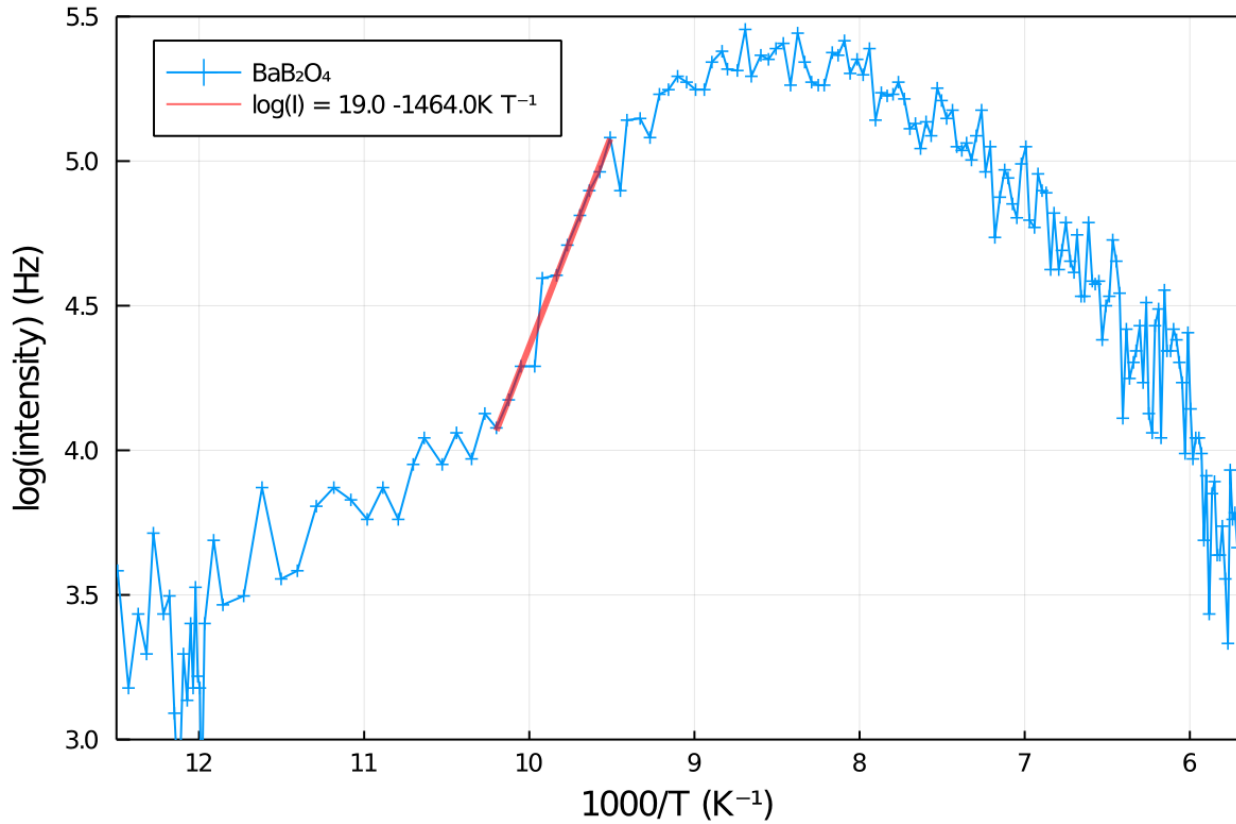


**Figure 4.8** Arrhenius plot of the emission during the heating of BaB<sub>2</sub>O<sub>4</sub> between 80 K and 172 K (same data as Figure 4.7). The activating energy for the TSL model is determined from the linear initial slope (red line) to be 126 meV.

We find that the activating energy determined by the initial slope using the Arrhenius model is again in good agreement with the first peak of the multipole fit. The magnitude of the luminescence is rather low when compared with literature [145], which may be either due to the low efficiency of generating trapped states with the UV lamp, or due to a lower amount of defects.

### 4.4.3 Barium Titanate

In the region of the large emission peak, between 80 and 180 K, the crystal remains in the rhombohedral phase. At around 190 K to 200 K, we also observe a relatively small emission that falls within the transition to the orthorhombic phase.

#### 4.4.3.1 Multipeak fit

The first order multipeak fit on BaTiO<sub>3</sub> is shown in Figure 4.9. As can be observed, the peak is composed of multiple close individual peaks that are difficult to separate. The model yields energies between 94 meV and 390 meV.

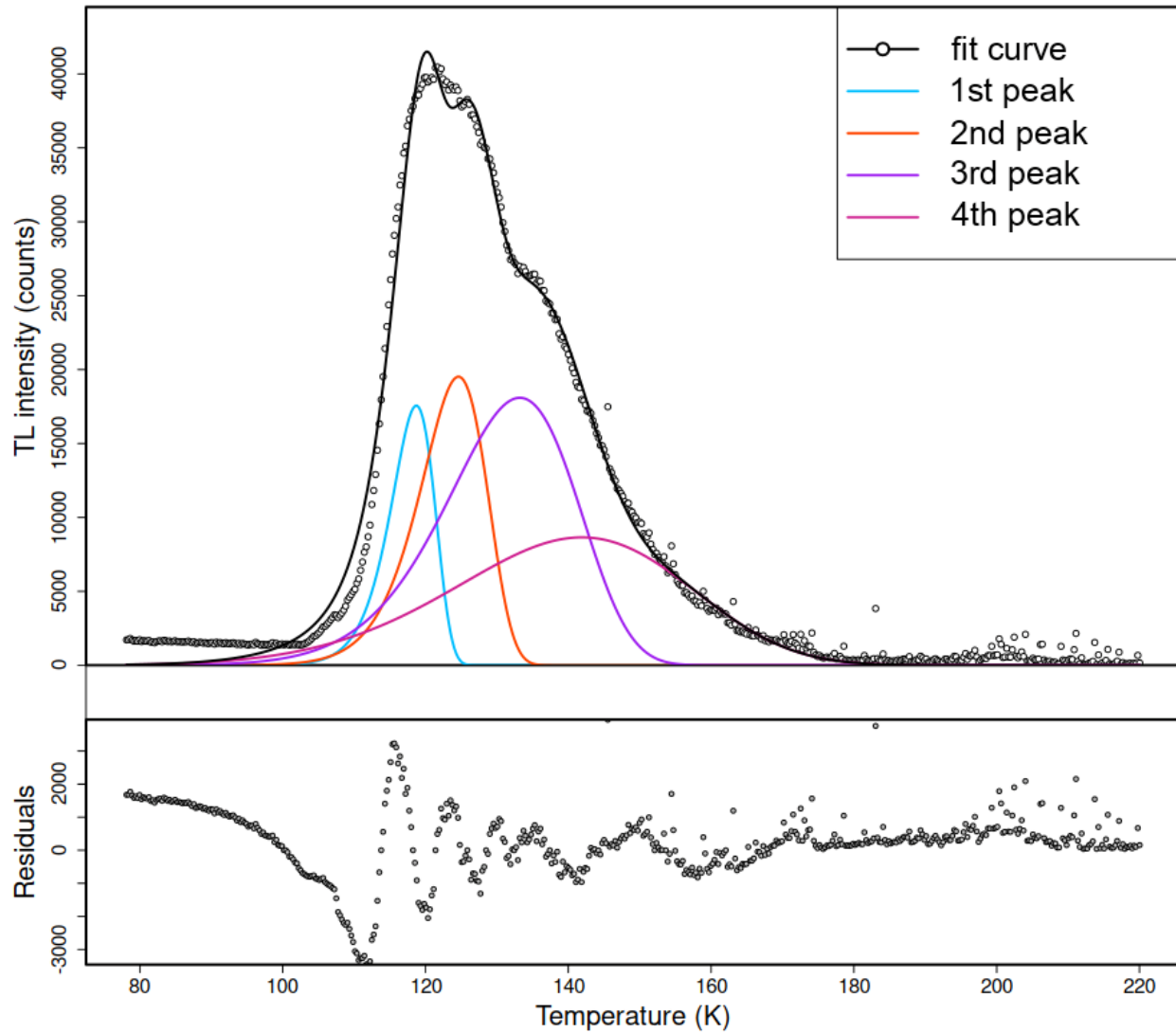


**Figure 4.9** TSL emission during heating of  $\text{BaTiO}_3$  (heuristic model). The sample was illuminated by UV light before heating from 77 K to 500 K. The largest emission is visible between 120 K and 180 K.

	I (1)	Wa (meV)	Tm (K)
1th-Peak	17600	390	118.7
2th-Peak	19500	280	124.6
3th-Peak	18100	157	133.2
4th-Peak	8650	94.0	141.9

**Table 4.3 Fitting parameters of thermoluminescence model, BaTiO<sub>3</sub>**

#### 4.4.3.2 Arrhenius fit

Since the separation into multiple peaks may not be unambiguous, the Arrhenius fit (Figure 4.10) provides a simple model to estimate at least the first activating energy of the peak group.

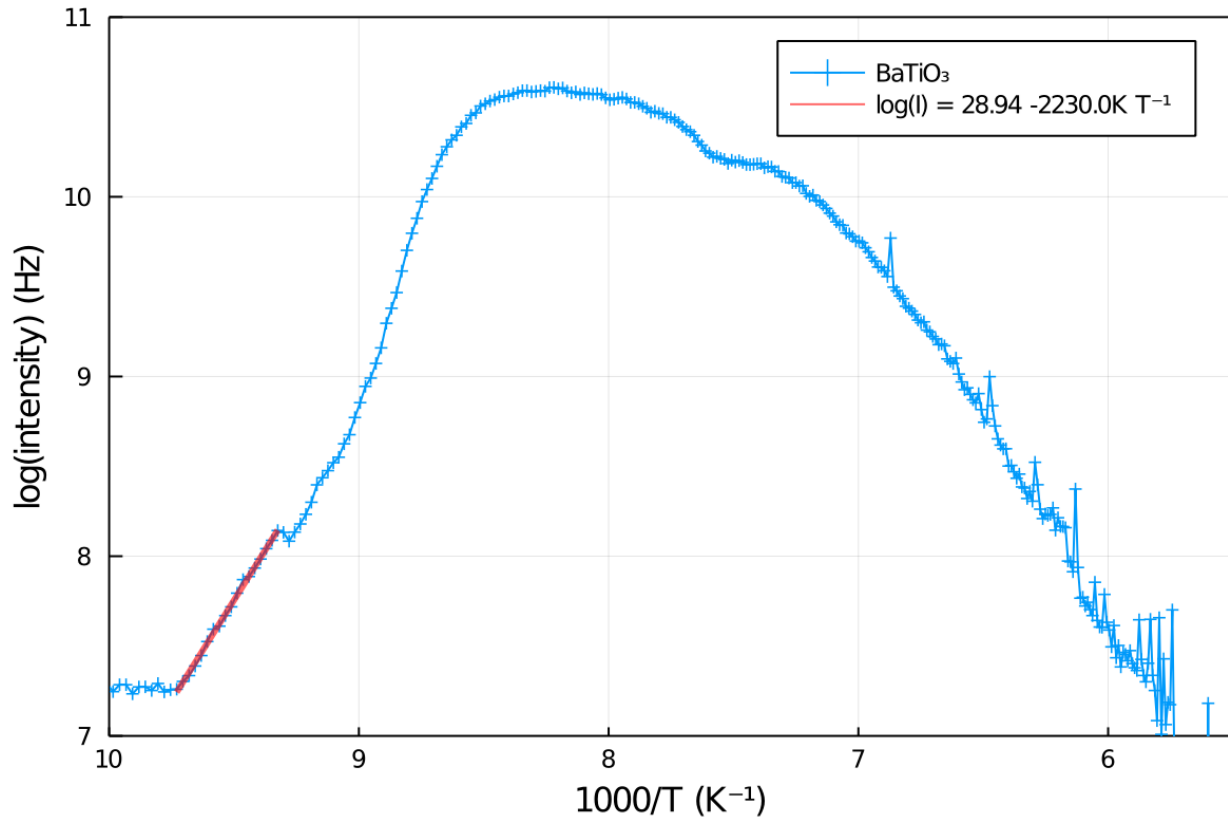


**Figure 4.10** Arrhenius plot of the emission during the heating of BaTiO<sub>3</sub>. The activating energy for the TSL model is determined from the linear initial slope (red line) to be 192 meV. The choice of the range of fitting is crucial.

The discrepancy between the first multipeak fit and the Arrhenius model is relatively large and matches more closely with the third peak. Matching thermal activating energies for defects have not been reported in literature.

Since the Arrhenius model assumes a constant number of occupied traps  $N_0$ , the model is only accurate during the onset of emission. The Arrhenius model has two shortcomings: First, we need to assume a constant number of occupied traps  $N_0$ , which only allows for fitting in a small range of the measured data in a low intensity range. Second, we neglect the effect of the electric field generated by the pyroelectric effect.

While this model is commonly used for non-pyroelectric thermostimulated luminescence, we face the additional challenge of a varying electric field with the pyroelectric crystals.

Additionally, while qualitative comparisons between the activating energies are possible, we find that the quantitative results provide unexpectedly large activating energies.

For this reason, we develop a more sophisticated, generalized model that takes into account the effects of the electric field, as well as other mechanisms besides a simple thermal activation.

#### 4.5 Model of Smooth Pyroelectric Luminescence

Our model takes into account variants of a trapped charge carrier to be released into the conduction band. The subsequent relaxation is assumed to account for the emitted light. Here, we derive our quantitative model to describe this process.

First, we express the emission rate of electrons in trapped states  $\partial N / \partial t$  to be proportional to the number remaining states  $N(t)$  and the emission rate  $\Gamma(t)$ . Assuming negligible replenishing of trap states during the measurement, the depletion rate of electrons in trapped states  $\partial N / \partial t$  is proportional to the number of remaining states  $N(t)$  and the emission rate  $\Gamma(t)$ :

$$\frac{\partial N(t)}{\partial t} = -N(t) \Gamma(t) \quad (4.2)$$

Solving by separation of variables and integration between  $t_0$  to  $t$  yields

$$N(t) = N_0 \exp\left(-\int_{t_0}^t \Gamma(t_1) dt_1\right) \quad (4.3)$$

where  $N_0 = N(t_0)$  is the initial amount of trapped states. The measured intensity of emitted photons  $I(t)$  is thus proportional to the trap depletion rate  $\partial N / \partial t$

$$I(t) = -c_2 \frac{\partial N(t)}{\partial t} \quad (4.4)$$

where  $c_2$  accounts for the number of photons emitted per trap emission and the probability of measuring a photon. Substituting (4.2), (4.3) into (4.4) yields

$$I(t) = N_0 c_2 \Gamma(t) \exp\left(-\int_{t_0}^t \Gamma(t_1) dt_1\right) \quad (4.5)$$

where the emission rate is a temperature and electric field dependent emission rate  $\Gamma(t) = \Gamma(T(t), E(t))$ .

To describe the emission rate  $\Gamma(t)$ , we consider three scenarios shown in Figure 4.11: The first two describe thermally activated processes of different potential shapes (a) and (b), where the electric field modulates the energy barrier  $\Delta W$ . The last one (c) describes a Fowler-Nordheim tunneling process without temperature effects. In this process, the electric field modulates the width of a trapezoidal tunneling barrier  $a$ .

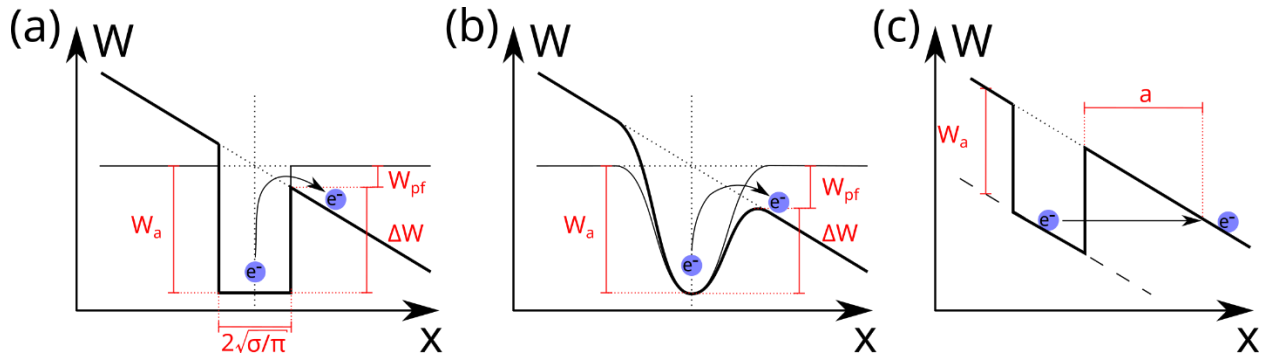


**Figure 4.11 Trap release mechanisms of electrons: (a) Dirac-well, (b) Coulomb potential, (c) Fowler-Nordheim Tunneling [104]**

The Poole–Frenkel effect is a bulk-limited conduction mechanism which depends on the trap energy levels in the dielectric material. It is similar to Schottky emission i.e. the thermal excitation of electrons may emit from traps into the conduction band of the dielectric. The classical Poole-Frenkel emission rate as shown in Figure 4.11(a) is [67]

$$\Gamma_{\text{coulomb}} = c_1 \exp\left(\frac{-W_a - \Delta W_{pf}}{k_B T}\right), \quad W_{pf} = \sqrt{\frac{q^3 E}{\pi \epsilon_\infty \epsilon_0}}, \quad (4.6)$$

In case of a Dirac well (Figure 4.11(b)), we obtain [146]

$$\Gamma_{\text{dirac}} = c_1 \exp\left(\frac{-W_a - W_{pf}}{k_B T}\right), \quad W_{pf} = qE \sqrt{\frac{\sigma}{\pi}} \quad (4.7)$$

With the fitting parameters  $N_0, c_1, c_2, W_a, \sigma, \epsilon_\infty$  respectively.  $\sigma$  is the cross section of the potential well,  $\epsilon_\infty \approx n^2$  is the high frequency (optical) permittivity, and  $W_a$  is the activation energy of the trap.

Finally, the high pyroelectric field may result in emission of trapped charge carriers due to Fowler-Nordheim tunneling (FNT), as shown in Figure 4.11(c), primarily depending on the magnitude of the electric field. For a very high electric field and low temperatures, FNT will always dominate thermally induced effects. The FNT emission rate takes the form [69]

$$\Gamma_{\text{FNT}} = c_1 \frac{E^2}{W_a} \exp\left(-\frac{8\pi\sqrt{2m^*}}{3hq} \frac{W_a^{3/2}}{E}\right) \quad (4.8)$$

where  $m^*$  is the effective mass of the charge carrier.

## 4.6 Experimental results of SPEL

We measured pyroelectric luminescence in LiNbO<sub>3</sub>,  $\beta$ -BaB<sub>2</sub>O<sub>4</sub> under heating and cooling conditions and compare the results with our models from the previous section. Depending on the field and temperature magnitudes, the thermally activated models and tunneling can occur in the same material. For high temperatures and moderate electric fields, the Poole–Frenkel effect dominates, while low temperatures and high electric fields promote Fowler–Nordheim Tunneling.

Following the same procedure as with the TSL measurements, we first evacuate the cryostat to less than 10<sup>-6</sup> mbar, and heat the sample to 500 K to evaporate any remaining surface condensation.

In principle, the trap energy level can be extracted by using an Arrhenius plot (Section 2.4.1). However, this limits the fit to a small, subjectively chosen region of that describes the initial slope. We avoid this problem by using our model (see Section 4.5) that incorporates the effects of temperature and trapped electron depletion. This allows us to take into account the full data range. The pyroelectric field results in lowering of the Coulomb barrier for the trapped carriers and aids in radiative recombination [55]. An important consequence is that the potential barrier in SPEL is not fixed like in TSL but temperature-dependent.

### 4.6.1 Lithium Niobate

Our first result focuses on a sample of congruent lithium niobate. We use the experimental setup and procedure as described in Section 3.2. The electric field, SPEL intensity and temperature are recorded. The calibration procedure for the electric field within the crystal is done as explained in Section 4.5.

The pyroelectric coefficient in LiNbO<sub>3</sub> is relatively large. Literature specifies its value at about -38 uC/m<sup>2</sup>/K.

The luminescence curve for heating of LiNbO<sub>3</sub> did not show any clear peaks without either an initial field reversal due to the previous cooling, or intermediate sparks (see for e.g. Figure 4.4). For this reason we focus on the cooling results from our experiments, for which we find a characteristic emission in the range between 440 K to 360 K. The experimental results are illustrated in Figure 4.12.

We observe that the electric field, which in a pyroelectric should constantly increase during cooling, shows a decrease at the peak position at ~400 K at 22.8 MV/m. The electrical conductivity should only increase with lowering temperatures. Also, the trap activation should only limit the electric field, since it is driven only by the electric field during cooling. However, we find that the electric field drops by about 10% (2 MV/m), which points to an increase of free charge carriers during the emission.

We fit the two Poole-Frenkel field-assisted lowering of the activating energy models with a Coulombic and Dirac well (see Equation (4.6)(4.7)), as well as the FNT model (Equation (4.8)). A visual comparison between the fitted models shows that the Dirac potential follows the measurement most accurately, while the Coulomb potential results in a too wide spread of the peak, while the FNT model shows a too narrow peak due to its high field sensitivity. The values obtained from the fit are shown in Table 4.4. The parameter  $N_0$  is the number of charges initially confined in trap states,  $c_2$  accounts for the number of photons emitted per trap emission and the probability of measuring a photon. Together, they provide the fitting parameter  $N_0 c_2$ , which is the number of overall measured photons.

The attempt frequency of a trapped charge carrier  $c_1$  is quite small in case of the two barrier jumping models, the FNT model frequencies are higher than expected (values relative to the electric field squared). However, the activating energies  $W_a$  are found in a similar regime between 515 meV and 760 meV for all our models.

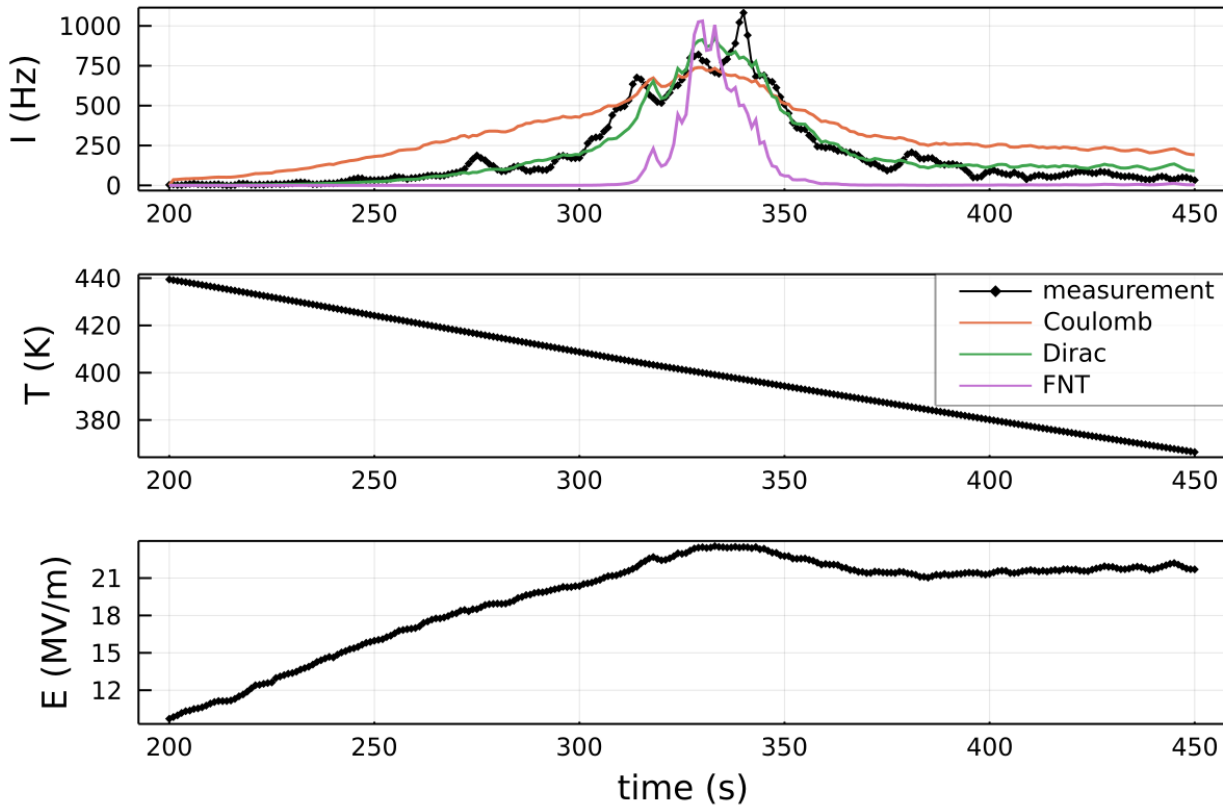


**Figure 4.12** LiNbO<sub>3</sub> SPEL emission during cooling.

The emission was observed at fields of 22 MV/m during cooling between 440 K and 360 K. We show that a Poole–Frenkel model with a Dirac-shaped potential provides a good description of the dynamics of the emission and even a quantitative determination of material parameters including the trap depth, as well as the FNT model. We established a method to simultaneously observe the electric field and emission, which allows the determination of the deep defect activation energies, which are inaccessible by pure thermal stimulation.

	$N_0 c_2$ (1)	$c_1$ (Hz)	$W_a$ (meV)	$\epsilon_r^\infty$ (1)
Coulomb	$6.4 \times 10^6$	2.6	515	$n^2$
Dirac	$N_0 c_2$ (1)	$c_1$ (Hz)	$W_a$ (meV)	$\sigma$ (nm <sup>2</sup> )
	$6.52 \times 10^6$	108.4	760	49
FNT	$N_0 c_2$ (1)	$c_1$ (Hz eVm <sup>2</sup> /V <sup>2</sup> )	$W_a$ (meV)	-
	$2.06 \times 10^4$	$1.84 \times 10^6$	678	-

**Table 4.4 SPEL model parameters for LiNbO<sub>3</sub> during cooling acquired during the cooling cycle between 430 K and 390 K.**

From the obtained fittings, we see that all three models show activating energies within similar values. The Dirac model has effectively one more free parameter, as compared to the Coulomb and FNT models, which allows it to fit better. However, the rectangular potential well is likely the least accurate representation of the actual potential cross section along the direction of the electric field.

We see that the attempt frequencies  $c_1$  for both the Coulomb and Dirac potentials appears too small to what is typically found in literature, while the values for FNT are too large. We find that this value is highly sensitive to small perturbations in the measurement and fitting procedure. For this reason, this parameter should not be considered as physically accurate. The activating energy, however, is relatively stable, and mostly independent of this frequency factor.

When compared to the TSL measurement from section 4.4.1, we find about a quarter of the activating energy at a quarter of the temperature. Thus, we are certainly dealing with a deeper trap type in the SPEL experiment. Despite extensive literature research, we have not found similar results in literature with SPEL emission.

#### 4.6.2 Beta-Barium Borate

In this section, we repeat the measurement from the previous section with a Barium  $\beta$ -Borate ( $\beta\text{-BaB}_2\text{O}_4$ ) crystal in the temperature range 80–400K for both heating and cooling cycles. In the temperature regime that we investigate,  $\text{BaB}_2\text{O}_4$  remains in the low-temperature, non-centrosymmetric  $\beta$ -form with R3c space group. It has a band gap of 5.6 eV (215 nm) and the crystals have a fairly high pyroelectric coefficient  $\sim 15 \mu\text{C/m}^2 \text{ K}$  [61], which remains almost constant in the range of 100 –300 K. As a result, temperature

changes of the crystal can generate large electric fields. The sample is an undoped Newlight 3x3x5cm shape crystal with the polarization axis along the 5 cm axis.

The resulting temperature, emission and field curves are shown in Figure 4.13 (heating) and Figure 4.14 (cooling).

The luminescence spectrum is continuous with intensities peaking between 240 K and 260 K in both the cycles. The resulting smooth emission curves are fitted with the emission models from Section 4.5. The fitting parameters are provided in Table 4.5 and Table 4.6. The electric field reaches a plateau when the intensity peak occurs, and then continues to rise afterwards. This is in contrast to the slightly decreasing field in LiNbO<sub>3</sub>.

It is evident that the all the models fit the heating curve (Figure 4.13) well. However, the FNT model provides the best fit to the cooling curve (Figure 4.14). Although all the models fit the experimental data, the fitting parameters for the Poole-Frenkel models reveal unrealistic values for the models to truly describe the underlying physical process. For instance, the attempt frequency  $c_1$  for the trapped state is unphysically high (Table 4.5, Table 4.6). Compared to this, Fowler-Nordheim frequencies are found in a plausible range.

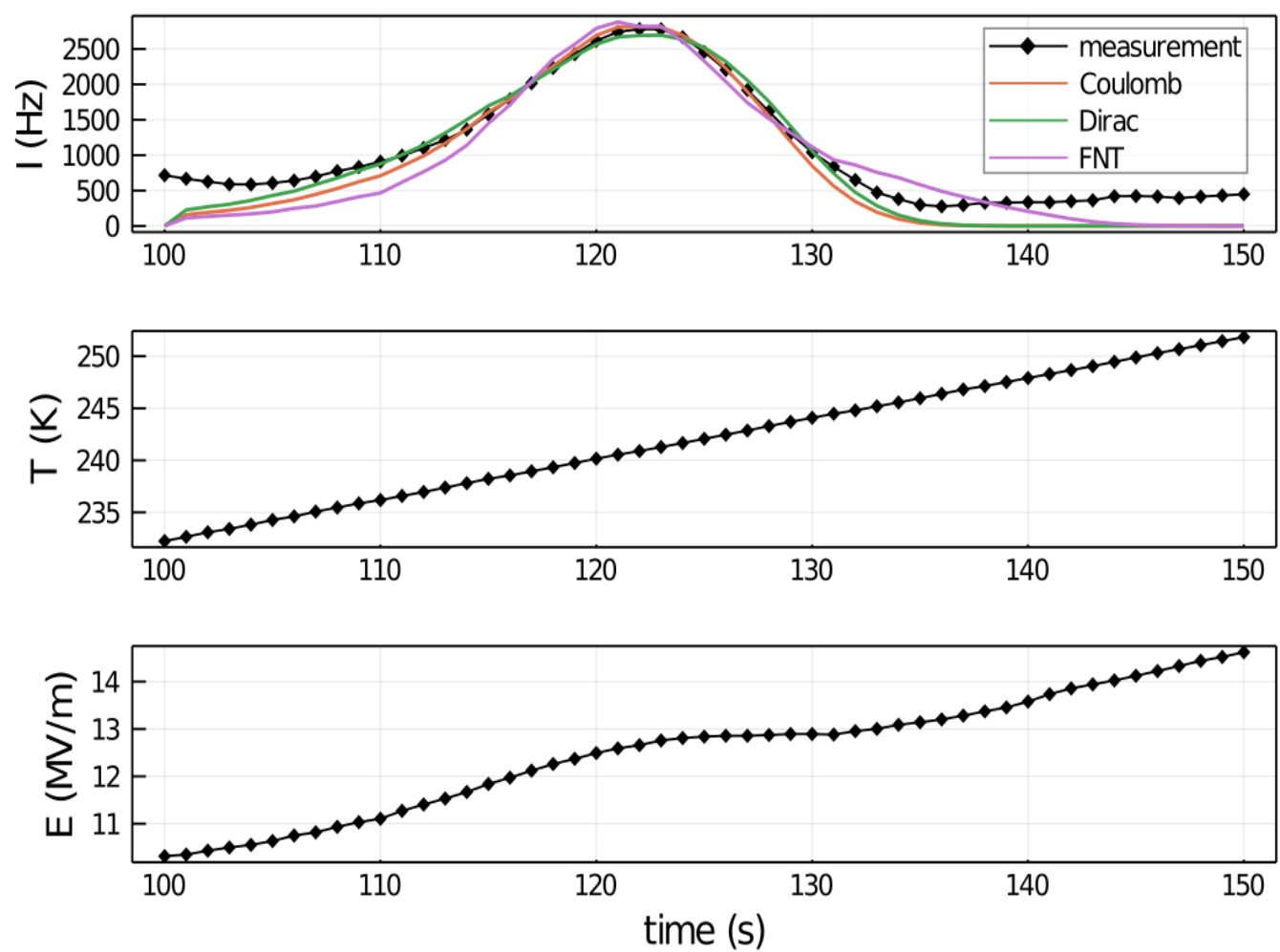


**Figure 4.13** BaB<sub>2</sub>O<sub>3</sub> SPEL emission during heating. The peak is located between 232 K and 252 K, at an electric field of about 13 MV/m.

Coulomb	$N_0 c_2$ (1)	$c_1$ (Hz)	$W_a$ (eV)	$\epsilon_{r\infty}$ (1)
	$3.58 \times 10^{26}$	$4.10 \times 10^{21}$	4.25	$2.80 \times 10^{-2}$
Dirac	$N_0 c_2$ (1)	$c_1$ (Hz)	$W_a$ (eV)	$\sigma$ (nm <sup>2</sup> )
	$1.02 \times 10^{23}$	$7.89 \times 10^{17}$	2.67	$5.24 \times 10^3$
FNT	$N_0 c_2$ (1)	$c_1$ (Hz eVm <sup>2</sup> /V <sup>2</sup> )	$W_a$ (eV)	-
	$1.71 \times 10^5$	$1.56 \times 10^{-6}$	0.367	-

Table 4.5 SPEL model parameters for the heating cycle of BaB<sub>2</sub>O<sub>4</sub>. Parameters are fits of equation (4.5) using the three emission rates (4.6)(4.7)(4.8)).

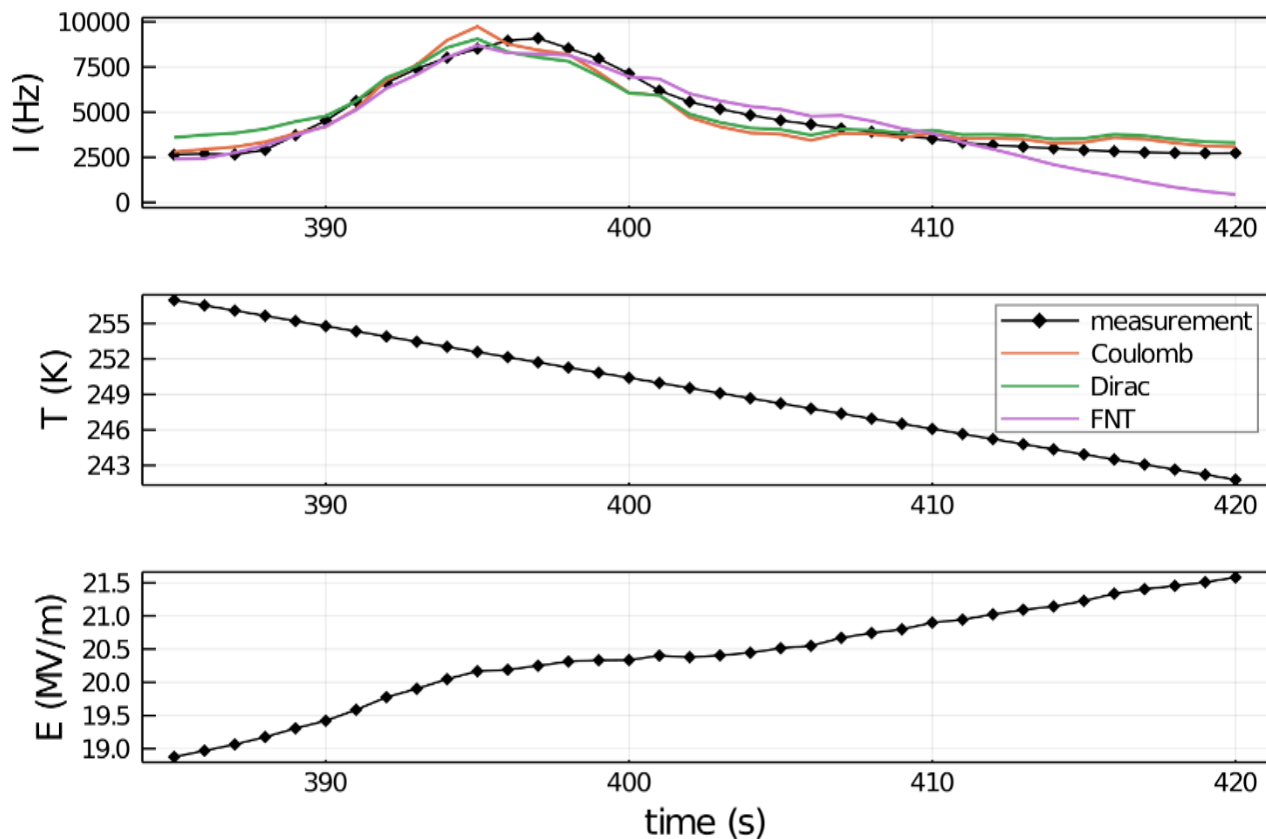


Figure 4.14 BaB<sub>2</sub>O<sub>4</sub> SPEL emission during cooling. Comparison of measured cooling data (black) of  $\beta$ -barium borate with numerical models (top). The black line between data points is merely a guide to the eye. Colors in the upper and the middle figure correspond to the same models.

Coulomb	$N_0 c_2 (1)$	$c_1 (\text{Hz})$	$W_a (\text{eV})$	$\epsilon_r^\infty (1)$
	$4.91 \times 10^{22}$	$1.812 \times 10^{21}$	3.83	0.0466
<b>Dirac</b>	$N_0 c_2 (1)$	$c_1 (\text{Hz})$	$W_a (\text{eV})$	$\sigma (\text{nm}^2)$
	$2.68 \times 10^{24}$	$1.43 \times 10^{20}$	2.96	3678
<b>FNT</b>	$N_0 c_2 (1)$	$c_1 (\text{Hz eVm}^2/\text{V}^2)$	$W_a (\text{eV})$	-
	$1.82 \times 10^5$	0.1818	0.403	-

Table 4.6 SPEL model parameters for the cooling cycle of  $\text{BaB}_2\text{O}_3$ .

In summary, our investigation is the first to demonstrate smooth pyroelectric luminescence in beta barium borate. We provide a comparative study of different emission models and identify that the luminescence is consistent with a trap release mechanism that follows a Fowler-Nordheim-type behavior. The heating and cooling parameter predictions are in close agreement. We obtain an activating energy of the trap of  $W_a=370$  meV and 400 meV for heating and cooling, respectively.

#### 4.6.3 Barium Titanate: Luminescence during phase transitions

The measurement of  $\text{BaTiO}_3$  analogous to  $\text{LiNbO}_3$  and  $\text{BaB}_2\text{O}_4$  shows electrostatic discharges over the full range of the signal (Figure 4.16). This may be due to both the smaller bandgap and the phase transitions that induce defects. Since this signal makes a consistent fitting of any smooth pyroelectric luminescence model difficult, we use the luminescence signal to observe the relation to the various phase transitions that occur in the temperature range of our experiment.

These phase transitions can induce high electric fields in the vicinity of the domain wall. This is due to the large change in pyroelectric coefficient and dielectric permittivity between the phases (see Figure 4.15), which in turn could trigger smooth pyroelectric luminescence.

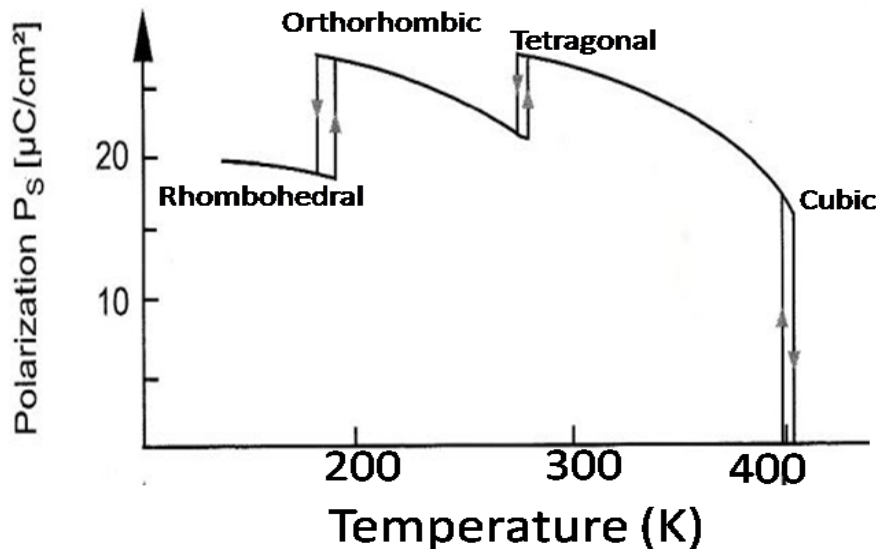


**Figure 4.15 Spontaneous polarization in  $\text{BaTiO}_3$  during phase transitions [ 136]**

In Figure 4.16, we present the luminescence during heating between 150 K and 440 K, with superimposed regions of phase transition. As shown in the figure, at least the orthorhombic-tetragonal, as well as the tetragonal-cubic crystal phases are clearly visible within the intensity spectrum.

According to Figure 4.15, the first two transitions come with a large increase in polarization, which goes to zero at the final transition. The effect of these phase transitions on the emission of the  $\text{BaTiO}_3$  crystal is shown in Figure 4.16. The rhombohedral-orthorhombic transition shows no clear change in emission, which is relatively low and picks up once we approach the orthorhombic-tetragonal transition during which we have a large change in spontaneous polarization. The same happens for the tetragonal. Finally, during the phase transition to the nonpolar cubic phase, the emission becomes zero, since the electric field becomes constant.

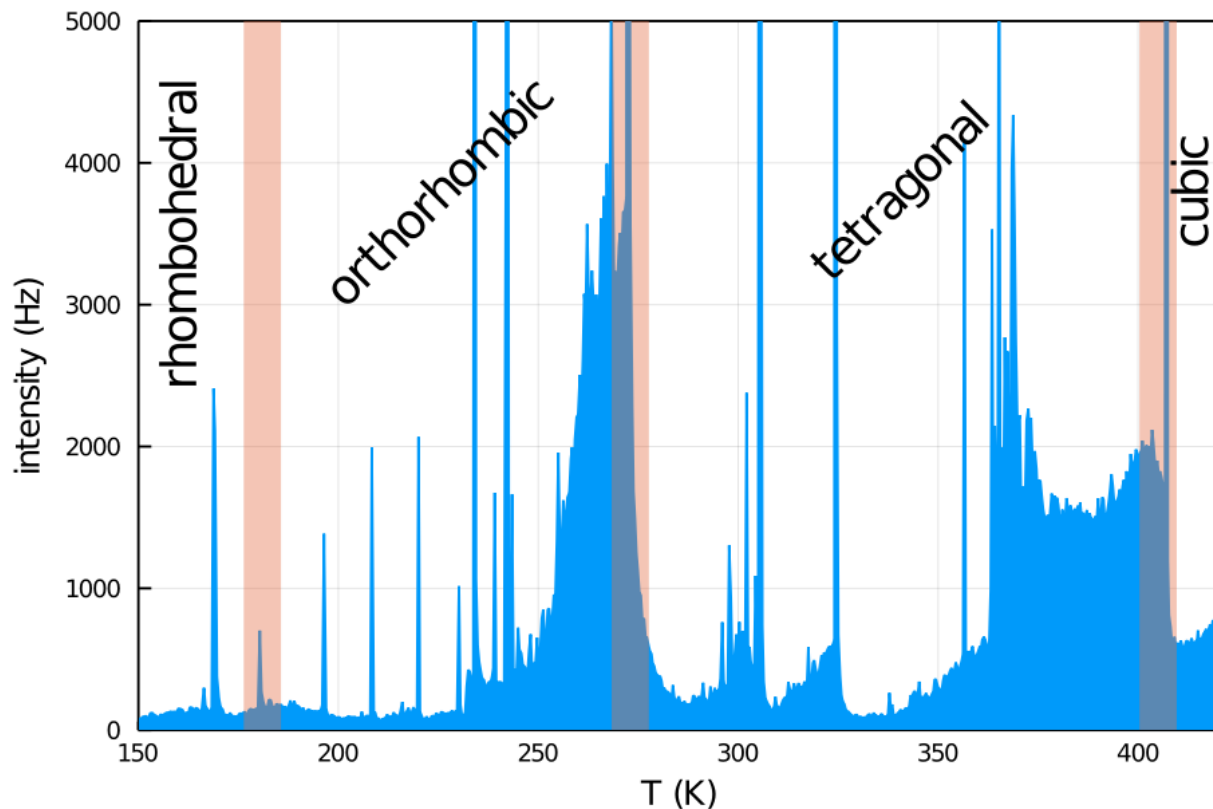


**Figure 4.16 Barium Titanate:  $\text{BaTiO}_3$ . Emission during heating.**

Parameter phase change	T K	$\mu\text{C}/\text{m}^2/\text{K}$	$\epsilon_r$ (1)	observed during heating	luminescence
rhombohedral	<90	30 to 100 at 90 K		Low, constant emission, sparks	
orthorhombic		50		steadily increasing, sparks	
tetragonal			66.6	rapid drop after transition, increasing after 350 K, sparks	
cubic		0		rapid drop after transition	

**Table 4.7 Phase parameters in  $\text{BaTiO}_3$**

The emission spectrum of our  $\text{BaTiO}_3$  sample is rich in emission peaks that are intermixed with sparks. This behavior is may be mostly defined by the phase transitions that create

new traps and conductive channels. Additionally, bulk BaTiO<sub>3</sub> is known to suffer permanent damage during these phase transitions, which will continuously increase the number of defects.

# Chapter 5

## 5 SUMMARY AND CONCLUSION

### 5.1 Summary

Luminescence phenomena are mechanisms of releasing stored energy from a dielectric sample. This effect has classically been triggered by heat, in which case it is called Thermally Stimulated Luminescence. It has since been found that other triggers exist, such as electric fields, which has been termed Pyroelectric Luminescence in case of an intrinsically-generated field, or electroluminescence in case of an externally applied field.

The topic of pyroelectric luminescence and luminescence phenomena in general have seen a low rate of academic interest within recent years. Despite this, there exist many unanswered questions and unexplained phenomena in materials that are of high technological and scientific interest.

A variety of technical applications, which serve to investigate different material properties such as crystal defects in semiconductors. Indeed, a wide range of experimental methods has been used to study crystal defects [5].

Our research addressed the study of thermostimulated luminescence and pyroluminescence in three materials of high technological importance. We established a measurement setup to allow for the acquisition of both the luminescence and electric field within a temperature- and pressure-controlled environment. In case of thermoluminescence, the vacuum is just used to avoid moisture during cooling, and the electric field generated by the pyroelectric crystal is short-circuited. In case of pyroluminescence, the low pressure is also required to avoid electrical discharges to obtain high electric fields. Avoiding these sparks that lower the electric field and produce a strong emission on their own is critical for a successful measurement.

In principle, the trap energy level can be extracted by using an Arrhenius plot i.e. a linear fit of  $\ln(J/E)$  vs  $E^{1/2}$ . However, this limits the fit to a small, subjectively chosen region of the initial slope. We avoid this problem by using a method that incorporates the effects of temperature and trapped electron depletion, which allows us to take into account the full data range. The pyroelectric field results in lowering of the Coulomb barrier for the trapped carriers and aids in radiative recombination[55].

Our key results include the activating energy of shallow traps and related parameters with regards to the thermostimulated luminescence. With regards to pyroelectric luminescence, we developed models to predict the activation of deep traps and their parameters, such as the activation energy, and the trap escape frequency amongst others. The materials  $\text{LiNbO}_3$  and  $\beta\text{-BaB}_2\text{O}_4$  were both investigated using these techniques. In case of  $\text{BaTiO}_3$ , we were only able to obtain results for thermoluminescence, since the single crystal is prone to shattering during phase transition. We have found a relationship between certain phase transitions and the luminescence signal emitted from this material.

In  $\text{LiNbO}_3$ , as well as  $\beta\text{-BaB}_2\text{O}_4$  we were able to identify distinct deep trap states.

In  $\text{LiNbO}_3$ , we have found that the activating energies obtained from our measurements are consistent with the small bound polarons given in literature. The activating energies determined from our models yield values between 515 meV and 760 meV. These values are consistent with small bound polarons at the substitutional defect of  $\text{Nb}_{\text{Li}}^{5+}$ , which is specified with thermal activating energies of 0.65 eV. [121].

We find that all materials show multiple pyroelectric luminescence peaks, and we were the first to report on the luminescence in  $\beta\text{-BaB}_2\text{O}_4$ . We also looked at the behavior of  $\text{BaTiO}_3$  emission during phase change and found that the luminescence shows a strong correlation with the phase change.

Parameter	TSL	SPEL
Pyroelectric materials	✗	✓
Electric field	✗	✓
Defects	shallow only	also deep
Vacuum required	✗	✓ 10 <sup>-7</sup> mbar
Heating	✓	✓
Cooling	✗	✓
Intensity	high	low
Sparks eliminate emission	✗	✓
Illumination required	✓	✗
Size requirements	✗	(✓) determines E-field

Table 5.1 Comparison between TSL and SPEL

## 5.2 Conclusion and Outlook

We have developed a novel experimental setup to measure smooth pyroelectric luminescence in pyroelectric crystals, including a rotating capacitor to measure the electric field in a contact-free way within a vacuum cryostat. We propose three emission models of traps under the effect of temperature and electric fields, two of which are derived from the Poole-Frenkel model, while the third one is based on Fowler-Nordheim Tunneling. With the models that we proposed, the activating energy of deep trap levels which are inaccessible by pure thermal stimulation can be determined.

With the intensities ranging between 10<sup>2</sup> and 10<sup>5</sup> counts per second, pyroelectric luminescence yields a relatively weak signal. For this reason, photon counters like the PMT are required, which do not allow measuring the wavelength of this emission. The signal is too low for typical spectrometers. In principle, repeating the same measurement with different wavelength filters could be a way to obtain the wavelengths. This could provide insight about the respective recombination processes, and is left to future research.

Our investigation has demonstrated some crucial results about the studied samples, including a model description that yields quantitative information about the trap. However, we assumed what is commonly known as first-order luminescence, which means that there occurs no substantial replenishing of traps during the emission. However, since we found that crystals show luminescence even without illumination, a certain intrinsic regeneration of filled traps can be deduced. The development of a second- or higher-order model is thus an important pointer for future studies.

In conclusion, despite of similarities between TSL and SPEL, we find the following differences between the two: SPEL occurs without previous photo-excitation, so mechanisms to replenish the exhausted traps are suspected. The effect of the electric field on traps can be large enough to generate SPEL under cooling. The rate constants for the emission appear to be very high, since a stop in heating rapidly diminishes any emission. We also see a clear slowing or even reversal of the electric field buildup during the heating of a pyroelectric when the emission takes place. This clearly indicates that the released trapped charges contribute a significant dark current.

Future studies based on BaTiO<sub>3</sub> nanoparticles could help circumvent the problem of crystal fracture, however the measurement of electric field is not directly possible in this approach.

Additional research options include the calculation of resistivity change due to the emitted charge carriers, as well as the density of the latter from the total amount of captured light.

Measuring the emitted wavelengths could allow to gain more insight about the transitions within the electronic structure of the material. Since our lamp only provided 365-nm, a proper activation of the crystals was not possible. Signals of higher quality could be obtained when more traps can be occupied before starting the experiment.

The bulk limited conduction mechanisms like Poole–Frenkel, the trap level, trap spacing, trap density, carrier drift mobility, the dielectric relaxation time and the density of states of the conduction band in the dielectric films can be determined [67].

## 6 REFERENCES

- [1] L. Liang, X. Kang, Y. Sang, and H. Liu, "One-dimensional ferroelectric nanostructures: Synthesis, properties, and applications," *Advanced Science*, vol. 3, no. 7. Wiley-VCH Verlag, 2016.
- [2] K. S. V. Nambi, S. M. D. Rao, and M. P. Chougaonkar, "Luminescence and field emission associated with heating and cooling of pyroelectric materials: Pyroelectroluminescence," *Nuclear Tracks and Radiation Measurements* (1982), vol. 10, no. 1–2, pp. 243–247, Jan. 1985.
- [3] K. Kerimov and A. Suleimanov, "Effect of Electric Field Strength on the Intensity Distribution of Electrostimulated Thermoluminescence of Polyethylene," *Physica Status Solidi (a)*, vol. 94, no. 1, pp. K51–K54, 1986.
- [4] K. V. R. Murthy and H. S. Virk, "Luminescence phenomena: An introduction," *Defect and Diffusion Forum*, vol. 347, no. June 2015, pp. 1–34, Jan. 2014.
- [5] J. I. Pankove, *Optical Processes in Semiconductors*. Dover, New York: Dover Publications, Inc., 1975.
- [6] D. N. Nikogosyan, "Beta barium borate (BBO) - A review of its properties and applications," *Applied Physics A Solids and Surfaces*, vol. 52, no. 6. Springer-Verlag, pp. 359–368, Jun-1991.
- [7] R. S. Weis and T. K. Gaylord, "Lithium niobate: Summary of physical properties and crystal structure," *Applied Physics A Solids and Surfaces*, vol. 37, no. 4, pp. 191–203, Aug. 1985.
- [8] A. Almirall *et al.*, "High-frequency surface acoustic wave devices based on epitaxial Z-LiNbO<sub>3</sub> layers on sapphire," *Applied Physics Letters*, vol. 114, no. 16, p. 162905, Apr. 2019.

- [9] M. Acosta *et al.*, “BaTiO<sub>3</sub>-based piezoelectrics: Fundamentals, current status, and perspectives,” *Applied Physics Reviews*, vol. 4, no. 4. American Institute of Physics Inc., p. 41305, 01-Dec-2017.
- [10] I. C. Amaechi, A. Hadj Youssef, D. Rawach, J. P. Claverie, S. Sun, and A. Ruediger, “Ferroelectric Fe-Cr Codoped BaTiO<sub>3</sub> Nanoparticles for the Photocatalytic Oxidation of Azo Dyes,” *ACS Applied Nano Materials*, vol. 2, no. 5, pp. 2890–2901, May 2019.
- [11] S. Pandya *et al.*, “Pyroelectric energy conversion with large energy and power density in relaxor ferroelectric thin films,” *Nature Materials*, vol. 17, no. 5, pp. 432–438, May 2018.
- [12] G. Sebald, D. Guyomar, and A. Agbossou, “On thermoelectric and pyroelectric energy harvesting,” *Smart Materials and Structures*, vol. 18, no. 12, p. 125006, Sep. 2009.
- [13] G. Sebald, S. Pruvost, and D. Guyomar, “Energy harvesting based on Ericsson pyroelectric cycles in a relaxor ferroelectric ceramic,” *Smart Materials and Structures*, vol. 17, no. 1, p. 15012, Dec. 2007.
- [14] M. H. Lee, R. Guo, and A. S. Bhalla, “Pyroelectric sensors,” *Journal of Electroceramics*, vol. 2, no. 4, pp. 229–242, 1998.
- [15] A. J. Holden, “Pyroelectric sensor arrays for detection and thermal imaging,” in *Infrared Technology and Applications XXXIX*, 2013, vol. 8704, pp. 483–492.
- [16] I. C. Amaechi, R. Katoch, G. Kolhatkar, S. Sun, and A. Ruediger, “Particle size effect on the photocatalytic kinetics of barium titanate powders,” *Catalysis Science and Technology*, vol. 10, no. 18, pp. 6274–6284, Sep. 2020.
- [17] B. Jaffe, W. R. C. Jr., and H. Jaffe, *Piezoelectric Ceramics*, 1st ed. London and New York: Academic Press, 1971.

- [18] J. H. Robertson, *Physical properties of crystals: their representation by tensors and matrices by J. F. Nye*, vol. 41, no. 6. Clarendon Press, 1985.
- [19] D. A. Zabek, "Pyroelectric Structures and Devices for Thermal Energy Harvesting," University of Bath, 2016.
- [20] E. Defaÿ, *Integration of Ferroelectric and Piezoelectric Thin Films: Concepts and Applications for Microsystems*. Wiley-ISTE, 2013.
- [21] C. Wan and C. R. Bowen, "Multiscale-structuring of polyvinylidene fluoride for energy harvesting: the impact of molecular-, micro- and macro-structure," *Journal of Materials Chemistry A*, vol. 5, no. 7. Royal Society of Chemistry, pp. 3091–3128, 14-Feb-2017.
- [22] S. B. Lang, "Pyroelectricity: From ancient curiosity to modern imaging tool," *Physics Today*, vol. 58, no. 8, pp. 31–36, Aug. 2005.
- [23] R. W. Whatmore, "Pyroelectric devices and materials," *Reports on Progress in Physics*, vol. 49, no. 12. pp. 1335–1386, 1986.
- [24] C. R. Bowen, J. Taylor, E. Leboulbar, D. Zabek, A. Chauhan, and R. Vaish, "Pyroelectric materials and devices for energy harvesting applications," *Energy and Environmental Science*, vol. 7, no. 12, pp. 3836–3856, 2014.
- [25] K. M. Rabe, M. Dawber, C. Lichtensteiger, C. H. Ahn, and J. M. Triscone, "Modern physics of ferroelectrics: Essential background," *Topics in Applied Physics*, vol. 105, pp. 1–30, 2007.
- [26] M. Dawber, K. M. Rabe, and J. F. Scott, "Physics of thin-film ferroelectric oxides," *Reviews of Modern Physics*, vol. 77, no. 4, pp. 1083–1130, Oct. 2005.
- [27] M. E. Lines and A. M. Glass, *Principles and Applications of Ferroelectrics and Related Materials*. Oxford: Clarendon Press, 1977.

- [28] A. S. Sidorkin, *Domain Structure in Ferroelectrics and Related Materials*. Cambridge, United Kingdom: Cambridge International Science Publishing, 2006.
- [29] J. Valasek, "Piezo-electric and allied phenomena in Rochelle salt," *Physical Review*, vol. 17, no. 4, pp. 475–481, 1921.
- [30] F. Pockels, *On the effect of an electrostatic field on the optical behavior of piezoelectric crystals*. Abh. Gott, 1894.
- [31] H. Mueller, "Properties of Rochelle salt," *Physical Review*, vol. 57, no. 9, pp. 829–839, 1940.
- [32] J. C. Slater, "Theory of the transition in KH<sub>2</sub>PO<sub>4</sub>," *The Journal of Chemical Physics*, vol. 9, no. 1, pp. 16–33, 1941.
- [33] A. von Hippel, R. G. Breckenridge, F. G. Chesley, and L. Tisza, "High dielectric constant ceramics," *Industrial & Engineering Chemistry*, vol. 38, no. 11, pp. 1097–1109, Nov. 1946.
- [34] G. Schmidt and J. Petersson, "Über die Lichtemission von ferroelektrischen Triglyzinsulfatkristallen," *Zeitschrift für Naturforschung A*, vol. 24, no. 10, pp. 1559–1562, Oct. 1969.
- [35] H. P. Yockey and C. L. Aseltine, "Development of high voltages in potassium dihydrogen phosphate irradiated by gamma rays," *Physical Review B*, vol. 11, no. 11, pp. 4373–4382, Jun. 1975.
- [36] D. W. Cooke and C. Alexander, "Observations of intense scintillations in unirradiated glycine," *Physical Review B*, vol. 14, no. 3, pp. 1333–1335, Aug. 1976.
- [37] K. S. V Nambi, "Pyroelectroluminescence induced by tourmaline," *Physica Status Solidi (a)*, vol. 82, no. 1, pp. K71–K73, Mar. 1984.

- [38] K. A. Mirza, P. D. Townsend, and G. L. Destefanis, "Light emission from the surface of LiNbO<sub>3</sub>," *Physica Status Solidi (a)*, vol. 47, no. 1, pp. K63–K66, May 1978.
- [39] I. Tale, V. Tale, and J. Rosa, "The field fluctuational model of thermally stimulated processes in ferroelectric LiNbO<sub>3</sub>," *Solid State Communications*, vol. 48, no. 2, pp. 135–137, Oct. 1983.
- [40] S. L. Bravina, A. K. Kadashchuk, N. V. Morozovsky, N. I. Ostapenko, and Y. A. Skryshevsky, "Pyroelectric luminescence of ferroelectric-semiconductors proustite and pyrargyrite in the temperature range 4.2–300 K," *Ferroelectrics*, vol. 83, no. 1, pp. 119–125, Jan. 1988.
- [41] J. S. Patel and D. M. Hanson, "Pyroelectric Luminescence From Ionic Compounds," *Ferroelectrics*, vol. 38, no. 1, pp. 923–924, Oct. 1981.
- [42] J. Kalinowski and Z. Dreger, "Simple model for pyroelectric luminescence," *Physical Review B*, vol. 36, no. 15, pp. 7840–7848, Nov. 1987.
- [43] J. S. Patel and D. M. Hanson, "Pyroelectric luminescence," *Nature*, vol. 293, no. 5832, pp. 445–447, Oct. 1981.
- [44] M. C. C. Nelson, D. M. M. Hanson, and J. S. S. Patel, "The phenomenon of pyroelectric luminescence," *Chemical Physics*, vol. 116, no. 3, pp. 311–318, Sep. 1987.
- [45] A. J. J. Bos, "Thermoluminescence as a research tool to investigate luminescence mechanisms," *Materials*, vol. 10, no. 12, 2017.
- [46] M. Martini and F. Meinardi, "Thermally stimulated luminescence: New perspectives in the study of defects in solids," *Rivista del Nuovo Cimento della Società Italiana di Fisica*, vol. 20, no. 8, pp. 1–71, Apr. 1997.
- [47] E. Mihóková and M. Nikl, "Luminescent materials: Probing the excited state of

emission centers by spectroscopic methods," *Measurement Science and Technology*, vol. 26, no. 1. Institute of Physics Publishing, p. 012001, 01-Jan-2015.

- [48] D. Eimerl, L. Davis, S. Velsko, E. K. Graham, and A. Zalkin, "Optical, mechanical, and thermal properties of barium borate," *Journal of Applied Physics*, vol. 62, no. 5, pp. 1968–1983, Sep. 1987.
- [49] Q. Tan *et al.*, "Defects in  $\beta$ -BaB<sub>2</sub>O<sub>4</sub> (BBO) crystals observed by laser scanning tomography," *Journal of Crystal Growth*, vol. 141, no. 3–4, pp. 393–398, Aug. 1994.
- [50] D. A. Keszler, "Borates for optical frequency conversion," *Current Opinion in Solid State and Materials Science*, vol. 1, no. 2, pp. 204–211, Apr. 1996.
- [51] V. D. Antsygin *et al.*, "Origin of near-ultraviolet absorption of nonlinear BBO crystals," in *Seventh International Symposium on Laser Metrology Applied to Science, Industry, and Everyday Life*, 2002, vol. 4900, pp. 599–605.
- [52] M. Swaisi, A. Dörfler, R. Katoch, and A. Ruediger, "Smooth pyroelectric luminescence in LiNbO<sub>3</sub> single crystals," *Journal of Physics Condensed Matter*, vol. 32, no. 29, p. 295701, Apr. 2020.
- [53] R. Singh, J. Kaur, P. Bose, R. Shrivastava, V. Dubey, and Y. Parganiha, "Intense visible light emission from dysprosium (Dy<sup>3+</sup>) doped barium titanate (BaTiO<sub>3</sub>) phosphor and its thermoluminescence study," *Journal of Materials Science: Materials in Electronics*, vol. 28, no. 18, pp. 13690–13697, Sep. 2017.
- [54] A. J. J. Bos, "Theory of thermoluminescence," *Radiation Measurements*, vol. 41, no. SUPPL. 1, pp. 45–56, 2006.
- [55] A. Ruediger, O. F. Schirmer, A. K. Kadashchuk, and Y. A. Skryshevskii, "Pyroelectric luminescence via internal Poole-Frenkel effect," *Europhysics Letters*, vol. 57, no. 4, pp. 592–596, Feb. 2002.

- [56] D. W. Kim, E. M. Bourim, S. H. Jeong, and I. K. Yoo, "Pyroelectric electron emissions and domain inversion of LiNbO<sub>3</sub> single crystals," *Physica B: Condensed Matter*, vol. 352, no. 1–4, pp. 200–205, 2004.
- [57] V. T. Adamiv, Y. V. Burak, M. R. Panasyuk, and I. M. Teslyuk, "Pyroelectroluminescence of barium beta borate single crystals," *Technical Physics Letters*, vol. 24, no. 2, pp. 150–151, 1998.
- [58] Y. Furukawa *et al.*, "Correlation of MgO-doped near-stoichiometric LiNbO<sub>3</sub> composition to the defect structure," *Journal of Crystal Growth*, 2000.
- [59] R. Lisiecki, B. Macalik, R. Kowalski, J. Komar, and R.-R. Witold, "Effect of Temperature on Luminescence of LiNbO<sub>3</sub> Crystals Single-Doped with Sm<sup>3+</sup>, Tb<sup>3+</sup>, or Dy<sup>3+</sup> Ions," *Crystals*, vol. 10, no. 1034, p. 15, 2020.
- [60] A. A. Plokhikh, C. D. Kim, G. T. Joo, R. K. Route, and R. S. Feigelson, "Domain structure and electrical properties of beta-BaB<sub>2</sub>O<sub>4</sub> single crystals grown by direct Czochralski method," in *9th International Meeting on Ferroelectricity*, 1998, pp. 1231–S1233.
- [61] R. Guo and A. S. Bhalla, "Pyroelectric, piezoelectric, and dielectric properties of β-BaB<sub>2</sub>O<sub>4</sub> single crystal," *Journal of Applied Physics*, vol. 66, no. 12, pp. 6186–6188, 1989.
- [62] S. Pradhan and G. S. Roy, "Study the Crystal Structure and Phase Transition of BaTiO<sub>3</sub> – A Pervoskite," *Researcher*, vol. 55, no. 33, pp. 63–67, 2013.
- [63] M. Aguilar, "Thermoluminescence of BaTiO<sub>3</sub> crystals," *Journal of Physics C: Solid State Physics*, vol. 15, no. 17, pp. 3829–3839, 1982.
- [64] A. Y. Fasasi, F. A. Balogun, M. K. Fasasi, P. O. Ogunleye, C. E. Mokobia, and E. P. Inyang, "Thermoluminescence properties of barium titanate prepared by solid-state reaction," *Sensors and Actuators, A: Physical*, vol. 135, no. 2, pp. 598–604, Apr. 2007.

- [65] G. Godefroy *et al.*, "Electroluminescence in ferroelectric BaTiO<sub>3</sub>," *Ferroelectrics*, vol. 29, no. 1, pp. 135–144, Aug. 1980.
- [66] A. Gruverman *et al.*, "Tunneling electroresistance effect in ferroelectric tunnel junctions at the nanoscale," *Nano Letters*, vol. 9, no. 10, pp. 3539–3543, 2009.
- [67] F. C. Chiu, "A review on conduction mechanisms in dielectric films," *Advances in Materials Science and Engineering*, vol. 2014, p. 18, 2014.
- [68] V. Garcia and M. Bibes, "Ferroelectric tunnel junctions for information storage and processing," *Nature Communications*, vol. 5, pp. 1–12, 2014.
- [69] D. Pantel and M. Alexe, "Electroresistance effects in ferroelectric tunnel barriers," *Physical Review B - Condensed Matter and Materials Physics*, vol. 82, no. 13, p. 134105, 2010.
- [70] J. G. Simmons, "Poole-Frenkel effect and Schottky effect in metal-insulator-metal systems," *Physical Review*, vol. 155, no. 3, pp. 657–660, Mar. 1967.
- [71] R. Massarczyk *et al.*, "Paschen's law studies in cold gases," Institute of Physics Publishing, Jun. 2017.
- [72] P. Carazzetti, "Electrical breakdown at low pressure for planar microelectromechanical systems with 10- 500-um gaps," *Journal of Micro/Nanolithography, MEMS, and MOEMS*, vol. 8, no. 3, p. 031305, 2009.
- [73] F. Paschen, "Ueber die zum Funkenübergang in Luft, Wasserstoff und Kohlensäure bei verschiedenen Drucken erforderliche Potentialdifferenz," *Annalen der Physik*, vol. 273, no. 5, pp. 69–96, Jan. 1889.
- [74] M. A. Lieberman and A. J. Lichtenberg, *Principles of Plasma Discharges and Materials Processing: Second Edition*, 2nd ed. Hoboken, N.J: Wiley-Interscience,

2005.

- [75] A. M. García-Campaña and W. R. G. Baeyens, "Principles and recent analytical applications of chemiluminescence," *Analisis*, vol. 28, no. 8. Wiley-VCH Verlag, pp. 686–698, 2000.
- [76] A. Feng and P. F. Smet, "A review of mechanoluminescence in inorganic solids: Compounds, mechanisms, models and applications," *Materials*, vol. 11, no. 4, Mar. 2018.
- [77] T. Kerst, R. Malmbeck, N. L. Lal Banik, and J. Toivonen, "Alpha radiation-induced luminescence by am-241 in aqueous nitric acid solution," *Sensors (Switzerland)*, vol. 19, no. 7, Apr. 2019.
- [78] J. I. Zink and B. P. Chandra, "Light emission during growth and destruction of crystals. Crystalloluminescence and triboluminescence," *Journal of Physical Chemistry*, vol. 86, no. 1, pp. 5–7, 1982.
- [79] H. K. Henisch, "Electroluminescence," *Reports on Progress in Physics*, vol. 27, no. 1, pp. 369–405, Jan. 1964.
- [80] T. Unold and L. Gütay, "Photoluminescence Analysis of Thin-Film Solar Cells," in *Advanced Characterization Techniques for Thin Film Solar Cells*, vol. 1–2, Weinheim, Germany: Wiley-VCH Verlag GmbH & Co. KGaA, 2016, pp. 275–297.
- [81] W. M. Ranjith, "THERMOLUMINESCENCE DATING OF SEDIMENTS," 1982.
- [82] S. W. S. McKeever, *Thermoluminescence of Solids*. Cambridge University Press, 1985.
- [83] M. Bakr and M. Omer, "Determination of Thermoluminescence Kinetic," *Materials*, vol. 13, no. 1047, pp. 1–23, 2020.

- [84] R. Chen and S. W. S. McKeever, *Theory of Thermoluminescence and Related Phenomena*. World Scientific, 1997.
- [85] M. Fox, *Optical Properties of Solids*, 2nd ed. Oxford University Press, 2010.
- [86] Z. Wang, H. Yu, and H. Su, “The transport properties of oxygen vacancy-related polaron-like bound state in  $\text{HfO}_x$ ,” *Scientific Reports*, vol. 3, no. 1, pp. 1–6, Dec. 2013.
- [87] F. Chevy, “Bose Polarons that Strongly Interact,” *Physics*, vol. 9, Jul. 2016.
- [88] C. Merschjann, D. Berben, M. Imlau, and M. Wöhlecke, “Evidence for two-path recombination of photoinduced small polarons in reduced  $\text{LiNbO}_3$ ,” *Physical Review Letters*, vol. 96, no. 18, p. 186404, 2006.
- [89] O. F. Schirmer, M. Imlau, C. Merschjann, and B. Schoke, “Electron small polarons and bipolarons in  $\text{LiNbO}_3$ ,” *Journal of Physics Condensed Matter*, vol. 21, no. 123201, p. 29pp, 2009.
- [90] R. L. Frank, E. H. Lieb, and R. Seiringer, “Symmetry of Bipolaron Bound States for Small Coulomb Repulsion,” *Communications in Mathematical Physics*, vol. 319, no. 2, pp. 557–573, Apr. 2013.
- [91] O. F. Schirmer, “Holes bound as small polarons to acceptor defects in oxide materials: Why are their thermal ionization energies so high?,” *Journal of Physics Condensed Matter*, vol. 23, no. 33, 2011.
- [92] D. Emin, “Phonon-assisted transition rates I. Optical-phonon-assisted hopping in solids,” *Advances in Physics*, vol. 24, no. 3, pp. 305–348, Jan. 1975.
- [93] D. Emin, *Polarons*, vol. 9780521519. Cambridge University Press, 2010.

- [94] S. Messerschmidt *et al.*, “The role of self-trapped excitons in polaronic recombination processes in lithium niobate,” *Journal of Physics Condensed Matter*, vol. 31, no. 6, p. 065701, Feb. 2019.
- [95] A. J. J. Bos, T. M. Piters, J. M. Gomez Ros, and A. Delgado, “An intercomparison of glow curve analysis computer programs: I; Synthetic glow curves,” in *Radiation Protection Dosimetry*, 1993, vol. 47, no. 1–4, pp. 473–477.
- [96] J. Peng *et al.*, “tgcd: An R package for analyzing thermoluminescence glow curves.” R Project, 2020.
- [97] R Core Team, “R: A Language and Environment for Statistical Computing.” Vienna, Austria, 2020.
- [98] J. Furlan, “Tunnelling generation–recombination currents in a-Si junctions,” *Progress in Quantum Electronics*, vol. 25, no. 2, pp. 55–96, May 2001.
- [99] J. Frenkel, “On pre-breakdown phenomena in insulators and electronic semiconductors,” *Physical Review*, vol. 54, no. 8. American Physical Society, pp. 647–648, 15-Oct-1938.
- [100] P. A. Martin, B. G. Streetman, and K. Hess, “Electric field enhanced emission from non-Coulombic traps in semiconductors,” *Journal of Applied Physics*, vol. 52, no. 12, pp. 7409–7415, Dec. 1981.
- [101] J. Furlan, Ž. Gorup, A. Levstek, and S. Amon, “Thermally assisted tunneling and the Poole-Frenkel effect in homogenous a-Si,” *Journal of Applied Physics*, 2003.
- [102] J. Furlan, “Tunnelling generation-recombination currents in a-Si junctions,” *Progress in Quantum Electronics*, vol. 25, no. 2, pp. 55–96, 2001.
- [103] G. Vincent, A. Chantre, and D. Bois, “Electric field effect on the thermal emission of traps in semiconductor junctions,” *Journal of Applied Physics*, vol. 50, no. 8, p.

5484, 1979.

- [104] M. Swaisi, R. Katoch, A. Dörfler, and A. Ruediger, “(under review) Smooth pyroelectric luminescence in  $\beta$ -barium borate ( $\text{BaB}_2\text{O}_4$ ) single crystals via Fowler Nordheim tunneling,” *Europhysics Letters (EPL)*, 2021.
- [105] Q. Peng and R. E. Cohen, “Origin of pyroelectricity in  $\text{LiNbO}_3$ ,” *Physical Review B - Condensed Matter and Materials Physics*, 2011.
- [106] S. Sanna and W. G. Schmidt, “ $\text{LiNbO}_3$  surfaces from a microscopic perspective,” *Journal of Physics Condensed Matter*. 2017.
- [107] T. Volk and M. Wöhlecke, *Lithium niobate: Defects, photorefraction and ferroelectric switching*, 1st ed., vol. 115. Springer, 2009.
- [108] S. C. Abrahams, H. J. Levinstein, and J. M. Reddy, “Ferroelectric lithium niobate. 5. Polycrystal X-ray diffraction study between  $24^\circ$  and  $1200^\circ\text{C}$ ,” *Journal of Physics and Chemistry of Solids*, 1966.
- [109] C. Thierfelder, S. Sanna, A. Schindlmayr, and W. G. Schmidt, “Do we know the band gap of lithium niobate?,” *physica status solidi (c)*, vol. 7, no. 2, pp. 362–365, Feb. 2010.
- [110] K. L. Sweeney and L. E. Halliburton, “Oxygen vacancies in lithium niobate,” *Applied Physics Letters*, vol. 43, no. 4, pp. 336–338, 1983.
- [111] N. Zotov, H. Boysen, F. Frey, T. Metzger, and E. Born, “Cation substitution models of congruent  $\text{LiNbO}_3$  investigated by X-ray and neutron powder diffraction,” *Journal of Physics and Chemistry of Solids*, vol. 55, no. 2, pp. 145–152, 1994.
- [112] A. P. Wilkinson, A. K. Cheetham, and R. H. Jarman, “The defect structure of congruently melting lithium niobate,” *Journal of Applied Physics*, 1993.

- [113] J. Shi, H. Fritze, G. Borchardt, and K. D. Becker, "Defect chemistry, redox kinetics, and chemical diffusion of lithium deficient lithium niobate," *Physical Chemistry Chemical Physics*, 2011.
- [114] H. Donnerberg, S. M. Tomlinson, C. R. A. Catlow, and O. F. Schirmer, "Computer-simulation studies of intrinsic defects in LiNbO<sub>3</sub> crystals," *Physical Review B*, vol. 40, no. 17, pp. 11909–11916, Dec. 1989.
- [115] A. Zylbersztein, "Thermally activated trapping in Fe-doped LiNbO<sub>3</sub>," *Applied Physics Letters*, 1976.
- [116] D. McMillen, T. Hudson, J. Wagner, and J. Singleton, "Holographic recording in specially doped lithium niobate crystals," *Optics Express*, 1998.
- [117] P. I. MacFarlane, K. Holliday, J. F. H. Nicholls, and B. Henderson, "Characterization of Cr<sup>3+</sup> centres in LiNbO<sub>3</sub> using fluorescence line narrowing," *Journal of Physics: Condensed Matter*, 1995.
- [118] G. E. Peterson, M. Glass, A. Carnevale, and P. M. Bridenbaugh, "Control of Laser Damage in LiNbO<sub>3</sub>," *Journal of the American Ceramic Society*, vol. 56, no. 5, pp. 278–282, May 1973.
- [119] P. Günter and J. P. Huignard, *Photorefractive Materials and Their Applications 1*, 1st ed., vol. 113. 2006.
- [120] M. Kösters, B. Sturman, P. Werheit, D. Haertle, and K. Buse, "Optical cleaning of congruent lithium niobate crystals," *Nature Photonics*, vol. 3, no. 9, pp. 510–513, Sep. 2009.
- [121] M. Imlau, H. Badorreck, and C. Merschjann, "Optical nonlinearities of small polarons in lithium niobate," *Applied Physics Reviews*, vol. 2, no. 4, 2015.
- [122] K. Nassau, H. J. Levinstein, and G. M. Loiacono, "Ferroelectric lithium niobate. 1.

Growth, domain structure, dislocations and etching," *Journal of Physics and Chemistry of Solids*, vol. 27, no. 6–7, pp. 983–988, 1966.

- [123] Judith Renate Marie-Luise Schwesyg, "Interaction of light with impurities in lithium niobate crystals," *Rheinischen Friedrich-Wilhelms-Universität Bonn*, 2011.
- [124] J. R. Carruthers, G. E. Peterson, M. Grasso, and P. M. Bridenbaugh, "Nonstoichiometry and crystal growth of lithium niobate," *Journal of Applied Physics*, vol. 42, no. 5, pp. 1846–1851, Apr. 1971.
- [125] R. Bhatt *et al.*, "Control of Intrinsic Defects in Lithium Niobate Single Crystal for Optoelectronic Applications," *Crystals*, vol. 7, no. 2, p. 23, Jan. 2017.
- [126] E. G. Tsvetkov, "Some reasons for the formation of grain boundaries and melt inclusions in growing large BBO crystals by TSSG technique," *Journal of Crystal Growth*, vol. 297, no. 1, pp. 259–263, Dec. 2006.
- [127] V. Trnovcová, P. P. Fedorov, A. E. Kokh, and I. Furár, "Electrical and dielectric properties of  $\beta$ -BaB<sub>2</sub>O<sub>4</sub> (BBO) and CsLiB<sub>6</sub>O<sub>10</sub> (CLBO) crystals," *Journal of Physics and Chemistry of Solids*, vol. 68, no. 5–6, pp. 1024–1028, May 2007.
- [128] W. Hong, L. E. Halliburton, D. Perlov, K. T. Stevens, R. K. Route, and R. S. Feigelson, "Observation of paramagnetic point defects in BBO ( $\beta$ -BaB<sub>2</sub>O<sub>4</sub>) crystals," *Optical Materials*, vol. 26, no. 4, pp. 437–441, 2004.
- [129] A. E. Kokh, N.G. Kononova, T.B. Bekker, and Yu. F. Kargin, "BaO-BaB<sub>2</sub>O<sub>4</sub> phase diagram," *Russian Journal of Inorganic Chemistry*, vol. 50, no. 11, pp. 1749–1753, Nov. 2005.
- [130] A. R. Lim and I. G. Kim, "Correlation between NMR and nonlinear optical properties at boron sites in nonlinear optical  $\beta$ -BaB<sub>2</sub>O<sub>4</sub> single crystals," *Solid State Communications*, vol. 159, no. September 2018, pp. 41–44, 2013.

- [131] Y.-N. Xu and W. Y. Ching, "Electronic, optical, and structural properties of some wurtzite crystals," *Physical Review B*, vol. 48, no. 7, 1993.
- [132] S. D. Ganichev, E. Ziemann, W. Prettl, I. N. Yassievich, A. A. Istratov, and E. R. Weber, "Distinction between the Poole-Frenkel and tunneling models of electric-field-stimulated carrier emission from deep levels in semiconductors," *Physical Review B*, vol. 61, no. 15, pp. 10361–10365, Apr. 2000.
- [133] A. Bahouka, "Comparaison des propriétés optiques de beta-BBO obtenu par croissance TSSG et par tirage Czochralski en vue d'optimiser la génération de rayonnement UV," Université de Metz, 2006.
- [134] R. Tazaki, D. Fu, M. Itoh, M. Daimon, and S. Y. Koshihara, "Lattice distortion under an electric field in BaTiO<sub>3</sub> piezoelectric single crystal," *Journal of Physics Condensed Matter*, vol. 21, no. 21, 2009.
- [135] D. T. Margulies, F. T. Parker, and A. E. Berkowitz, "Magnetic anomalies in single crystal Fe<sub>3</sub>O<sub>4</sub> thin films," *Journal of Applied Physics*, vol. 75, no. 10, pp. 6097–6099, Aug. 1994.
- [136] M. Itoh, R. Wang, Y. Inaguma, T. Yamaguchi, Y. J. Shan, and T. Nakamura, "Ferroelectricity induced by oxygen isotope exchange in strontium titanate perovskite," *Physical Review Letters*, vol. 82, no. 17, pp. 3540–3543, Apr. 1999.
- [137] A. S. Bhalla, R. Guo, and R. Roy, "The perovskite structure - A review of its role in ceramic science and technology," *Materials Research Innovations*, vol. 4, no. 1. Springer New York, pp. 3–26, 2000.
- [138] W. D. Kingery, H. K. Bowen, and D. R. Uhlmann, *Introduction to ceramics*. New York: Wiley, 1976.
- [139] G. Philippot, C. Elissalde, M. Maglione, and C. Aymonier, "Supercritical fluid technology: A reliable process for high quality BaTiO<sub>3</sub> based nanomaterials," *Advanced Powder Technology*, vol. 25, no. 5, pp. 1415–1429, Sep. 2014.

- [140] D. Rytz, B. A. Wechsler, M. H. Garrett, C. C. Nelson, and R. N. Schwartz, "Photorefractive properties of BaTiO<sub>3</sub>:Co," *Journal of the Optical Society of America B*, vol. 7, no. 12, p. 2245, Dec. 1990.
- [141] M. G. Clark, F. J. Disalvo, A. M. Glass, and G. E. Peterson, "Electronic structure and optical index damage of iron-doped lithium niobate," *The Journal of Chemical Physics*, vol. 59, pp. 6209–6219, 1973.
- [142] K. Suzuki and K. Kijima, "Optical band gap of barium titanate nanoparticles prepared by RF-plasma chemical vapor deposition," *Japanese Journal of Applied Physics, Part 1: Regular Papers and Short Notes and Review Papers*, vol. 44, no. 4 A, pp. 2081–2082, 2005.
- [143] Hamamatsu Photonics K.K., "Photon Counting Head H8259 Series - H8259-01." 2019.
- [144] M. M. Chirila *et al.*, "Thermoluminescence study of stoichiometric LiNbO<sub>3</sub> crystals," *Journal of Applied Physics*, vol. 92, no. 3, pp. 1221–1226, 2002.
- [145] V. Kisand, R. Kink, M. Kink, J. Maksimov, M. Kirm, and I. Martinson, "Low temperature optical spectroscopy of nonlinear BBO crystals," *Physica Scripta*, vol. 54, no. 5, pp. 542–544, 1996.
- [146] J. Furlan, Z. Gorup, A. Levstek, and S. Amon, "Thermally assisted tunneling and the Poole–Frenkel effect in homogenous a-Si," *Journal of Applied Physics*, vol. 94, no. 12, p. 7604, May 2003.
- [147] G. Kitis, J. M. Gomez-Ros, and J. W. N. Tuyn, "Thermoluminescence glow-curve deconvolution functions for first, second and general orders of kinetics," *Journal of Physics D: Applied Physics*, vol. 31, no. 19, pp. 2636–2641, Oct. 1998.
- [148] S. Kim, V. Gopalan, and A. Gruverman, "Coercive fields in ferroelectrics: A case study in lithium niobate and lithium tantalate," *Applied Physics Letters*, vol. 80, no.

15, pp. 2740–2742, 2002.

- [149] A. Prokhorov and Y. S. Kuz'minov, *Physics and Chemistry of Lithium Niobate*. Adam Hilger, 1990.
- [150] Y. Yang, D. Psaltis, M. Luennemann, D. Berben, U. Hartwig, and K. Buse, "Photorefractive properties of lithium niobate crystals doped with manganese," *Journal of the Optical Society of America B*, vol. 20, no. 7, p. 1491, 2003.
- [151] H. Kurz *et al.*, "Photorefractive centers in LiNbO<sub>3</sub>, studied by optical-, Mössbauer- and EPR-methods," *Applied Physics*, vol. 12, no. 4, pp. 355–368, 1977.
- [152] R. L. Byer, "Quasi-phasematched nonlinear interactions and devices," *Journal of Nonlinear Optical Physics and Materials*, vol. 6, no. 4, pp. 549–592, 1997.
- [153] D. A. Roberts and G. C. Catella, "Simplified characterization of nonlinear optical crystals: A plea for standardization of nomenclature and conventions," *Conference Proceedings - Lasers and Electro-Optics Society Annual Meeting-LEOS*, vol. 11, p. 51, 1997.
- [154] M. Yamada, N. Nada, M. Saitoh, and K. Watanabe, "First-order quasi-phase matched LiNbO<sub>3</sub> waveguide periodically poled by applying an external field for efficient blue second-harmonic generation," *Applied Physics Letters*, vol. 62, no. 5, pp. 435–436, 1993.
- [155] G. D. Miller, R. G. Batchko, W. M. Tulloch, D. R. Weise, M. M. Fejer, and R. L. Byer, "42%-Efficient Single-Pass Cw Second-Harmonic Generation in Periodically Poled Lithium Niobate," *Optics Letters*, vol. 22, no. 24, p. 1834, Dec. 1997.
- [156] T. Bartholomäus, K. Buse, C. Deuper, and E. Krätzig, "Pyroelectric coefficients of LiNbO<sub>3</sub> crystals of different compositions," *Physica Status Solidi (a)*, vol. 142, no. 1, pp. K55–K57, Jun. 1994.

- [157] P. Marton, I. Rychetsky, and J. Hlinka, “Domain walls of ferroelectric BaTiO<sub>3</sub> within the Ginzburg-Landau-Devonshire phenomenological model,” *Physical Review B - Condensed Matter and Materials Physics*, vol. 81, no. 14, Apr. 2010.
- [158] B. Ertuğ, “The Overview of The Electrical Properties of Barium Titanate,” *American Journal of Engineering Research*, vol. 2, no. 08, pp. 1–7, 2013.
- [159] B. Naranjo, J. K. Gimzewski, and S. Putterman, “Observation of nuclear fusion driven by a pyroelectric crystal,” *Nature*, vol. 434, no. 7037, pp. 1115–1117, Apr. 2005.

## APPENDIX

### A.1 Theory of regeneration of trapped states without UV

The mechanism is based on two metastable states with a slow singlet-triplet transition. Analog to the phosphorescence mechanism, this slow transition keeps replenishing the emitting trap shown in Figure A.2.

#### A.1.1 Jablonski Diagram of Phosphorescence

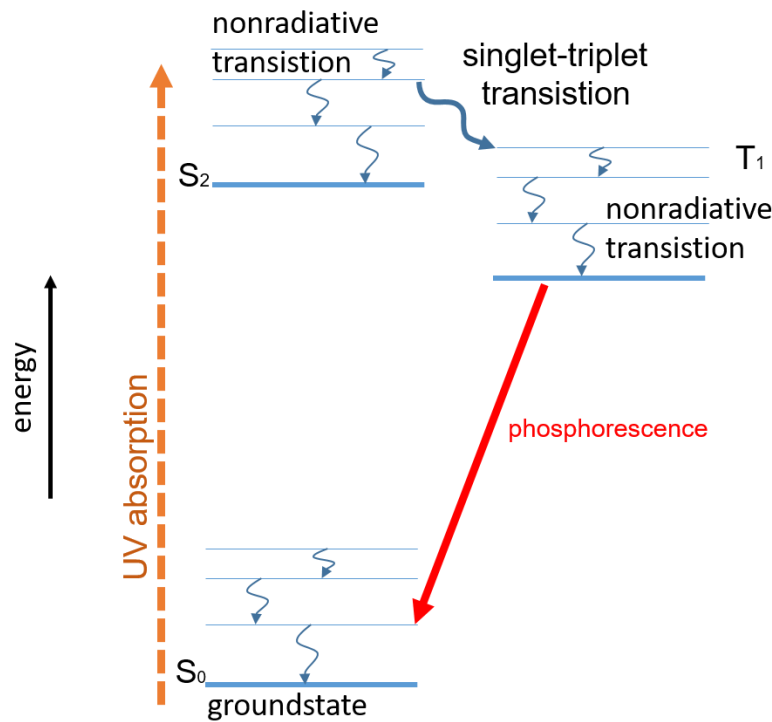


**Figure A.1** Energy diagram of the phosphorescence process. The excited singlet states  $S_2$  relax by the singlet-triplet transition. This process is temperature-dependent and can require exponentially long timescales[4], meaning that the emission of light continues without illumination.

### A.1.2 Hypothetical model of regenerating traps

The Jablonski Diagram (Figure A.1) visualizes the process of radiative decay from an excited triplet state back to a singlet state, also known as phosphorescence. This process is typically temperature sensitive, while fluorescence is a singlet-singlet transition which is typically non-temperature dependent.

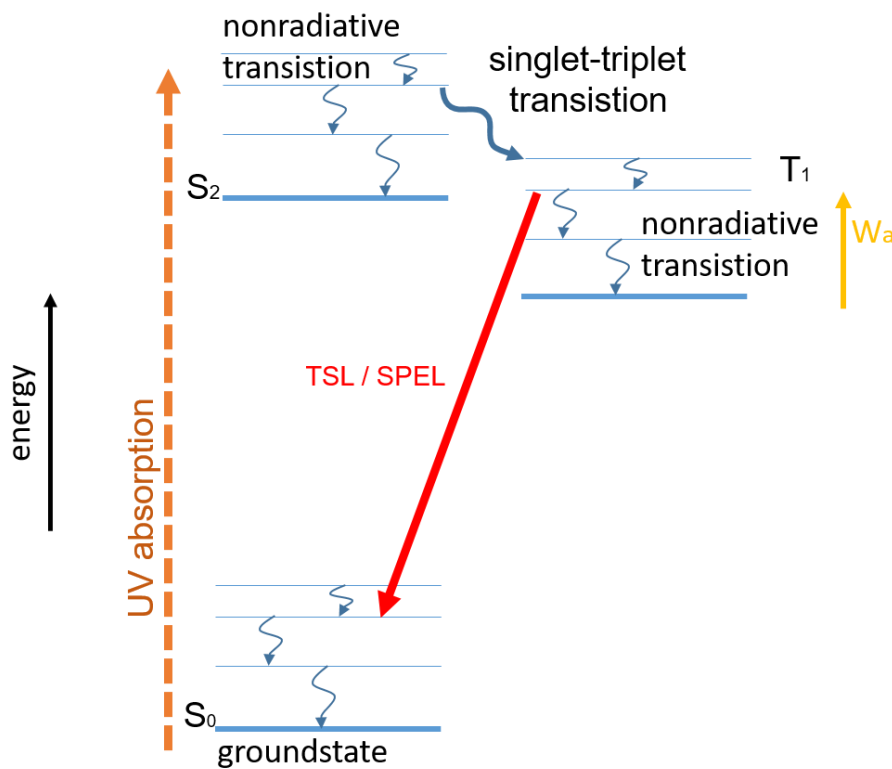


**Figure A.2** Proposed mechanism for the regeneration of trapped states. A relatively slow singlet-triplet transition continually keeps replenishing the trap that can then be released by thermal or pyroelectric stimulation. This allows TSL / SPEL to be detected during multiple heating and cooling cycles without renewed UV illumination.

## A.2 Derivation of Trap Depletion by Arrhenius' law

The Arrhenius law assumes that the rate of change is constant and proportional to the ratio of thermal activating energy  $k_B T$  and energy barrier  $W_a$ . The temperature is assumed constant as well.

$$\frac{\partial N}{\partial t} = \text{const} = -N(t) c \frac{W_a}{k_B T} \quad (\text{A.1})$$

The differential equation is solved by separation of variables and subsequent integration

$$\int_{t_0}^t \frac{\partial N}{\partial t} / N(t) dt = - \int_{t_0}^t c \frac{W_a}{k_B T} dt \quad (\text{A.2})$$

The integration rule of the derivative over its antiderivative yields the logarithm

$$\log \frac{N(t)}{N(t_0)} = -c \frac{W_a}{k_B T} (t - t_0) \quad (\text{A.3})$$

Solving by  $N(t)$  yields

$$\frac{N(t)}{N(t_0)} = \exp\left(-c \frac{W_a}{k_B T} (t - t_0)\right) = \exp\left(-c \frac{W_a}{k_B T} t + t_0 c \frac{W_a}{k_B T}\right) \quad (\text{A.4})$$

From this, we obtain

$$\frac{N(t)}{N(t_0)} = \exp\left(-c \frac{W_a}{k_B T} (t - t_0)\right) = \exp\left(-c \frac{W_a}{k_B T} t\right) \underbrace{\exp\left(t_0 c \frac{W_a}{k_B T}\right)}_{constant=C} \quad (\text{A.5})$$

Which yields

$$\frac{N(t)}{N(t_0)} = C \exp\left(-c \frac{W_a}{k_B T} t\right) \quad (\text{A.6})$$

### A.3 Estimation of conductivity as observed by the emission rate

The electric field due to the change in temperature is

$$E_{ideal} = \frac{\beta \gamma}{\epsilon_0 \epsilon_r} \Delta t \quad (\text{A.7})$$

If we estimate the amount of emitted charges from traps from the isotropic radiation on a sphere, we obtain a total emission of

$$I_{total} = \frac{4\pi r^2}{A_{PMT} q_{eff}} I \quad (\text{A.8})$$

Subtracting this amount of charges yields a drop in electric field to

$$E_{real} = \frac{\beta \gamma - I_{total} q}{\epsilon_0 \epsilon_r} \Delta t \quad (\text{A.9})$$

For the maximum values in LiNbO<sub>3</sub>, of  $\gamma = 38 \text{ E-6 C/K/m}^2$ ,  $\epsilon_r = 4.2$ ,  $A_{PMT} = (2\text{mm})^2$ , the efficiency of transmission through the window and on the sensor  $q_{eff} = 0.05$ , the distance between crystal and PMT sensor  $r = 0.2 \text{ m}$ , a peak intensity  $I = 5\text{E}5 \text{ Hz}$ , and a heating rate of  $\beta = 0.2 \text{ K/s}$ .

We obtain approximately a two percent drop in electric field

$$\frac{E_{real}}{E_{ideal}} = 97\%$$

Thus, the observed amount of released traps is insufficient to explain a significant drop in the electric field.

#### A.4 Trap-based conduction mechanisms (schematic)

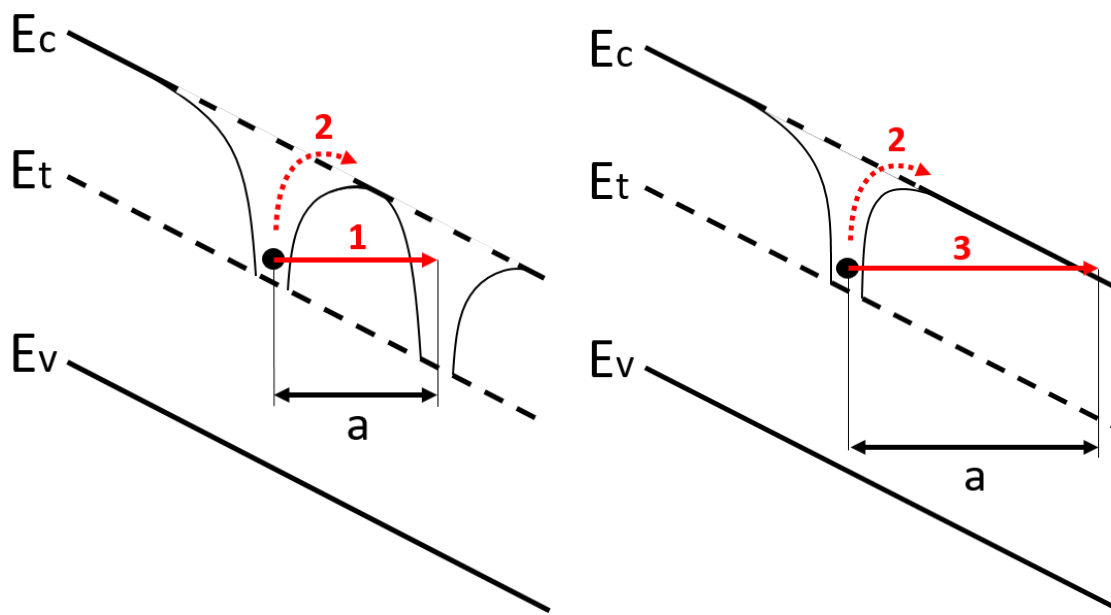


**Figure A.3** Trap conduction mechanisms (schematic). Left diagram, 1: Hopping tunneling and 2: Poole-Frenkel effect. The hopping mechanism depends mainly on tunneling distance  $a$ , while the Poole-Frenkel mechanism depends highly on the electric field and temperature. Right diagram, 3: At lower trap density, only tunneling to the conduction band is possible. This is a Fowler-Nordheim-type barrier where the tunneling distance changes with the applied electric field.

## A.5 General Order Thermoluminescence

Using the general order kinetic glow peak model from Kitis et al. [147], we fit the luminescence curves of LiNbO<sub>3</sub>, BaB<sub>2</sub>O<sub>4</sub> and BaTiO<sub>3</sub>. The fitting is performed using the tgcd software package [96].

The general order equation is [147]

$$I(T) = I_m b^{b/(b-1)} \exp\left(\frac{W_a}{kT} \frac{T - T_m}{T_m}\right) \times \left[ (b-1)(1-\Delta) \frac{T^2}{T_m^2} \exp\left(\frac{W_a}{kT} \frac{T - T_m}{T_m}\right) + Z_m \right]^{-b/(b-1)} \quad (\text{A.10})$$

where  $\Delta = \frac{2kT}{W_a}$ ,  $\Delta_m = \frac{2kT_m}{W_a}$ ,  $Z_m = 1 + (b-1)\Delta_m$  and  $1 < b \leq 2$ . When  $b$  approaches 1, the equation approaches the first order kinetic model. When  $b = 2$ , the model describes second order kinetics, and intermediary values of  $b$  describe mixed variants.

### A.5.1 General Order Fits

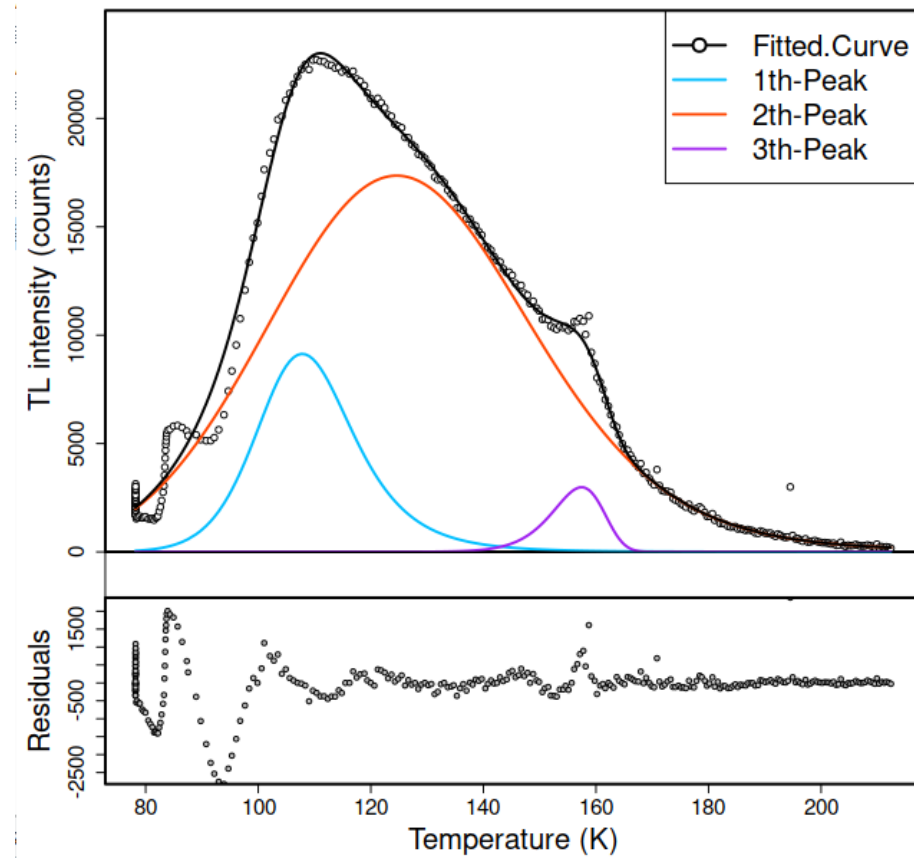


**Figure A.4** LiNbO<sub>3</sub>, general order model

	I (Hz)	Wa (meV)	Tm (K)	b
1st-Peak	9130	157	107.6	2.00
2nd-Peak	16900	53.5	119.6	1.09
3rd-Peak	2980	47.1	157.4	1.06

**Table A.1** Fitting parameters of thermoluminescence model, LiNbO<sub>3</sub>, general order model

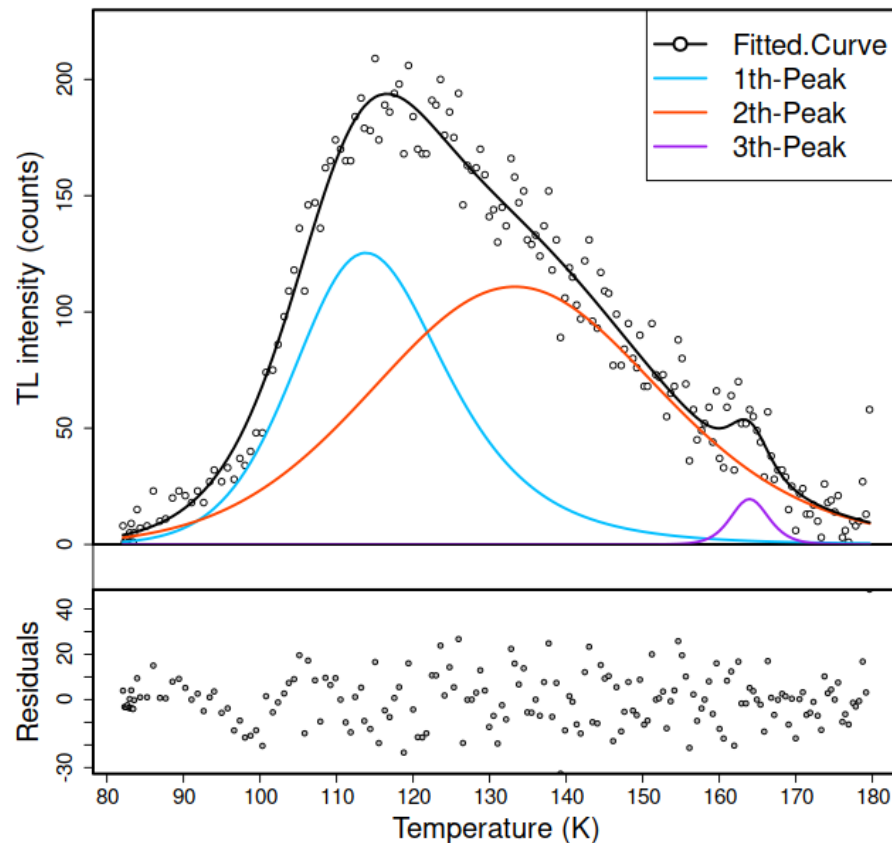


**Figure A.5**  $\text{BaB}_2\text{O}_4$  general order model

	I (Hz)	Wa (meV)	Tm (K)	b
1st-Peak	125	150	113.5	2.00
2nd-Peak	110	83.3	131.2	1.30
3rd-Peak	19.5	1.38	163.9	2.00

**Table A.2** Fitting parameters of thermoluminescence model,  $\text{BaB}_2\text{O}_4$  general order model

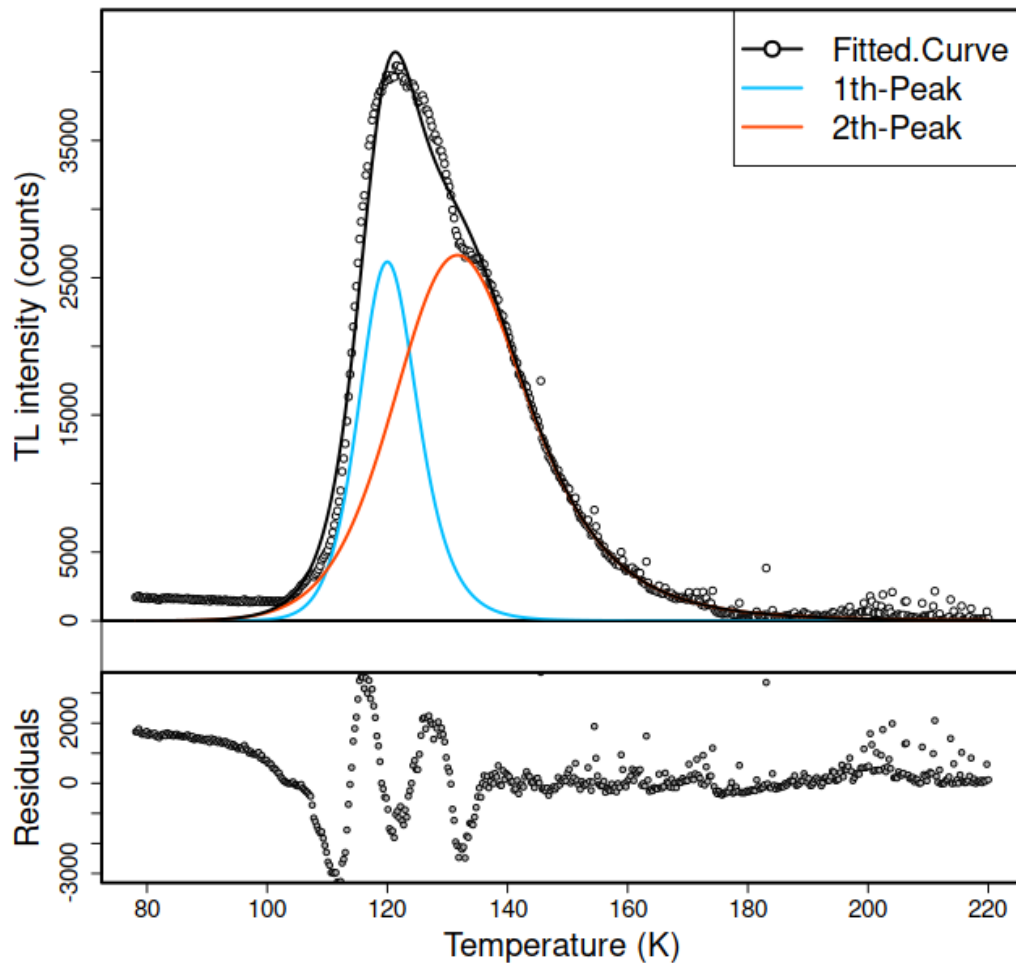


**Figure A.6**  $\text{BaTiO}_3$ , general order model

	I (Hz)	Wa (meV)	Tm (K)	b
1st-Peak	26200	359	120.0	2.00
2nd-Peak	26600	178	131.4	2.00

**Table A.3** Fitting parameters of thermoluminescence model,  $\text{BaTiO}_3$ , general order model

## A.6 Pyroelectric Luminescence of BaTiO<sub>3</sub>

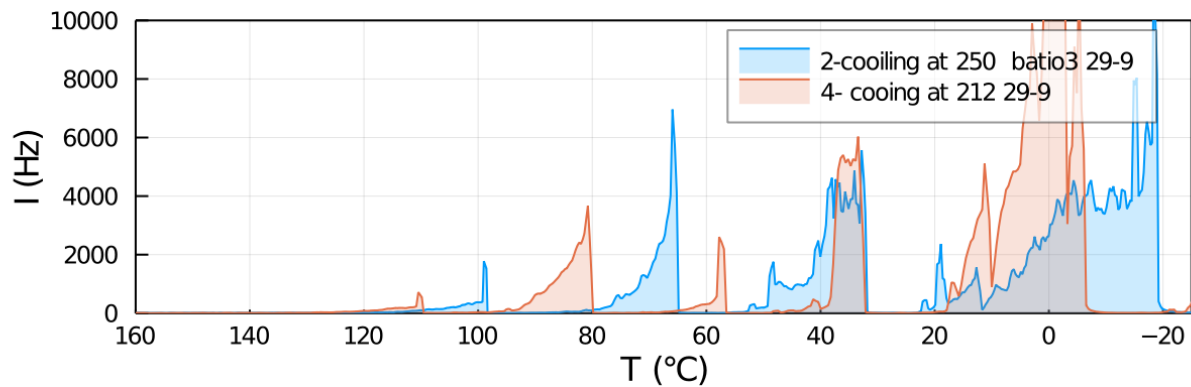


**Figure A.7** Pyroelectric Luminescence, cooling of BaTiO<sub>3</sub> between 160 °C to -20 °C.

# Sommaire Récapitulatif

## **Luminescence pyroélectrique continue dans le niobate de lithium, le beta borate de baryum et le titanate de baryum**

Les phénomènes d'interaction de matériaux et de lumière ont depuis toujours été utilisés pour la caractérisation des propriétés de matériaux. Parmi l'absorption et la diffusion, les phénomènes de luminescence, qui résument l'émission de lumière par une conversion d'énergie au sein du matériau, sont les méthodes les plus exploités. Concernant la luminescence, il y une façon commune de distinguer l'origine de l'énergie permettant l'émission d'un ou de plusieurs photons pour catégoriser les effets. Parmi les différentes manifestations de la luminescence, celle qui converti un photon incident à un photon émis (typiquement à moindre énergie suite à de différents mécanismes de perte d'énergie) et connue comme photoluminescence. Selon la durée de vie de l'état excité ou autrement dit, selon la nature de la transition (permise, interdite ou même doublement interdite), on peut également distinguer entre la photoluminescence et p.ex. la phosphorescence. De nombreux autres mécanismes ont été identifiés pour la génération d'une luminescence comme p.ex. la chimiluminescence (lucioles etc.), l'électroluminescence (jonction *pn* dans une DEL etc.), la cathodoluminescence suite à un bombardement par électrons. Dans cette thèse, je vais me préoccuper d'un nouveau phénomène surnommé « luminescence pyroélectrique » et qui fait sujet d'un nombre important de publications depuis les premiers rapports il y a environ 50 ans. Mais même si Patel et Hanson [43] ont cherché à donner une approche plus systématique dans leur publication dans Nature en 1987, il y a un très grand défi quant à la compréhension ce qui est à l'origine de ce phénomène.

## 1 INTRODUCTION

La luminescence pyroélectrique décrit alors l'émission de lumière dans un matériau pyroélectrique. La pyroélectricité décrit la formation d'un champ électrique sous variation de température et n'existe que dans des matériaux polaires. Ceci mérite une description plus systématique pour comprendre la relation entre la structure et les propriétés électrostatiques d'un matériau. Si nous nous intéressons à l'existence d'un ordre polaire dans un matériau, on peut partir de l'idée d'un dipôle à l'échelle moléculaire ou d'une polarisation diélectrique à l'échelle macroscopique. La polarisation diélectrique n'est que l'intégrale volumique de tous les dipôles dans un volume donné. La polarisation diélectrique peut pourtant exister pour des raisons différentes:

1. Un champ électrique extérieur induit un dipôle (ceci est médié par la susceptibilité diélectrique). Plus que la polarisabilité (à l'échelle moléculaire) ou la susceptibilité diélectrique (dans le monde macroscopique) est élevée, plus le dipôle induit par le champ électrique sera important. Il s'agit d'une propriété universelle qui existe dans tous les matériaux. Étant représenté par un tenseur de deuxième rang, il n'y a aucune restriction concernant l'existence d'une polarisabilité ou d'une susceptibilité diélectrique. Clairement, l'existence d'un dipôle brise la symétrie mais cette réduction de la symétrie d'inversion est induite par le champ électrique extérieur. Pour comprendre cet argument en détail, il faut s'intéresser aux groupes de point ou au classes cristallins. Pour l'instant, il suffit de retenir que toutes les classes cristallines (32/32) sont susceptibles à la formation d'un dipôle sous l'application d'un champ électrique.
2. Dans les matériaux qui n'ont pas de centre d'inversion (ceci s'applique à 21/32 des classes cristallins) il y a 20 qui sont connus comme piézoélectriques. Dérivé du grecque, la piézoélectricité décrit la formation d'un dipôle ou d'une polarisation diélectrique sous un stress extérieur. Pour qu'un matériau soit piézoélectrique, il suffit que le centre d'inversion du cristal soit absent. Sous un stress externe, le centre de gravitation des charges positives se déplace autrement que le centre de

gravitation des charges négatives ce qui donne un dipôle ou bien une polarisation diélectrique.

3. Si nous regardons maintenant un autre sous-groupe des matériaux piézoélectrique et que nous exigeons la présence d'un dipôle permanent ou d'une polarisation permanente (aussi connue comme une polarisation rémanente), nous faisons face aux 11 groupes polaires. Comme cette polarisation est toujours présente tant que la structure cristalline ne change pas (elle changera uniquement lors d'une transition de phase) on s'intéresse surtout à comment cette polarisation change lors d'un changement de température. Ce phénomène est appelé pyroélectricité, basé sur le mot grecque pour le feu, mais l'appellation n'est pas exacte. Le terme pyro- suggère que le changement de polarisation diélectrique se produit uniquement lors d'un échauffement mais l'effet fonctionne aussi bien lors d'un échauffement que lors d'un refroidissement. Il est important à noter qu'une transition de phase va souvent changer à la fois l'ampleur et l'orientation de la polarisation permanente ou, lors d'une transition polaire, la polarisation peut être complètement supprimée. Ce genre de transition est décrite par une théorie thermodynamique développée par Landau-Ginzburg-Devonshire (LGD) et provoque un changement abrupt quand la température s'approche de la température de transition de phase qui est identique avec la température de Curie pour une transition de deuxième ordre et possiblement différent de quelques Kelvins lors d'une transition de premier ordre. Ce qui en suit en tout cas, est que les changements de la polarisation permanente en proximité d'une transition de phase sont toujours beaucoup plus importants que quand la température est loin d'une transition de phase. Plus exactement, le comportement est décrit par la loi de Curie-Weiss.

Nous allons nous intéresser uniquement à des matériaux cristallins pour la suite de cette thèse. L'ordre cristallin renforce l'ordre polaire car la périodicité exige à ce que tous les dipôles soient orientés dans la même direction dans une zone précise que l'on appelle un domaine polaire (ou aussi un domaine ferroélectrique). La polarisation peut p.ex. être antiparallèle dans un autre domaine ou être placé à un angle précis qui est dicté par les paramètres de maille de la cellule cristalline.

Comme nous l'avons indiqué dans la section 3) ci-dessus, il y a un intérêt particulier d'analyser des matériaux avec une multitude de transitions de phases dans la gamme de température accessible par l'expérience. On peut s'attendre à des phénomènes plus riches et plus importants que pour un matériau sans transitions de phase en proximité.

Dans le cadre de cette thèse, nous avons choisi trois matériaux différents : a) le titanate de baryum qui a plusieurs transitions de phase entre 80K et 500K, les températures accessibles par notre cryostat b) le niobate de lithium sous sa forme congruent avec une seule transition de phase bien au-dessus de 1000K et c) le beta-baryum borate qui dispose d'une bande interdite très importante comparé aux autres matériaux de cette thèse ce qui aura une importance qu'on soulignera plus tard.

## 1.1 La luminescence thermiquement stimulée

Pour revenir au phénomène de la luminescence pyroélectrique, on peut alors s'attendre à un phénomène qui existe sous changement de température et ceci et pour un échauffement et pour un refroidissement. C'est le moment de présenter la luminescence thermiquement stimulée, aussi connu sous son acronyme TSL ('thermally stimulated luminescence' en anglais). Cette luminescence existe dans les conditions suivantes : un échantillon quelconque (sans nécessité d'être pyro-, ou piézoélectrique)

- est refroidi à basse température (« basse température » sera synonyme avec « température cryogène » dans le cadre de cette thèse) et
- exposé à une source d'illumination. Cette source est choisie de sorte qu'elle puisse efficacement exciter des capteurs de charge vers des états excités. Dans un cristal parfait, on pourrait s'attendre à ce que la seule transition possible soit vers la bande de conduction pour les électrons ou vers la bande de valence pour les trous. J'aimerais constater que je vais uniquement discuter le cas d'électrons lors de ma thèse sans limitation à la validité de mes arguments pour le cas respectif de trous et leur excitation vers la bande de valence. Ceci implique même la discussion de

polarons dans le cas du niobate de lithium qui existent théoriquement aussi bien pour les électrons que pour les trous. Une fois que les électrons se trouvent dans la bande de conduction, ils vont recombiner avec les trous restant dans la bande de valence sous émission d'un photon de l'énergie exacte de la bande directe du matériau. À ce moment, nous faisons le constat que cette photoexcitation est difficile, voire impossible à accomplir d'une manière homogène à travers le matériau. La photoexcitation nécessite une absorption qui provoque une intensité décroissante à travers l'échantillon selon la loi de Lambert-Beer. Donc, si on utilise une source de lumière qui est fortement absorbée et qui facilite la photoexcitation, cette efficacité est limitée à une très faible profondeur de pénétration de la lumière dans l'échantillon qui est inversement proportionnel au coefficient d'absorption. Si nous partons de l'idée d'un cristal non-ideal qui contient des défauts comme p.ex. des lacunes, des substitutions, des interstices ou des défauts d'une plus grande dimensionnalité (dislocations etc.), la photoexcitation peut se passer de deux manières différentes. Comme dans le premier cas, il y a l'excitation des électrons vers la bande de conduction mais au lieu de recomburer directement vers la bande de valence, les électrons peuvent maintenant recomburer vers les défauts qui ne contiennent pas encore d'électron. L'autre option est la photoexcitation directe de la bande de valence vers les défauts, un phénomène qui est très bien connu grâce aux bandes d'absorption supplémentaires introduites par des défauts cristallins. Donc, il est fort probable que ces défauts ou certains parmi ces défauts seront remplis d'électrons suite à une photoexcitation avec une source de lumière dont les photons disposent d'une énergie suffisante pour les atteindre.

- Imaginons maintenant que nous sommes à température zéro Kelvin de sorte que les électrons qui se trouvent dans ces défauts sont efficacement piégés dans le potentiel de ces défauts. Les potentiels peuvent être très complexes et dans le cadre de cette thèse, nous allons nous contenter des deux cas d'un potentiel Coulombique ou d'un potentiel de Dirac (rectangulaire) pour évaluer l'importance du choix de cette approximation. Mais quelque soit la forme du potentiel à zéro Kelvin, aucun électron pourrait d'en évader à cause d'un manque d'énergie. Les électrons cherchent à s'en évader avec une fréquence de tentative qui correspond à des fréquences des phonons optiques dans ces matériaux mais pour y réussir, il faut prendre en considération un coefficient de probabilité de pouvoir surmonter

la barrière énergétique. Avec une distribution d'énergie thermique donnée par leur nature de fermions, donc une distribution de Fermi-Dirac, les électrons vont connaître une probabilité très faible de dépasser un certain seuil. Ce traitement probabilistique de dépasser une énergie d'activation amène directement à la loi d'Arrhenius qui démontre qu'il faut une certaine énergie pour que le taux d'électrons qui arrivent à s'évader d'un potentiel avec une profondeur  $W_A$  devienne détectable.

La luminescence thermiquement stimulée est donc basée sur l'ionisation thermique d'électrons piégés dans des défauts cristallins (souvent appelés « pièges » dans ce contexte) dès que la température atteint une certaine valeur lors d'un échauffement. Il est très important de constater que ce phénomène ne se produit que lors d'un échauffement car les pièges seront irréversiblement vidés à température élevée de sorte que lors d'un refroidissement il n'y a plus d'électrons à ioniser. La luminescence thermiquement stimulée est particulièrement utile car elle permet d'extraire les valeurs des énergies d'ionisation thermique des pièges ce qui est un paramètre très pertinent pour p.ex. l'industrie des semiconducteurs. La valeur de l'ionisation thermique peut être très différent de la valeur pour l'ionisation optique car cette dernière doit respecter les préservations du moment angulaire ce qui est d'ailleurs l'origine du concept de Frank-Condon. Pour remonter à l'énergie d'activation, on suit la procédure décrite ci-dessus avec un échauffement à taux constant. Le taux de changement de température est dénommé  $\beta$  à travers cette thèse. Quand la température atteint le seuil que l'activation thermique devient détectable, l'intensité de la luminescence thermiquement stimulée augmente selon la loi d'Arrhenius jusqu'à ce que l'épuisement des électrons de ce défaut se fait remarquer ce qui amène finalement à une décroissance du signal. La position du maximum n'a pas de signification mais c'est à travers un fit numérique selon la loi d'Arrhenius que l'on peut extraire l'énergie d'activation qui se trouve typiquement à quelques dizaines ou quelques centaines de meV.

## 1.2 La luminescence pyroélectrique

Un autre phénomène s'ajoute à ce qui est décrit dans la section précédente lors d'une expérience avec un matériau pyroélectrique. Lors d'un changement de température, un matériau pyroélectrique génère un champ électrique. La raison est un changement de la polarisation permanente qui peut être exprimée selon le théorème de Gauss par une densité de charge de surface (nota bene que les unités de la polarisation diélectrique sont C/m<sup>2</sup>). Il revient à Patel et Hanson d'avoir remarqué que *a*) un certain type de luminescence n'existe que dans des matériaux pyroélectriques (comme le tourmaline) et que *b*) ce type de luminescence changeait en fonction de la pression atmosphérique. Plus précisément, Patel et Hanson ont établi trois types de luminescence pyroélectrique qu'ils ont observé pour des pressions atmosphériques standard, pour des pressions autour d'un millibar et pour des pressions encore inférieures à cette valeur. Leurs observations se résument comme suit :

- luminescence pyroélectrique de type 1 : à pression atmosphérique, un cristal pyroélectrique émet une luminescence en forme d'éclairs qui sont espacés de quelques Kelvins en fonction du taux de changement de température.
- luminescence pyroélectrique de type 2 : à une pression autour d'un millibar, les éclairs deviennent plus fréquents et moins intenses et on observe une faible émission continue, mais qui n'est pas constante pendant le changement de température.
- luminescence pyroélectrique de type 3 : à des pressions substantiellement inférieures à un millibar, les éclairs disparaissent et l'émission continue devient légèrement plus prononcée et démontre clairement qu'elle existe préférentiellement dans certaines gammes de température. Ceci est reproductible et démontre une certaine similitude avec la luminescence thermiquement stimulée bien que la luminescence pyroélectrique de type 3 existe aussi pour un refroidissement.

Déjà dans la publication de Patel et Hanson, les auteurs émettent l'hypothèse que la luminescence pyroélectrique de type 3 pourrait être associée à des défauts cristallins mais la très faible intensité ne permettait pas d'obtenir une information sur la distribution spectrale de cette émission.

Il est pourtant surprenant que les auteurs n'aient pas fait le constat que la luminescence pyroélectrique de type 2 avait à la fois les caractéristiques du type 1 (les éclairs) et du type 3 (émission continue) et qu'il pourrait possiblement s'agir d'une superposition des deux.

Concernant la luminescence pyroélectrique de type 1, la publication de Kalinowski et Dreger [42] a établi un modèle qui décrit les observations quantitativement correctement.

Ils décrivent l'évolution du champ électrique causé par les charges de surface par l'équation suivante :

$$\frac{dE}{dt} = \frac{\gamma_P \beta}{\chi(T)\epsilon_0} - \frac{\sigma E}{\epsilon_r(T)\epsilon_0}$$

où  $E$  est le champ pyroélectrique,  $t$  dénote le temps depuis le début du changement de température avec un taux constant de  $\beta$ ;  $\gamma_P$  est le coefficient pyroélectrique,  $\epsilon_0$  la permittivité diélectrique du vide,  $\epsilon_r(T)$  est la permittivité relative du matériau,  $\chi(T)$  est la susceptibilité diélectrique du matériau et  $\sigma$  est la conductivité électrique. Pour les propriétés représentées par des tenseurs, il faut considérer les éléments respectifs le

long de la direction de l'axe polaire. Tous les paramètres de matériau ainsi que le taux de changement de température sont principalement des fonctions de la température qui elle-même est paramétrisée par le temps et le taux de changement de température. En considérant ces implications, l'équation différentielle décrivant l'évolution du champ pyroélectrique ci-dessus, n'aura plus de solution analytique tandis qu'en gardant les paramètres constants (cette approximation ne peut se justifier que loin de transitions de phase, pour un changement de température constant et dans une gamme de température dans laquelle le changement de conductivité est négligeable). Pour ce cas, la solution de cette équation est :

$$E(t) = \frac{\gamma_p \beta}{\sigma} \left( 1 - \exp \left( -\frac{\sigma}{\epsilon_r \epsilon_0} t \right) \right)$$

si on considère que la valeur initiale soit zéro champ électrique au début de l'expérience. Cette solution décrit une courbe de saturation qui démarre quasiment linéaire avec la proportionnalité  $\frac{\gamma_p \beta}{\sigma}$ . Ceci veut dire que le champ électrique évolue particulièrement bien pour un matériau avec un fort coefficient pyroélectrique, un taux de changement de température élevé et une faible conductivité. Avec le temps, les contributions des fuites deviennent de plus en plus importantes de sorte que la courbe sature vers un limes pour lequel le côté gauche de l'équation différentielle devient zéro (stagnation) ce qui donne le champ de saturation à  $\frac{\gamma_p \beta}{\sigma}$ . En principe, ce champ électrique maximal que l'on peut atteindre est principalement dicté par des paramètres du matériau et le taux de changement de température mais est-ce que cela veut dire qu'on puisse l'atteindre en réalité?

C'est ici que le champ de claquage doit être pris en considération. À pression ambiante avec un taux d'humidité standardisé, on peut s'attendre à des décharges électriques (claquages) au-dessus d'un certain seuil. Cette décharge provoque la formation d'un plasma dans l'atmosphère ambiante qui est principalement composé d'azote et d'oxygène et qui porte une signature spectrale très spécifique. Dreger et Kalinowski n'ont pas seulement montré que le spectre des éclairs correspondait parfaitement aux lignes d'émission du gaz de l'atmosphère mais ils ont également pu montrer que chaque claquage causait un court-circuit des charges de surface à travers l'atmosphère (pas du tout à travers le matériau qui a un champ de claquage beaucoup plus élevé que l'atmosphère) et par conséquence, suite à chaque claquage, la densité de charge de surface tombait à une très faible valeur. Autrement dit, le champ pyroélectrique est limité à la fois par l'échantillon et par le champ de claquage de l'atmosphère ambiante.

Ceci explique parfaitement la luminescence pyroélectrique de type 1, mais la nature des types 2 et 3 reste toujours mystérieuse et fera l'objet de cette thèse.

### 1.3 Objectifs de cette thèse

- 1) Identifier la nature de la pyroélectricité de type 2 et 3. Ceci implique l'explication de toutes les observations rapportées dans la littérature à date d'une manière au moins qualitative.
- 2) Vérifier des prédictions de notre modèle expliquant ce qu'on va appeler à partir d'ici la « luminescence pyroélectrique lisse » (type 3)
- 3) Chercher à identifier la nature des pièges dans plusieurs matériaux et estimer la possibilité d'accéder à des défauts « profonds » qui ne sont pas accessibles par la luminescence thermiquement stimulée.

## 2 MÉTHODOLOGIE

Nous utilisons un cryostat optique de Oxford Instrument qui fonctionne sous vide entre 80 K et 500K. Le contact thermique avec l'échantillon est fait à travers un bloc de cuivre sur un côté de l'échantillon. Ceci implique que la température varie à travers l'échantillon lors d'un changement de température sur un côté. La différence de température entre deux côtés d'un échantillon peut être estimée et ne dépasse pas 5 K pour les matériaux et les taux de changement de température que nous utilisons qui sont entre 0.1 K/s et 1 K/s.

La photo-détection se fait par un tube de photomultiplicateur en mode de photon individuel. L'efficacité quantique du capteur est autour de 60% dans la gamme visible et l'angle solide de détection correspond à une aperture numérique d'environ 0,1. Les intensités détectées sont tellement faibles qu'une dispersion spectrale n'est pas pertinente.

Lors de l'échauffement, le changement de température se fait par un contrôleur PID (proportionnel-intégral-différentiel) qui permet de moduler le taux d'échauffement envers l'effet de refroidissement du bain d'azote liquide du cryostat pour atteindre un taux de changement de température positif est constant. Lors du refroidissement, notre système ne permet pas de stabiliser le taux de circulation d'azote de sorte que le changement de température est moins contrôlé que lors de l'échauffement mais malgré cette limitation, les taux ne varient pas plus que typiquement 20% lors d'un cycle.

La détection du champ pyroélectrique se fait par couplage capacitif (pour ne pas vider les surfaces de leurs charges) par une électrode en rotation au-dessus d'une surface polaire du cristal. Les signaux sont transférés en temps réel (temp, température, intensité détectée et champ pyroélectrique) vers un ordinateur par un script de Labview qui nous permet par la suite d'exporter les données vers des logiciels d'analyse de données (p.ex. Origin ou Matlab) et de les analyser numériquement.

Le contact thermique entre les échantillons et le bloc de cuivre se fait par une pâte thermique à base d'oxyde de zinc qui garantit à la fois une bonne conductivité thermique, une adhésion mécanique et une bonne isolation électrique. Cette pâte ne contribue aucunement aux émissions détectées.

## 2.1 Matériaux

### 2.1.1 Titanate de baryum

Le choix pour le titanate de baryum s'est fait à cause de la présence de multiples transitions de phases dans la gamme de températures observée. À chaque transition de phase à température modérée, l'orientation de la polarisation change de la direction (111) dans la phase rhomboédrale vers la direction (110) dans la phase orthorhombique et ensuite vers la direction (100) dans la phase tétragonale qui est présente à température ambiante. Autour de 120 degrés Celsius, la dernière transition de phase vers la structure cubique fait disparaître la polarisation permanente. En principe, si notre théorie est correcte, on devrait s'attendre à une émission prononcée à chaque transition de phase qui fait augmenter le coefficient pyroélectrique. La bande interdite est de 3.2 eV. Les échantillons que nous avons utilisés sont des produits commerciaux et nominalement sans défauts. Ceci dit, il est connu que le titanate de barium n'a pas de solution congruente de sorte que chaque monocristal a des gradients de la concentration de lacunes d'oxygène lors de sa croissance. Il y a un autre défi pour ce matériau : Comme la transition de phase de la structure tétragonale vers la structure orthorhombique à 7 degrés Celsius lors d'un refroidissement affecte aussi la distribution des domaines ferroélastique, il est fort probable que le cristal déchire lors de ce refroidissement ce qui détruit l'échantillon progressivement.

### 2.1.2 Niobate de lithium

Le niobate de lithium est très bien connu comme matériau pour l'optique non-linéaire, pour la génération de radiation THz ou pour l'holographie. Le matériau a deux particularités qui le rendent intéressant pour notre étude. Premièrement, la composition congruente du cristal n'est pas la composition stoichiométrique ce qui fait qu'il y a beaucoup plus de  $\text{Nb}^{5+}$  dans le cristal que de  $\text{Li}^+$  ce qui nécessite une compensation de charge par des lacunes d'oxygène. Deuxièmement, la seule transition de phase connue dans ce matériau est au-dessus de 1000K, donc très loin de ce qu'on peut atteindre dans nos expériences. Contrairement au titanate de baryum, les paramètres de ce matériau devraient plutôt rester constants dans la gamme de température observée dans cette thèse. La bande interdite est de 3.7 eV, donc légèrement plus grande que celle du titanate de baryum.

### 2.1.3 Beta-baryum borate

Nous avons choisi ce matériau pour deux raisons : premièrement, ce matériau a récemment attiré beaucoup d'attention comme remplacement du niobate de lithium dans les applications de doublement de fréquence (génération de seconde harmonique) et comme la bande interdite est de 6.4 eV, il est donc quasiment impossible de remplir les pièges par une excitation à travers la bande interdite. S'il y a une excitation et une capture d'électrons, il faudrait qu'elle se fasse à travers une absorption directe par les défauts.

## 3 RÉSULTATS

Pour ce qui est le premier objectif et la question si p.ex. la luminescence pyroélectrique de type 2 est une simple conséquence des éclairs, il faut faire un constat important : la

pyroélectricité de type 3 disparaît tout de suite après une décharge électrique. Si l'hypothèse était correcte que le type 3 est une conséquence du type 1, que l'éclair qui contient beaucoup d'UV génère une photoluminescence qui par la suite est détectée comme type 3, on devrait pourtant s'attendre à ce que a) l'intensité des éclairs soit beaucoup plus élevée que l'intensité de type 3 et que b) l'émission de type 3 suit un éclair ce qui n'est pas du tout le cas! Comme indiqué avant, l'émission de type 3 cède après chaque éclair ce qui indique plutôt que la présence du champ pyroélectrique est requise pour ce genre d'émission.

Si c'est le cas, quel est le rôle de la pression atmosphérique? La réponse est dans la loi de Paschen qui décrit l'évolution du champ de claquage en fonction de la pression atmosphérique pour une distance entre deux électrodes (les surfaces polaires du cristal) donnée.

- pour une pression atmosphérique et plus élevée, le champ de claquage est assez important et provient d'une compétition entre l'accélération des électrons libres et des ions omniprésents dans ce champ électrique et leurs collisions pour le parcours libre moyen. Si le parcours libre moyen est faible à cause de la présence de beaucoup d'atomes ou de molécules de gaz, les ions vont perdre leur énergie assez facilement lors d'une collision et que très rarement atteindre le seuil nécessaire pour ioniser un atome lors d'une collision. Si cette ionisation se produit, on déclenche pourtant une réaction de chaîne car chaque collision génère davantage d'électrons qui à leurs tours seront accélérés et pourront participer à la prochaine collision inélastique et ionisante. Le seuil de claquage est donc relativement élevé et il faut un champ électrique élevé pour provoquer un claquage qui décharge une grande quantité d'énergie dans une événement assez intense.
- pour une pression autour d'un millibar (c'est environ la pression à l'intérieur des tubes à néon), la situation change dramatiquement car le parcours libre moyen entre deux collisions augmente de sorte qu'il est plus facile d'accumuler de l'énergie cinétique entre deux collisions qui deviennent plus facilement inélastiques et ionisantes. Les claquages deviennent donc plus fréquents (plus d'éclairs comme décrit dans l'introduction) mais moins intense (aussi en accord avec les observations de Patel et Hanson).

- pour des pressions inférieures à 1 millibar, la situation s'inverse à nouveau et bien que l'énergie cinétique entre deux collisions augmente, ces collisions deviennent de moins en moins probables car notre gaz atmosphérique devient de plus en plus dilué en s'approchant de l'approximation du gaz idéal. À ce moment, le champ de claquage augmente très rapidement et bien au-dessus du seuil de la pression atmosphérique ambiante car il n'y a quasiment plus de possibilité de former un plasma lors d'une décharge. Les pressions de nos expériences sont de l'ordre de  $10^{-5}$  mbar et causent un champ de claquage qui est tellement élevée que nous n'observons plus de claquages du tout.

Cette réflexion explique déjà l'observation pourquoi les éclairs deviennent plus fréquents mais moins intenses quand on baisse la pression atmosphérique vers 1 mbar. La question se pose maintenant d'où provient l'émission de type 3. Qu'est-ce qui pourrait se passer dans un cristal ou plus précisément avec les défauts dans un cristal quand on fait face à un champ électrique très important (au-dessus de 10 MV/m)? Ceci nous amène aux phénomènes d'ionisation de défauts par champ électrique et en analogie des phénomènes d'une interface, où on a l'émission Schottky et l'effet d'émission de champ, la même chose peut se produire pour les potentiels d'un défaut. Si le porteur de charge doit dépasser l'énergie d'activation baissé par le champ électrique, c'est l'effet Poole-Frenkel, tandis que l'effet tunnel à travers la barrière est connu comme l'effet tunnel Fowler-Nordheim. Les deux phénomènes se passent tellement vite que les phonons du cristal ne sont pas couplés, la mobilité des électrons, la petite distance à traverser le champ électrique énorme assurent que le processus est très rapide.

L'effet Poole-Frenkel ne peut se produire que dans une petite gamme de valeurs du champ électrique : si le champ électrique est trop faible, la déformation du potentiel du défaut ne suffit pas pour libérer les charges et si le champ devient assez important pour l'effet tunnel Fowler-Nordheim, ceci sera dominant.

Nous avons pu constater pour les trois matériaux qu'à basse pression, l'émission de type 3 est dominante. Par conséquence, toujours lié à l'objectif 1, la luminescence

pyroélectrique de type 2 n'est en effet qu'une superposition de deux phénomènes : les claquages de l'atmosphère et le début d'une émission médié par champ pyroélectrique soit par l'effet Poole-Frenkel soit par l'effet tunnel Fowler-Nordheim.

Pour ce qui concerne les différences qualitatives entre les matériaux il faut souligner que lors d'un échauffement, il y a toujours la coexistence de la luminescence thermiquement stimulée et de la luminescence pyroélectrique. C'est seulement lors des mesures de refroidissement que l'on observe un effet purement pyroélectrique. La question est donc : comment est-ce que la luminescence pyroélectrique peut ioniser des défauts que la luminescence thermiquement stimulée n'a pas encore pu ioniser à haute température? La réponse couvre une partie de l'objectif 2 : pour qu'on puisse ioniser quelque chose qui n'est pas déjà thermiquement ionisé, il faut que la méthode donne accès à des défauts qui ont une énergie d'activation qui n'est pas thermiquement accessible dans la gamme de température sous investigation. Autrement dit : l'effet du champ pyroélectrique permet de baisser la barrière d'activation d'une manière importante comparé à l'énergie thermique. Et effectivement, le changement de la hauteur de barrière selon l'effet Poole-Frenkel peut atteindre des centaines de meV et se trouve donc dans le même ordre de grandeur que les énergies thermiques observées.

Ceci est une observation importante : la luminescence pyroélectrique permet alors d'obtenir une signature optique de défauts qui n'est pas accessible autrement. Les défauts profonds pourraient devenir accessibles à la spectroscopie optique mais la question se pose dans quel mesure le modèle permet d'extraire des valeurs d'une manière reproductible.

Pour répondre à cette question, rappelons-nous du nombre d'approximations que nous avons dû mettre en place : les paramètres de matériau doivent être indépendants de la température pour obtenir une équation relativement simple de l'évolution du champ pyroélectrique en fonction du temps. Le taux de changement de température doit être constant. On doit connaître la forme du potentiel du défaut pour bien modéliser l'effet du champ pyroélectrique sur la forme du potentiel. Et principalement, il faudrait connaître le champ local à l'emplacement du défaut dans le cristal qui nécessite typiquement une analyse approfondie des effets d'écrantage locale par des méthodes numériques telles

que la théorie de fonctionnels de densité (DFT). Ceci dépasse amplement les objectifs de cette thèse.

Concernant les observations qualitatives par rapport aux échantillons spécifiques, on peut constater que 1) le baryum de titanate a effectivement une signature d'émission qui reflète la présence des transitions de phase bien que ceci n'est pas une corrélation évidente et qui doit probablement prendre en considération l'orientation entre la polarisation et les électrodes. Il est impossible de supprimer la luminescence pyroélectrique de type 1 totalement, ceci est probablement une indication de contaminations de surface qui permettent un claquage le long de la surface. Cette observation est appuyée par des expériences très récentes avec des nanopoudres du titanate de baryum qui ne donnent aucune signature de la luminescence pyroélectrique, ce qui est fort probablement associé à leur nature hygroscopique.

2) dans le niobate de lithium, il n'y a aucune anomalie de la luminescence pyroélectrique mais il y a des signatures dont l'origine reste à établir. Comme les résultats de cette nouvelle technique de spectroscopie ne se comparent pas à ceux obtenus par d'autres techniques comme la luminescence thermiquement stimulée, nous nous trouvons tout au début d'une investigation qui permet la spectroscopie de défauts avec une grande énergie d'activation. Dans le cas du niobate de lithium, à cause de l'absence de transitions de phases induites par l'échantillon, il est possible d'observer un effet autour de 100 degrés Celsius et qui est probablement associé à la désorption d'eau de la surface. Une augmentation de l'émission détectée pour des températures plus élevées est à la fois associé à l'ionisation de défauts et à la détection de la signature infrarouge que chaque échantillon et même le porte-échantillon émet à titre de radiateur noir. 3) Concernant le beta-baryum borate, nous constatons que l'échantillon émet de la luminescence pyroélectrique même si la photoexcitation avec les sources de lumière disponibles dans le cadre de cette thèse ne sont pas d'une énergie suffisante pour dépasser la bande interdite et pour remplir les pièges de capteurs de charges d'une manière efficace. Nous constatons pourtant au même moment que les échantillons sont transparents sans coloration perceptible de sorte qu'il est peu probable qu'il y a eu une photoexcitation efficace qui transfert les électrons directement dans les défauts. Ceci ne laisse que l'option que le beta-baryum borate, au moins les cristaux synthétisés de la

manière par laquelle les nôtres étaient fabriqués i.e. la croissance de Chrochalski, contiennent des défauts qui sont à dates inconnus.

### 3.1 Conclusions

Dans le cadre de cette thèse, j'ai pu démontrer plusieurs éléments qui font avancer la compréhension de la luminescence pyroélectrique de type 2 et 3.

- en considérant que la luminescence pyroélectrique de type 2 et 3 cède avec l'apparition d'une décharge, il est mis en évidence que le champ pyroélectrique est à l'origine des phénomènes de cette émission continue
- le comportement connu de cette émission en fonction de la pression atmosphérique ambiante est expliqué dans le contexte de la loi de Paschen qui décrit l'évolution du champ de claquage en fonction de la pression atmosphérique. En particulier, il est conclu que la luminescence pyroélectrique de type 3 ne se produit qu'uniquement dans des conditions avec un champ de claquage exceptionnellement élevé qui n'est donc pas atteint.
- en présence des ces forts champ pyroélectrique, une contribution additionnelle à l'ionisation de porteurs de charges doit être prise en considération : soit la réduction de la barrière en fonction d'un champ électrique tel que décrit par l'effet Poole-Frenkel, soit le contournement de la barrière par effet tunnel dépendant du champ connu comme effet tunnel Fowler-Nordheim. Ce dernier sera dominant pour des champs les plus élevés.

- Le champ électrique est expérimentalement accessible et permet d'extraire les énergies d'activation numériquement. Cette modélisation numérique est pourtant basée sur des valeurs des paramètres des matériaux obtenues par la littérature et a) peuvent considérablement varier d'un échantillon à l'autre et b) pour que le modèle puisse être approximé, il faut actuellement encore considérer que ces paramètres soient indépendants de la température, une approximation qui n'est certainement pas globalement valide. Les valeurs obtenues par nos analyses indiquent pourtant qu'il s'agit effectivement de défauts avec une énergie d'activation tellement élevée qu'elle n'est pas accessible par e.g. la luminescence thermiquement stimulée.
- La présence de transitions de phase avec une divergence du coefficient pyroélectrique amplifie l'intensité de la luminescence pyroélectrique mais il paraît qu'il faut prendre en considération l'anisotropie entre la polarisation permanente du matériau et les électrodes ou bien l'orientation du champ pyroélectrique en fonction de la forme exacte du potentiel des défauts.
- La luminescence pyroélectrique de type 3 peut être superposée à la luminescence pyroélectrique de type 1 ce qui était malheureusement appelé pyroélectricité de type 2 dans la référence la plus citée à ce sujet. Il ne s'agit pas d'un phénomène indépendant.
- La luminescence pyroélectrique permet principalement de déterminer les énergies d'activation des défauts autrement non-accessibles par e.g. la luminescence thermiquement stimulée mais la modélisation est considérablement plus complexe de sorte qu'une analyse fiable nécessite également la connaissance de tous les paramètres pertinents pour ce phénomène en fonction de la température dans la gamme de température pertinente.
- Il s'agit d'un nouvel outil spectroscopique qui fonctionne avec de l'équipement disponible dans la plupart de départements de physique ou des sciences de matériaux. La pertinence de cette méthode sera initialement la possibilité d'établir une nouvelle signature pour des défauts qui ont à date probablement échappés aux autres techniques spectroscopiques. Dans un deuxième temps, cette technique permettra

à établir les chemins de transfert de charges après photoexcitation, un défi connu également dans la luminescence thermiquement stimulée.

## 3.2 Perspectives

À la fin de cette thèse, nous avons pu confirmer que l'hypothèse qu'il s'agit effectivement de la signature de défauts cristallins. Idéalement, l'extraction des valeurs de l'énergie d'activation pour le ou les défauts permettra de caractériser la nature des défauts dans un cristal.

Ce qui reste à faire est d'analyser la reproductibilité de la méthode et d'optimiser la photoexcitation en fonction de la bande interdite. Comme nous avons uniquement eu un cryostat d'azote à notre disposition, tous les défauts avec une émission entre 1.6 K (température de transition de phase de l'hélium sous vide) et 77 K n'étaient pas accessible. Nous sommes en train d'établir une collaboration avec l'équipe de Denis Morris de l'université de Sherbrooke à ces fins.

La modélisation dans le cadre de cette thèse était limitée à deux cas : un potentiel Coulombique et un potentiel rectangulaire. Celles-ci sont deux approximations communes mais la vraie forme des potentiels dans la direction du champ pyroélectrique reste à établir par des techniques numériques.

Pour identifier la provenance spatiale de l'émission, nous avons programmé des expositions de longue durée avec des appareils numériques pendant toute la durée du changement de la température. Ceci permettra à vérifier s'il y a effectivement un effet de claquages résiduelles qui proviennent de la surface ou s'il y a des décharges à l'intérieur de l'échantillon qui pourraient indiquer le début des effets d'avalanche.